POLITECNICO DI MILANO

Dipartimento di Meccanica

DESIGN AND EXPERIMENTAL TESTS OF A CM-SCALE WIND TURBINE FOR ENERGY HARVESTING APPICATIONS

Relatrice: Gisella Marita Tomasini

Correlatore: Luca Bernini

Tesi di Laurea Magistrale in Mechanical Engineering

Davide Gasparini – Matr. 837836

Anno accademico 2016/2017

Davide Gasparini

DESIGN AND EXPERIMENTAL TESTS OF A CM-SCALE TURBINE FOR ENERGY HARVESTING APPLICATIONS

Tesi di Laurea Magistrale in Mechanical Engineering

Davide.Gasparini@mail.polimi.it

Data di esposizione

28-04-2017

Il lavoro svolto voglio dedicarlo agli amici di sempre che hanno sopportato le continue lamentele durante gli anni di studio, ma che mi hanno aiuto ad affrontare con il sorriso anche quelle difficoltà che sembravano insormontabili. Voglio fare una dedica a tutti gli amici che ho conosciuto durante gli anni passati al Politecnico di Milano, con cui ho condiviso gioie e dolori della carriera universitaria e che porterò sempre nel mio cuore. In particolare, una dedica speciale va alla mia famiglia che mi è sempre stata vicina in ogni momento, dalle stressanti sessioni d'esame alle gioie per gli esami superati, stimolandomi a dare il meglio di me in ogni situazione e che mi ha insegnato a non arrendermi mai qualsiasi cosa accada.

Davide

CONTENTS

LIST OF FIGURES

LIST OF TABLES

ABSTRACT

The purpose of the present research is the realization of a working prototype to be installed on freight train to power a wireless sensor node for structural diagnosis. The work deals with the modelling, designing and comparison of a centimeter wind turbine energy harvester. This cm-scale turbine is able to generate mechanical energy from the relative wind flow seen by the train while it is moving in still air.

In the first part of the analysis the simple BEM model predicts the best airfoil shape numerically designed and its performance in terms of power and power coefficient.

After, considerations on the imposed constraints are validated based by the final application. Furthermore, numerical performances are provided for the airfoil designed cm-scale turbine together with results regarding corrections applied on the numerical code to obtained convergence. Based on the conclusions of the analysis three prototypes are derived.

Then, experimental tests are performed in wind tunnel facility for the open field and confined flow operational configurations and performance results are presented, interpreted and compared between prototypes.

Keywords: energy harvesting, centimeter wind turbine, wind tunnel

Lo scopo del presente lavoro è realizzare un prototipo di recupero energetico da montare a bordo di treni merci per finalità diagnostiche. La trattazione documenta il processo realizzativo a partire dallo sviluppo del modello analitico, la sua analisi e validazione. Tramite la struttura delle pale, la turbina centimetrica è in grado di recuperare energia dal vento incidente che provoca un movimento rotatorio del rotore la cui energia meccanica viene convertita nel generatore in energia elettrica usufruibile.

Soggetto della prima parte della ricerca è lo sviluppo del modello BEM in grado di generare profili alari ottimizzati, basati su input dati in ingresso al codice numerico, e prevederne le performance in termini di potenza ed efficienza.

In seguito sono esaminati gli obbiettivi e soprattutto i vincoli dovuti all'applicazione finale del sistema di recupero energetico. Inoltre sono esaminate le modifiche apportare al codice numerico affinché arrivi convergenza. Da conclusioni basate sulle analisi ne sono derivati tre prototipi.

Infine vengono esaminati test sperimentali in galleria del vento in condizioni di campo aperto e turbina intubata, destinata all'applicazione finale; i cui risultati sono discussi e comparati.

***Parole chiave**: recupero energetico, turbine eolica, galleria del vento*

INTRODUCTION

The energy harvesting, or energy scavenging, is the research field that investigates the various possibilities to convert into usable power different form of energies available in the environment. In a world of technological advances, power demands are becoming more significantly a task to be achieved in many applications in order to guarantee sustainability and longevity. Batteries, despite some improvements, are remaining far beyond the requisites of long-term and low-maintenance use and therefore many research topics are currently under investigations, that promote different ways to provide power to small and smart electronics. At the same time, thanks to the progress in miniaturized sensors and processors, many researchers are studying wireless sensor nodes. These low-power demand devices are able to wirelessly communicate, exchanging information over a wide area for diagnostic purposes in a variety of fields. This scenario has gathered the raise of a new generation of power devices, capable of self-powering and of an autonomous and intelligent data management.

A wide number of researches have explored the fields of solar, thermal and body-derived energy harvesting. This effort provides the possibility to deploy large autonomous sensor networks, that are powered using the most suitable ambient resources in each context. For the latter reason, the fluid-flow energy harvesting is currently representing a promising source of energy for those environments in which sufficient flow velocities are present.

There are two main research fields that explore energy conversion method from wind or water flows. The first one is represented by centimeter-scale turbines, which show high efficiency and power density mostly for a relatively large range of flow speeds. The core of these devices is located on the structure and shape of the blades that are designed to generate as much mechanical energy as possible from the incoming wind flow. The second research field, which grants acceptable power levels starting from a lower set of wind speeds, harvests the mechanical energy induced by various aerodynamic instabilities.

The present investigation is intended to describe the design, the realization and the tests of a centimeter-scale wind turbine energy harvester, with the purpose to provide sufficient power for an autonomous wireless whose finale application is the structural analysis of freight train axles. Under an experimental and analytical procedure, the study is aimed at the performance examination and comparison of the designed airfoil cm-scale turbines and at the investigation of the energy provided by a confined flow symmetric centimeter turbine.

The centimeter-scale wind turbines are recently studied for their capacity of harvesting more energy than others energy harvesters. More researches focus their attention only on the construction and performance analysis of off-the-shelf cm-scale turbines [1], [2], using commercially available components to power small device like pressure sensors, temperature sensors, structure stress monitoring systems, smoke sensors or light emitting diodes. A recent study bases its analysis on the aerodynamics of the blades [3], using the BEM code to design and built a customized cm-scale turbine to optimize its efficiency for a low wind speed air-ventilation application. Others studies do not regard directly the turbine aerodynamics, but are focused on the optimization of the electro-mechanical conversion [4], [5].

With respect to the cited works, in this research not only the aerodynamic design of a centimeter scale blade using BEM code is developed, but also a deep investigation on a symmetric blade ducted turbine is performed. The latter turbine performance, design-based on the airfoil shape chord distribution, is investigated to develop a compact device able to provide sufficient electrical power working in a wide range of wind velocity.

IN the first part of the work a simple analytical model, the BEM model, has been adopted to design two cm-scale turbines. It allows to calculate the steady loads and thus also the thrust and the power for different settings of the wind speed, rotational speed and pitch angle. Providing in input the blades number, the rotor diameter, the Tip Speed Ratio and the design wind velocity, the simulation produces as output an optimized airfoil blade structure, from which two prototype with different rotor diameter, 4 cm and 3 cm are fabricated. Afterwards, in order to design a turbine able to provide energy for both train running directions, that is a bi-directional, a symmetric turbine is design based on the optimized chord of the 4 cm airfoil turbine.

Then, open field experiments are performed in “Sergio De Ponte” wind tunnel facility, to compare the airfoil performance results with the symmetric turbine, and in particular, those of the airfoil centimeter scale wind turbines are related to the numerical simulation in order to understand if the BEM code can provide a reliable numerical prototype. Finally, experimental tests are accomplished on a duct using the symmetric turbine, in prevision of the final application, in which the tube is composed by different modules that can be rearranged in order to find the best layout in term of power.

In detail, the present work is divided in four sections. It shows the development and the analysis of a numerical model and the experimental comparison through a series of tests.

In chapter 1, the basic theory of a turbine is reported showing the fundamental parameters and limitation for designing a wind turbine and the performance related to the modern large wind turbine for energy production. Then, an excursus on cm-scale wind turbines provided in literature is faced. Most of the authors consider the cm-scale turbine a suitable tool to harvest a sufficient amount of energy to power a small sensor for a wide range of wind velocity, because the turbines are characterized by high efficiency and power density.

The BEM model used to design the turbine's blade is pdescribed in chapter2. The 1-D momentum theory and the blade theory are explained and integrated with Glauert's correction, Prandtl's correction and the optimization model in order to provide the necessary steps for the blade design and analysis.

The design is carried out in chapter 3 where objectives and constraints are defined in order to design the 4 cm, 3 cm airfoil and 4 cm symmetric turbines. Furthermore, considerations and modeling of the duct are accomplished, in particular on a simple frustum divergent.

Chapter 4 regards the experimental tests that are divided in open field and confined flow tests. In the open field tests, active control experimental tests are performed for a direct comparison with the numerical simulation. Then passive tests are carried out for each turbine to evaluate the final performances for all the design prototypes. Confined flow tests are investigated, using the symmetric turbine, considering different configurations. In addition, a comparison is performed betweenr all the operational conditions in open field and, in particular, in the confined flow in order to determine the best layout in terms of power production for the final application.

1 State of the art

1.1 Basic theory of wind turbines

Wind turbines are systems designed to transform the wind kinetic energy into mechanical energy and finally into electrical energy. The maximum amount of power, P_{max}, that can be extracted is the total kinetic energy of the incoming wind flow:

$$P_{max} = \frac{1}{2}\dot{m}V_0^2 = \frac{1}{2}\rho A V_0^3 \qquad (1.1)$$

where $\dot{m}$ is the wind mass flow rate, V_0 is the wind speed, ρ is the density of the air and A is the wind turbine rotor area . Looking at the above equation the maximum power increases with the cube of the wind speed and linearly with density and area. In practice one cannot reduce the wind speed to zero obtaining the maximum energy conversion, so a power coefficient is defined [6] as the ratio between the actual power obtained and the maximum available power as given by the equation (1.2):

$$C_P = \frac{P_{actual}}{\frac{1}{2}\rho A V_0^3} \qquad (1.2)$$

Theoretically [6] there is a maximum C_P, denoted by the Betz limit, $C_{Pmax} = 16/27 = 0.593$. Modern wind turbines operate close to this limit with C_P up to 0.5.

When the wind impact the turbine's blade creates two force, Lift and Drag, perpendicular and parallel to the direction of relative wind respectively. All modern turbines consist of a number of rotating blades able to use lift force to extract energy from the wind, see figure (1.2) .

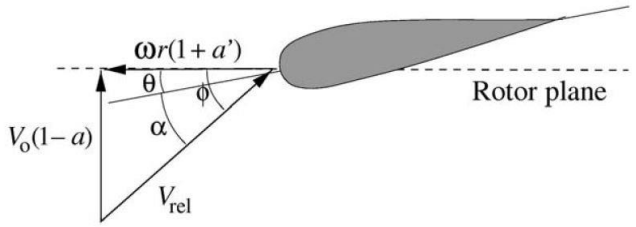

Figure 1.1 *Representation of the velocities and angle for a blade section*

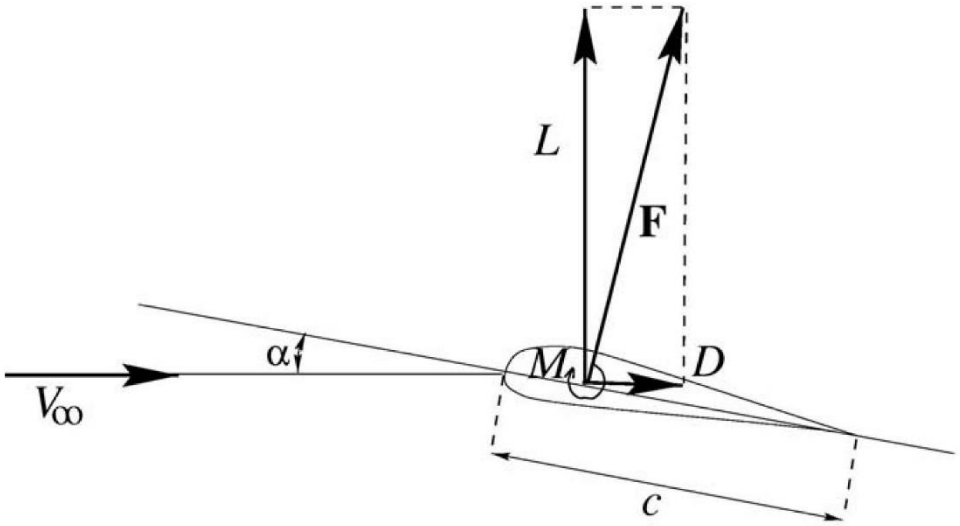

Figure 1.2 *Definition of Lift and Drag [6]*

If the blades are connected to a vertical shaft, the machine is called Vertical Axis Wind Turbine (VAWT), while if the shaft is horizontal the machine in called Horizontal Axis Wind Turbine (HAWT). A HAWT, as sketched in figure 1.3, is described in terms of rotor diameter, the number of blades, the tower height, the rated power and the control strategy.

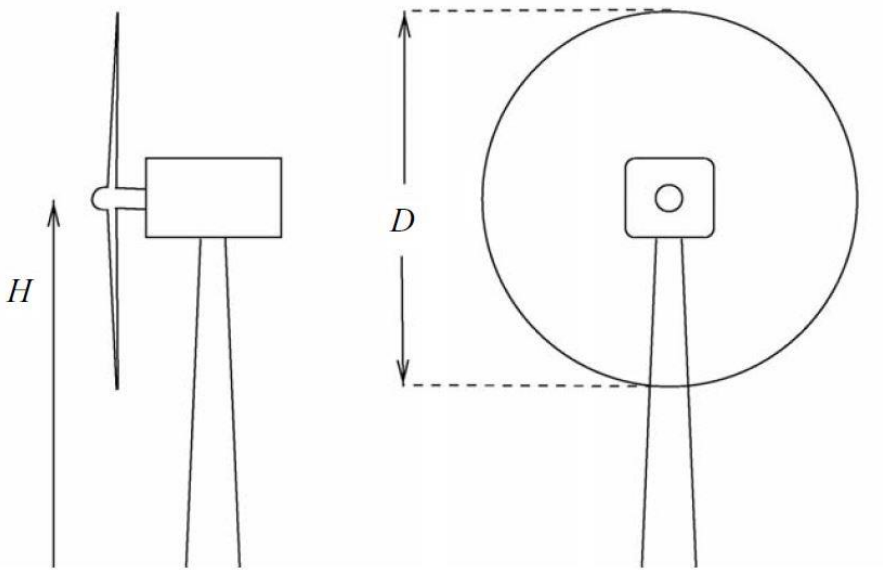

Figure 1.3 *Horizontal axis wind turbine (HAWT) [6]*

The tower height is important because the wind speed increases with height therefore increasing the power output of the turbine. The most common diameter size for modern wind turbine application are shown in figure 1.4.

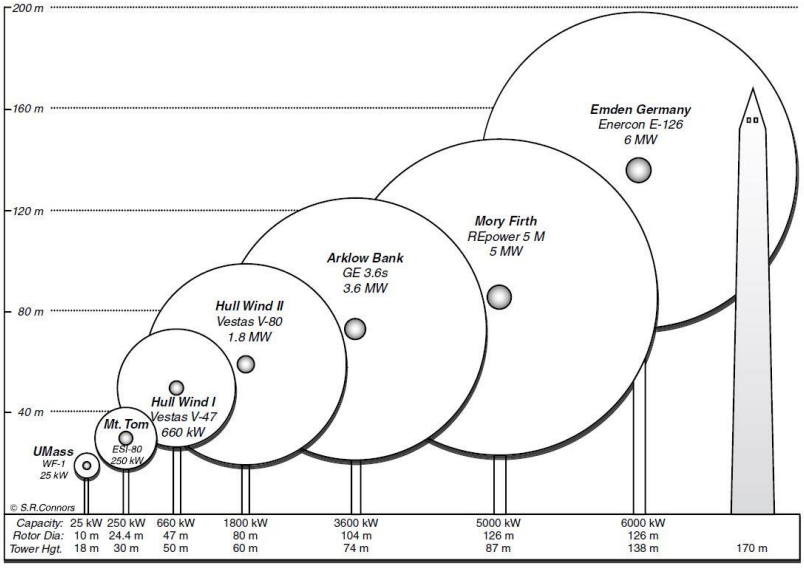

Figure 1.4 *Representative size, height, and diameter of wind turbines [7]*

The number of blades is usually two or three, in the late years however the three blade configuration has become the market reference configuration. The main motivation is due to the invariance of the rotor polar moment of inertia in respect to the rotor azimuthal position this guarantees mechanical stability of the system and allows for smoother yawing movement of the rotor [7]. In some extent three blade turbines have also a higher aerodynamic efficiency for being closer to the ideal optimum condition of infinite blade number [6]. The turbine could be a downwind machine, means that the rotor is downwind the tower, or vice versa, in upwind configuration. Downwind turbines are noisier, since the once-per-revolution tower passage of each blade is heard as a low frequency noise. The rotational speed of a wind turbine rotor is approximately 20 to 50 rpm and the rotational speed of most generator shaft is approximately 1000 to 3000 rpm. Therefore a gearbox must be placed between the low-speed rotor shaft and high-speed rotor generator shaft. As said, a HAWT consist of a series of blade with airfoil shape. The starting point for turbine blade design as describe in [7] assumes uniform axial flow upstream of the wind turbine, two-dimensional flow over the blades and steady-state operating condition, all under specific design aerodynamic conditions defined by the relationship between the rotor rotational speed and the incoming wind speed called Tip Speed Ratio (TSR):

$$TSR = \frac{\omega R}{V} \qquad (1.3)$$

where V is the wind speed, R is the rotor radius while ω the rotor rotational speed. As underline in [1] C_P is function of TSR, higher it is higher will be the turbine efficiency up to the Betz limit as shown in figure 1.5. By increasing TSR, angular speed is higher for the same air speed and less energy is lost as downstream swirl. More power can therefore be extracted with higher TSR.

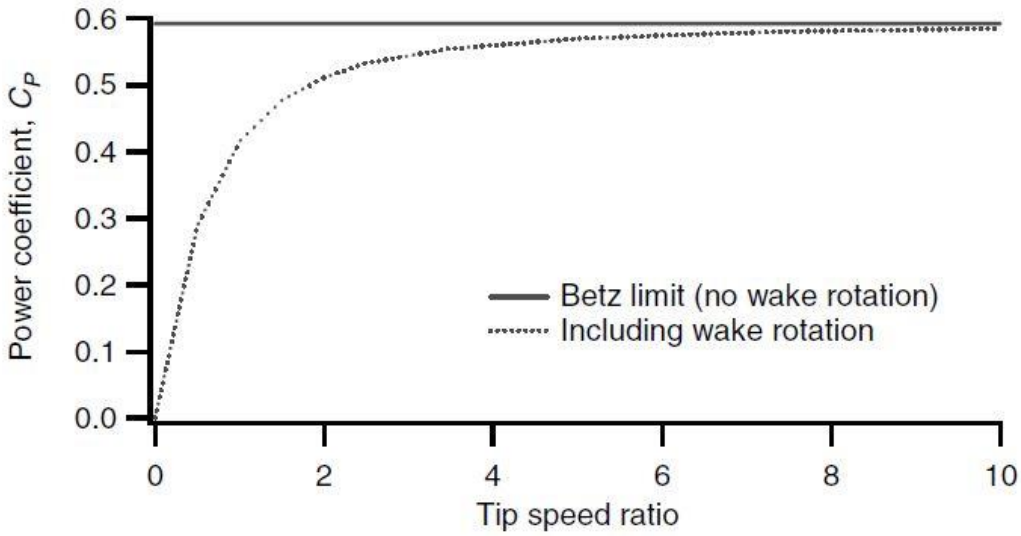

Figure 1.5 *Theoretical maximum power coefficient as a function of tip speed ratio for an ideal horizontal axis wind turbine, with and without wake rotation [7]*

1.2 State of the art of cm-scale wind turbines

1.2.1 Introduction

In recent years studies were carried out on cm-scale wind turbines for energy harvesting on small scale systems, typical application are duct ventilation system of buildings [1] and [3], the airflow under a bridge [8]. They differ from "micro turbines" and "wind turbines" because of their dimensions, applications and power production. Wind turbines, as introduced in the previous paragraph, are large commercial machine for electrical power generation with rotor diameter higher than 10 m and power production about MW. on the other hand, micro-turbines are used in power generation for domestic applications (micro turbines can be installed in gardens or on top of a house) in which the diameter range from 1 m to 3 m and the power produced is around 1 kW. Instead, the cm-scale wind turbines are small machines (order of centimeter) designed to power small electrical device with rated power in the order of mW. Another important difference is the presence of gearbox. Large turbines have a gearbox in order to increase the velocity of the generator shaft to reach 1000 to 3000 rpm and they have a very high mechanical-electrical efficiency, as explained in

[1], [6] and [7]. While in centimeter turbines the presence of the gearbox can reduce the efficiency by 50% [1]. The problem is studied also by [2] that make a deep investigation of the advantage and disadvantage of the gearbox use in cm-scale machines concluding that a gear transmission could be useful al very low wind speed, 3.5 m/s; while at 8m/s the gearbox is not useful because it reduces the efficiency of the system. Therefore it seems preferable to match the turbine rotation speed to that of the generator using a direct drive configuration [1]. Other studies were concentrated on mechanical-electrical conversion as in [9], where an electrostatic converter is tested as an alternative to classical electromagnetic converters. Another related work is [4] in which the study is concentrated on maximization of the wind generator performance in wide range of operating conditions using a buck-boots converter-based with the aim of low power losses. Another related study is [5] in which a combined axial-flow cm-turbine and an axial-flux electromagnetic generator is investigated.

Beside the miniaturization of the electro-mechanical conversion an important issue to be taken into consideration is the Low Reynolds number, defined in eq.(1.4), that characterize centimeter-scale wind turbines. Reynolds number below $5 \cdot 10^5$ could be expected which implies a reduction in the blade airfoil efficiency or Lift/Drag ratio [1]. The efficiency reduction is due to the Increase of viscous losses as a consequence of a low Reynolds number [3]. In fact as Reynolds decrease, viscous forces increase in magnitude compared to the inertial forces, this leads to higher drag in the attached flow condition and in a stall angle reduction due to higher possibility of low Reynolds boundary layer of separation in adverse pressure gradient conditions at the blade trailing edge area [7], [2] and [9].

$$Re = UD/\nu \qquad (1.4)$$

Others important losses are related to the bearings [9], [3] that significantly reduce the low-speed operation opportunity. One solution could be the use of low friction bearings as done in [3] to provide low friction and start up speed. All this factor affects the performance of the centimeter-scale turbine that will be very low compared with larger scale one as sketched in figure 1.6.

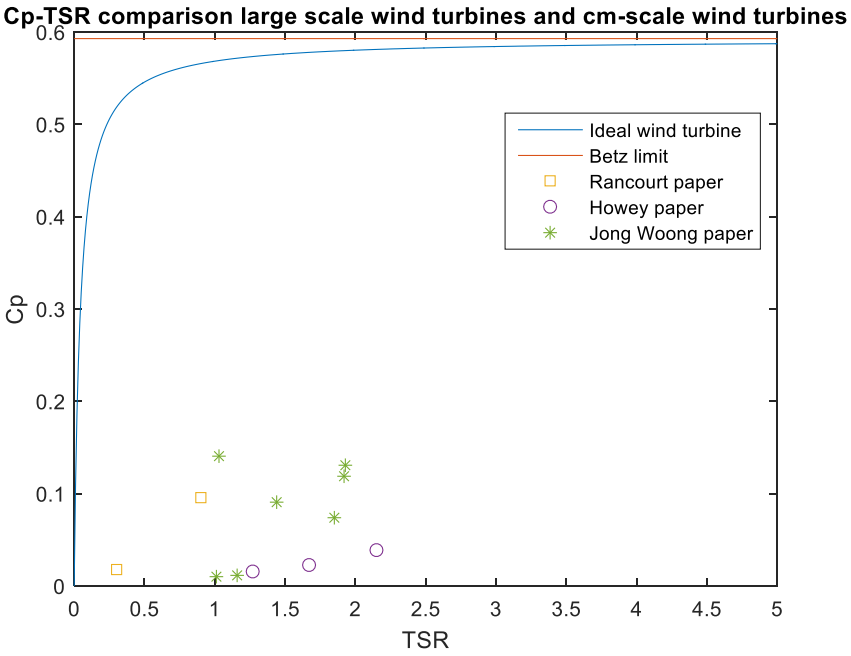

Figure 1.6 *Difference power coefficient of cm-scale wind turbine and large scale ideal wind turbine with infinite blade*

Therefore it is possible to have an indication that strong dimension reduction of the turbine rotor highly decrease the overall system performance [3], [1] and [8] with respect the large ideal scale turbine. However the cm-scale turbine analyzed in literature are built to power small device like pressure sensor, temperature sensor, structure stress monitoring system, smoke sensor or light emitting diode. Similar devices required only a small amount of power [mW] therefore even low efficiency system could be interesting.

1.2.2 Classification of the cm-scale turbines presented in literature

A classification of the studies found in literature can be made and regards:

- airfoil aerodynamics optimization;
- electro-mechanical conversion optimization;
- performance analysis off-the-shelf prototypes.

The table 1.1 shows variation in prototypes' diameter summarizes all the best performers cm-scale turbines found in literature review. Some authors focus their attention on off-the-shelf turbines using only commercial available components as in [1], [2], [10] and [8]. The aim in these papers was not the optimization of the turbine but the analysis performance as in [1] in comparison with the large-scale turbines, or in case of [2] the effect of the gearbox on the overall performance. While in some cases the aim

was only a sufficient amount of energy production to feed a wireless sensor as in [10] or in [8], in which the author wants to maximize the performance of the centimeter wind turbines.

Looking to work specifically focused on the aerodynamic optimization [3], there is an explanation of the numerical procedure and the experimental results; the aim of the study was the achievement of the maximum possible power coefficient for a 2 cm wind turbine.

Others authors concentrate their attention on the optimization of the electro-mechanical conversion [4], [9] and [5]. In those papers different methods are applied in order to optimize the turbine electro-mechanical efficiency. The purpose of the optimization in [4] regards the fulfilment of the performance maximization in wide wind speed range using a buck-boots converter-based maximum power point circuit using commercially available turbine. While in [9] the study is focused on an electrostatic converter in order to have an alternative generator with respect the common one.

Another important factor, is the final application of the turbine and in particular the environment in which the system is going to be placed. Given the specific application the external dimension could be fixed a priori due to the maximum available space such as in [3] in which the turbine has to be positioned in an air-duct and thus it was designed to occupy a small area as possible. So, the optimization design regards the aerodynamics of a fix dimension turbine (2 cm rotor diameter).

Reference	Rotor Diameter D [cm]	Number of blades	Air speed [m/s]	Average output power [µW]	Power density [µW/cm^2]	Efficiency Cp [%]
[5]	0.75	24	40	1.10E+03	2490	0.07
[1]	4.2	4	5.5	2.40E+03	173	1.8
			11.8	1.30E+05	9383	9.6
[2]	7.6	4	4	1.00E+04	220	5.6
			8	1.00E+05	2204	7.0
[4]	6.3	4	2.4	2.00E+03	64	7.9
			4.2	8.00E+03	257	5.9
			4.7	1.00E+04	321	5.2
[3]	2	4	3	8.00E+01	25	1.6
			7	2.50E+03	796	3.9
			10	4.30E+03	1369	2.3
[9]	4.0	4	4	3.00E+01	2	0.06
				2.00E+02	16	0.03
[8]	13.8	6	3.5	2.89E+04	193	7.4
			4	5.33E+04	356	9.1

			5	1.36E+05	912	11.9
			6	2.59E+05	1734	13.1
			7	4.39E+05	2390	14.1
		2	7	1.75E+05	1170	5.6
		3	7	2.53E+05	1690	8.0
[10]	10.2	4	2.5	8.00E+02	10	1.1
			4	1.50E+03	19	0.5
			6	2.70E+03	34	0.5

Table 1.1 *Representation of best performance of cm-scale turbines in literature*

In the table the average output power is calculated as:

$$P_{out} = \frac{1}{2}\rho A C_p V^3 \qquad (1.5)$$

The data in table 1.1 comes experiment results. The cm-turbines are always horizontal axis ones because of the higher efficiency in respect of than vertical axis ones. It can be noted that no centimeter-scale windmills are compatible with wind velocity lower than $2\ m/s$ because of bearing's friction and the strong electro-mechanical efficiency reduction at low speed.

A comparison among the cited works is possible even if they are presented micro turbine design was an optimal one. Figure 1.7 shows a comparison of the different cm scale turbines found in literature. Performance depends on the velocity of the wind flow. [8] is an example, by increasing the velocity of the wind flow, increase the power coefficient. High performance can be reached by lower diameter turbines when the optimization is computed at a specific wind velocity.

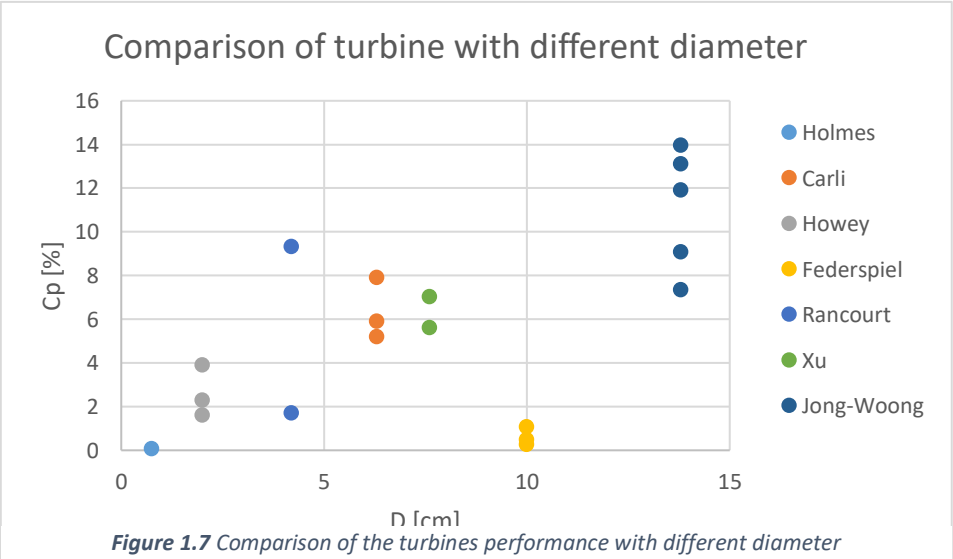

Figure 1.7 *Comparison of the turbines performance with different diameter*

1 State of the art

The purpose of the present study is the design and fabrication of a cm-scale turbine able to feed a monitoring sensor in a wide range of wind velocity application. The sensor need to be placed on a freight train that is a different environment with respect a duct, therefore it need to be as small as possible and to be able of extrapolating sufficient energy from the wind even at low wind speed (the design wind speed is 10 m/s).
These are the main reasons that brought us to numerical design optimization with the BEM model, as done in [3]. The differences with previous studies is that the desired turbine need to work at wind speed up to 30 m/s, resulting in wind speed working range wider than any other find in literature.
The optimization is done considering only the airfoil aerodynamics, without considering the generator.

2 The Classical Blade Element Momentum Method

The blade element momentum method allows to calculate the steady loads and, thus, also the thrust and the power for different settings of wind speed, rotational speed and pitch angle. The BEM numerical procedure is adopted to design the different turbines of this project. The most general numerical method is CFD but it involves too complex problems that are out of the scope of the present work whose first objective is not to maximize the extracted power but to design a turbine able to power the node considering the constraint of the application.

This theory derives from 1-D momentum theory for an ideal wind turbine in which the actual geometry of the rotor (the number of blades, the twist, the chord and the airfoils used) is not considered and in which the disc is supposed ideal so it is frictionless and there is no rotational velocity component in the wake. Therefore the Blade Element Momentum method couples the 1-D momentum theory with the actual blades one.

In the following paragraphs, 1-D momentum theory, blade theory and the subsequent BEM model are described focusing the attention, in particular, on the procedure used to design the blade of the turbine.

2.1 One-dimensional Momentum Theory for an ideal wind turbine

A wind turbine extracts mechanical power from the wind kinetic energy. The rotor is considered ideal so it is frictionless and there is no rotational component in the wake. The rotor acts as a drag device, as described in [6], slowing the wind speed V_0 far upstream of the rotor to u at the rotor plane and u_1 in the wake (figure 2.1). The drag is obtained by a pressure drops over the rotor: in upstream section, close to the rotor, there is a small rise of the pressure from the atmospheric level p_0 to p, before a discontinuous pressure drops Δp over the rotor (figure 2.2); downstream the rotor, the pressure recovers the atmospheric level. Due to the pressure drops there is also a wind speed variation; the axial velocity continuously decreases from V_0 to u_1 (velocity of undisturbed wind and wind speed at the rotor plane, respectively). Furthermore, the wake increases its area from the upstream zone to the downstream (see figure 2.1). The behavior of the pressure and the axial velocity is shown in figure 2.2.

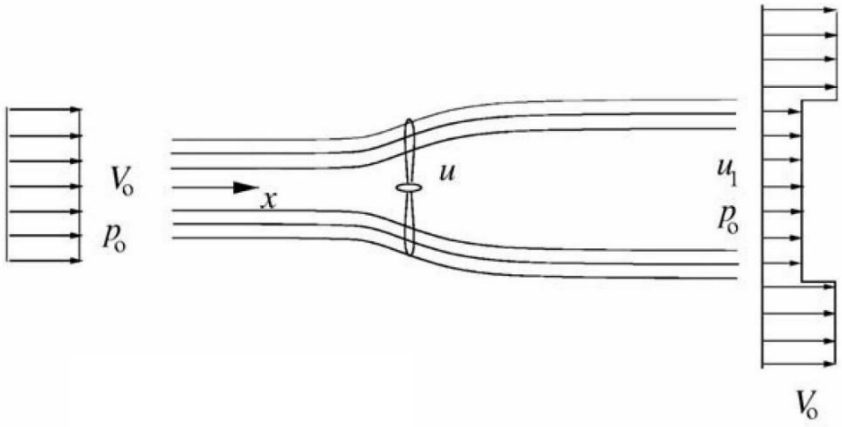

Figure 2.1 *Behavior of pressure and area and velocity streamline [6]*

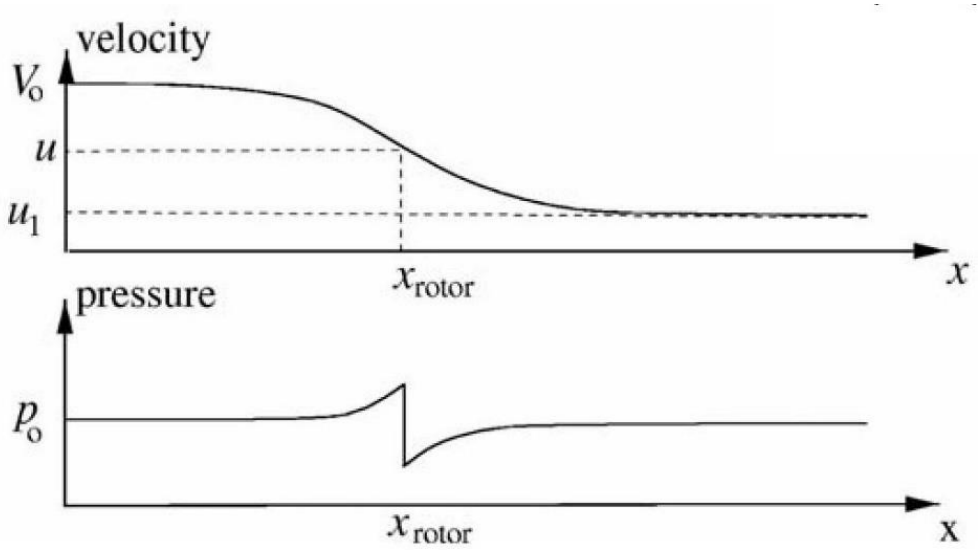

Figure 2.2 *Illustration of pressure and velocity variation across the turbine [6]*

Using the assumption of an ideal rotor, it is possible to derive relationships between velocities V_0, u_1 and u, the thrust T and the absorbed shaft power P. The analysis assumes a control volume, in which the control volume boundaries are the surface of the stream tube (see figure 2.3). The only flow is across the ends of the stream tube and the two cross-sections of the stream tube. In figure 2.3 section 1 corresponds to the inlet of the control volume; section 2 and 3 are, respectively, the up-stream area before the turbine, and the down-stream section. Section 4 coincides with the outlet of the control volume. The turbine is represented is represented by a uniform “actuator disc” which creates a discontinuity of the pressure in the stream tube of air flowing through it.

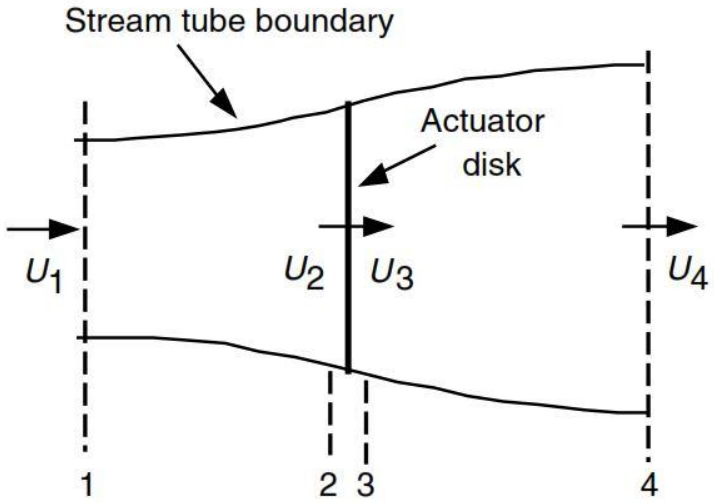

Figure 2.3 *Actuator disc model of a wind turbine: U indicates the mean velocity while 1,2,3 and 4 the location [7]*

The only flow is across the ends of the stream tube and the turbine is represented by a uniform "actuator disc" that creates the pressure discontinuity.

The assumptions of this analysis, as said in [7], are:

- homogenous, incompressible, steady state fluid flow;
- no frictional drag;
- infinite number of blades;
- uniform thrust over the disc or rotor area;
- non-rotating wake;
- static pressure far upstream and far downstream of the rotor are equal to the undistributed ambient static pressure.

Applying the conservation of linear momentum to the control volume enclosing the whole system, as explained in [7], it is possible to find the net force on the contents of the control volume. This force is equal and opposite to the thrust T which is the force of the wind on the wind turbine. From conservation of linear momentum for one-dimensional, incompressible, time-invariant flow, the thrust is equal and opposite to the rate of change of the momentum of the air stream:

$$T = U_1(\rho UA)_1 - U_4(\rho UA)_4 \qquad (2.1)$$

in which $A = \pi R^2$ describes the area of the rotor, ρ is the air density and U is the air velocity. For steady state flow $(\rho UA)_1 = (\rho UA)_4 = \dot{m}$ represents the mass flow rate. Substituting the mass flow rate in equation (2.1) yields:

$$T = \dot{m}(U_1 - U_4) \tag{2.2}$$

Because the thrust must be positive, the velocity behind the rotor is lower than the free stream velocity U_1. Since the flow is stationary, incompressible and frictionless and no force acts on the fluid up or downstream the rotor: the Bernoulli equation can be applied far up-stream:

$$p_1 + \frac{1}{2}\rho U_1^2 = p_2 + \frac{1}{2}\rho U_2^2 \tag{2.3}$$

and far downstream in the wake:

$$p_3 + \frac{1}{2}\rho U_3^2 = p_4 + \frac{1}{2}\rho U_4^2 \tag{2.4}$$

It is assumed that far upstream and downstream pressures are equals ($p_1 = p_4$) and the velocity across the disc remains the same ($U_2 = U_3$). So, the thrust can be expressed as:

$$T = A_2(p_2 - p_3) \tag{2.5}$$

In the equation (2.5) it is possible to see the creation of the thrust T thanks to the pressure drop on the rotor. Solving the equations (2.3) and (2.4) for $(p_2 - p_3)$ and substitute into equation (2.5) yields:

$$T = \frac{1}{2}A_2\rho(U_1^2 - U_4^2) \tag{2.6}$$

Where A_2 is the cross-area of section 2 (see figure 2.3). Equating the thrust from equations (2.2) and (2.6) it is possible to obtain a velocity expression:

$$U_2 = \frac{U_1 + U_4}{2} \tag{2.7}$$

Thus, the wind velocity at the rotor plane, using this simple model, is the average of the upstream and downstream wind speed.

If one defines the axial induction factor a as the fractional decrease in wind velocity between the free stream and the rotor plane, then:

$$a = \frac{U_1 - U_2}{U_1} \tag{2.8}$$

$$U_2 = U_1(1-a) \tag{2.9}$$

and:

$$U_4 = U_1(1-2a) \tag{2.10}$$

The quantity $U_1 a$ is often referred to as the induced velocity at the rotor, in which case the velocity of the wind at the rotor is a combination of the stream velocity and the induced wind velocity. The power output, P, is equal to the thrust times the velocity at the disc:

$$P = TU_2 = \frac{1}{2}A_2\rho(U_1^2 - U_4^2)U_2 \tag{2.11}$$

Substituting for U_2 and U_4 the expression of the equations (2.8) and (2.9) it is possible to find another expression of the power as function of the axial induction factor:

$$P = 2\rho A U^3 a(1-a)^2 \tag{2.12}$$

In the expression (2.12) the control volume area A_2 is substituted by the area A and the free stream velocity U_1 at section 1 is replaced by U.

The available power in a cross-section equal to the swept area A by the rotor, as described in [6], is:

$$P_{avail} = \frac{1}{2}\rho A U^3 \tag{2.13}$$

The power P is often non-dimensionalized with respect to P_{avail} as performance coefficient (or power coefficient):

$$C_P = \frac{P}{\frac{1}{2}\rho U^3 A} = \frac{Rotor\ power}{Power\ in\ the\ wind} \tag{2.14}$$

The non-dimensional power coefficient represents the fraction of power in the wind that is extracted by the rotor. Using the equation (2.12) the power coefficient for an idea wind turbine may be written as:

$$C_P = 4a(1-a)^2 \tag{2.15}$$

Differentiating C_p with respect to *a* yields:

$$\frac{dC_P}{da} = 4(1-a)(1-3a) \tag{2.16}$$

It is easily seen that $C_{P,max} = 16/27$ for $a = 1/3$.This theoretical maximum is called Betz limit, as explained in [6]. This level is achieved by large scale wind turbines, but for centimeter scale wind turbines there are problems regarding viscous losses at low Reynolds number and downscaling issue that cause other type of losses, as explained in paragraph 1.2.1, such that the C_P coefficient is very low with respect the Betz limit.
In similar way, the thrust coefficient can be expressed as function of the axial induction factor and in dimensionless term:

$$T = \frac{1}{2}\rho A U^2[4a(1-a)] \tag{2.17}$$

In non-dimensional form yields:

$$C_T = \frac{T}{\frac{1}{2}\rho U^3 A} = \frac{Thrust\ force}{Dynamic\ force} \tag{2.18}$$

$$C_T = 4a(1-a) \tag{2.19}$$

The thrust coefficient for an ideal wind turbine as a maximum of 1.0 when $a = 0.5$ and the downstream velocity is zero (see figure 2.4).

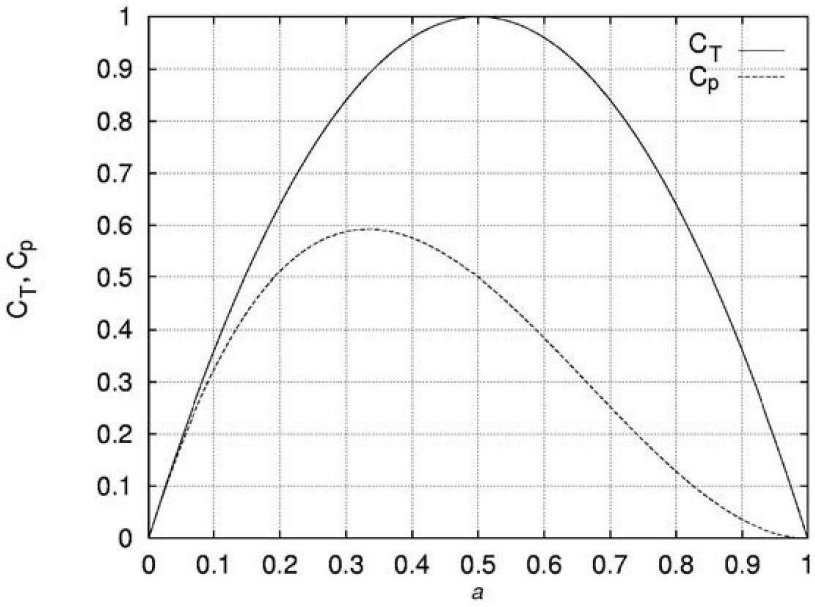

Figure 2.4 *The power and the thrust coefficients C_p and C_T as a function of the axial induction a for an ideal wind turbine*

The assumptions of ideal wind turbine are valid for an axial induction factor of approximately 0.4. If a overcome the limit value the, 1-D momentum theory is not able to describe correctly the behavior of C_T. High thrust and, thus, high axial induction factor are present at low wind speed; lower the wind speed downstream means higher flow due to the continuity. The reason of the incapacity to describe what happens at $a > 0.4$ is due to the free shear layer at the edge of the wake that becomes unstable when the velocity jump $U_1 - U_4$ becomes too high and eddies are formed which transport momentum from the outer flow into the wake. This situation is called turbulent-wake state.

2.1.1 Ideal horizontal axis wind turbine with wake rotation

In the previous section it was assumed that no rotation was imparted to the flow. But in wind turbine the wake behind the rotor rotates in opposite direction to the rotor itself, in reaction to the torque exerted by the flow on the rotor, as considered in [6].

The rotor of a horizontal-axis wind turbine consists of a number of blades and if a cut is made at the radial distance, r, from the rotational axis, see figure 2.5, a cascade of airfoils is observed as in figure 2.6.

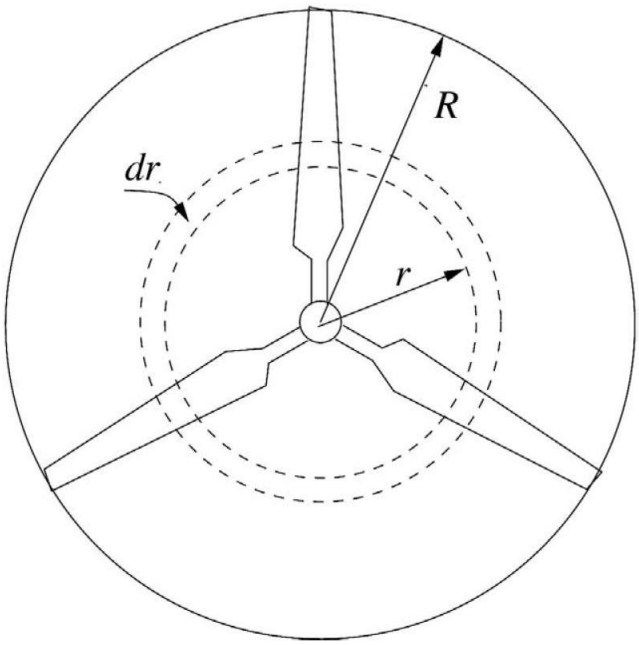

Figure 2.5 *Rotor of a three-blade turbine with rotor radius R [6]*

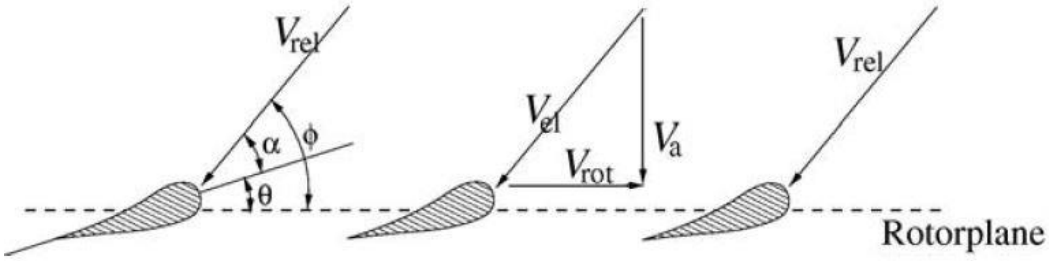

Figure 2.6 *Radial cut in a wind turbine rotor showing airfoils at r/R*

The local angle of attach is defined as:

$$\alpha = \phi - \theta \qquad (2.20)$$

where ϕ is the flow angle while θ is the blade pitch angle. The axial velocity and the rotational velocity are denoted respectively by V_a and V_{rot} (see figure 2.6).

Since a horizontal wind turbine consists of rotating blades, a vortex system must exist, the vortex is oriented in a helical path behind the rotor. The vortex system induces on a wind turbine an axial velocity component opposite to the direction of the wind and a tangential velocity component opposite to the rotation of the rotor blades. The induced velocity in the axial direction is specified by the axial induction factor a as aV_0, where V_0 is the undisturbed wind speed. The induced tangential velocity in the wake is specified through the

tangential induction factor a' as $2a'\omega r$. Since the flow does not rotate upstream of the rotor, the tangential induced velocity in the rotor plane can is thus approximately $a'\omega r$. ω denotes the angular while r is the radial distance from the rotational axis velocity of the rotor. The rotational kinetic energy in the wake results in less energy extracted by the rotor. Turbines with slow-running speed (low rotational speed and high torque) experience more wake rotation losses than high speed wind machines with low torque, as the case of cm-scale wind turbines. In figure 2.7 are illustrated the velocity triangle at the trailing edge and the leading edge.

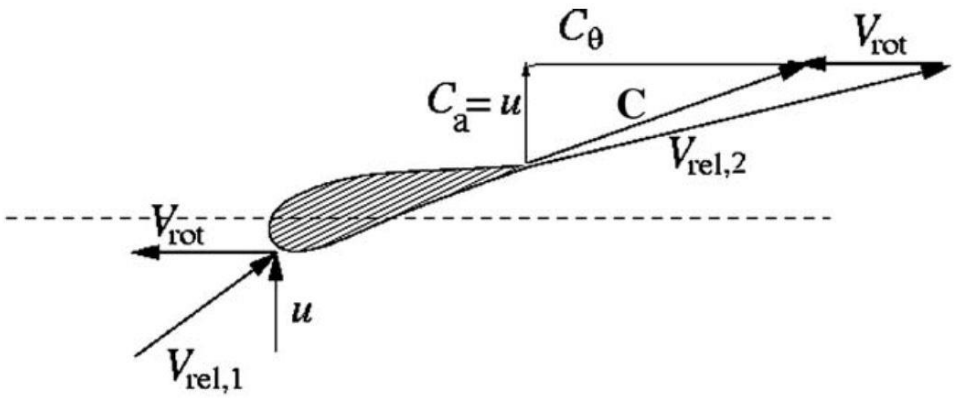

Figure 2.7 *Illustration of velocity triangles for a section of the rotor [6]*

The relative velocity upstream of the blade $V_{rel,1}$ is given by the axial velocity u and the rotational velocity V_{rot}. For moderate angle of attach (see figure 2.6), the relative velocity downstream $V_{rel,2}$ approximately follows the trailing edge. The axial component C_a equals u due to the conservation of the mass and the rotational speed V_{rot} is unaltered. The velocity triangle downstream of the blade is now fixed and the absolute velocity downstream, C, has a tangential component C_θ in the opposite direction of the blade, expressed as:

$$C_\theta = 2a'\omega r \qquad (2.20)$$

that is the one that causes the rotation into the wake and reduces the energy extracted by the rotor. Therefore, a reduction of the C_θ is desirable to enhance the efficiency of the turbine and it can be done increasing the rotational speed to minimize the loss of kinetic energy contained in the rotating wake.

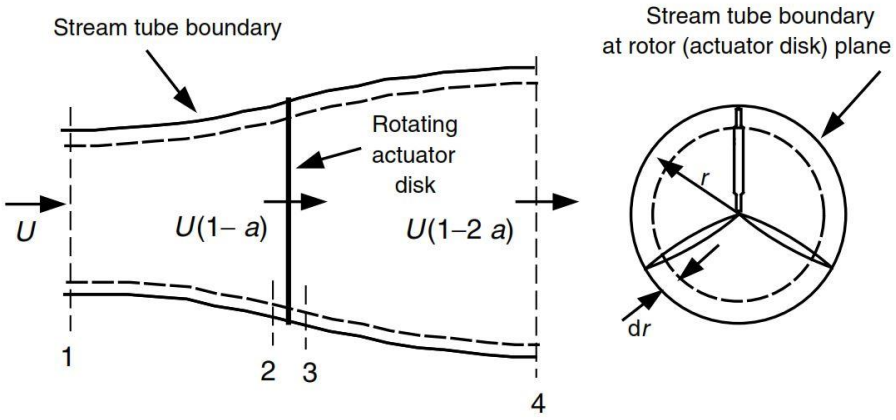

Figure 2.8 *Reference geometry for the rotor analysis [7]*

Figure 2.8 gives a schematic of the parameter involved in the analysis. If it is assumed that the angular velocity induced by the flow stream, ω, is small compared to the angular velocity, Ω, of the wind turbine rotor, then it can also be assumed that the pressure in the far wake is to the pressure in the far stream. The following analysis is based on the use of an annular stream tube with a radius r and a thickness dr, resulting in a cross sectional area equal to $2\pi r dr$ (see figure 2.8). If one uses a control volume that moves with the angular velocity of the blades, the energy equation can be applied in the section before and after the blades to derive for the pressure difference across the blades. Note that across the flow disc, the angular velocity of the air relative to the blade increases from Ω to $\Omega + \omega$, while the axial component remains constant. The resulting pressure difference across the blade yields:

$$p_2 - p_3 = \rho(\Omega + \tfrac{1}{2}\omega)\omega r^2 \qquad (2.21)$$

The resulting thrust in the annular element, dT:

$$dT = (p_2 - p_3)dA = [\rho(\Omega + \tfrac{1}{2}\omega)\omega r^2]\, 2\pi r dr \qquad (2.22)$$

Because the rotation of the wake is included in the analysis is necessary to consider the angular induction factor in the expression. Therefore, the equation of the thrust becomes:

$$dT = 4a'(1 + a')\tfrac{1}{2}\rho\Omega^2 r^2 2\pi r dr \qquad (2.23)$$

Using the axial induction factor, a, to determine the thrust at the annular cross-section:

$$dT = 4a(1-a)\frac{1}{2}\rho U^2 2\pi r dr \quad (2.24)$$

Equating the two expression of the thrust (2.23) and (2.24) yields:

$$\frac{a(1-a)}{a\prime(1+a')} = \frac{\Omega^2 r^2}{U^2} = \lambda_r^2 \quad (2.25)$$

where λ_r represents the local speed ratio for each annular section. The torque exerted on the rotor is defined as:

$$dM = 4a'(1-a)U\rho\Omega r^3\pi dr \quad (2.26)$$

The power is defined as the product between the angular velocity of the rotor and the torque:

$$dP = \Omega dM \quad (2.27)$$

Substituting the equation (2.26) into the equation (2.27) the expression of the power at each annular section becomes:

$$dP = \frac{1}{2}\rho A U^3[\frac{8}{\lambda^2}a'(1-a)\lambda_r^3 d\lambda_r] \quad (2.28)$$

The power depends directly on the axial and angular induction factors and the tip speed ratio. The axial and angular induction factors determine the magnitude and the direction of the airflow at the rotor plane. The local tip speed ratio, λ_r, is function of the tip speed ratio λ, which is basically defined as $\lambda = \Omega R/U$ where Ω is the rotational speed of the rotor, R is the radius and U is the wind speed. The relationship between λ_r and the tip speed ratio is:

$$\lambda_r = \frac{\Omega r}{U} = \frac{\lambda r}{R} \quad (2.29)$$

The performance coefficient takes into account the axial and angular induction coefficients and the tip speed ratio:

$$Cp = \frac{8}{\lambda^2}\int_0^{\lambda} a'(1-a)\lambda_r^3 d\lambda_r \qquad (2.30)$$

In order to integrate ones needs to relate a, a' and λ_r. Solving the equation (2.25) to express a' as function of a one gets:

$$a' = \frac{1}{2} + \frac{1}{2}\sqrt{[1 + \frac{4}{\lambda_r^2}a(1-a)]} \qquad (2.31)$$

The aerodynamic conditions for the maximum possible power production occur when the term $\mathrm{a}'(1-\mathrm{a})$ in equation (2.25). Substituting the value for a' from equation (2.26) into $\mathrm{a}'(1-\mathrm{a})$ and settings the derivative with respect to a equal to zero yields:

$$\lambda_r^2 = \frac{(1-a)(4a-1)^2}{1-3a} \qquad (2.32)$$

This equation defines the axial induction factor for maxium power as function of the local tip speed ratio in each annular ring. Substituting equation (2.32) in (2.25) for the maximum power in each annular section a' is:

$$a' = \frac{1-3a}{4a-1} \qquad (2.33)$$

Thanks to this equation we are able to find an optimum value of the angular induction factor a' for a given axial value.

In this section basic physics has been used to determine the nature of the air flow around a wind turbine and the theoretical limits on the maximum power can be extracted from the wind.

2.2 Blade element theory

As extensively describe in [7], this theory allows to evaluate the forces acting on the blade element as function of the lift and the drag coefficients, expressed in the following equations, and the angle of attack defined in figure 2.9.

$$C_D = \frac{D}{\frac{1}{2}\rho V_{rel}^2 c} \tag{2.34}$$

$$C_L = \frac{L}{\frac{1}{2}\rho V_{rel}^2 c} \tag{2.35}$$

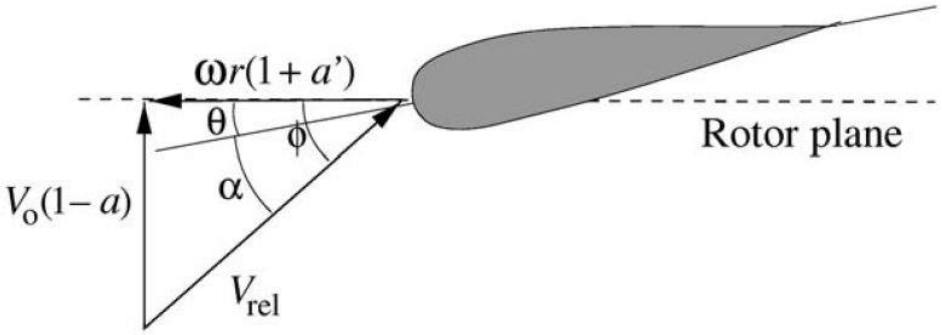

Figure 2.9 *Velocities at the rotor plane [6]*

in which θ is the pitch angle, α is the local angle of attach while ϕ is the flow angle. According to the theory the blade is divided into N sections (or elements) then the total force is calculated by integrating along the blade. The following assumptions are made:

- no aerodynamic interaction between the elements;
- the forces on the blades are determined only by the lift and drag characteristics of the airfoil shape of the blades.

In figure 2.10 there is the guideline geometry and nomenclature used to analyzed the blade element theory.

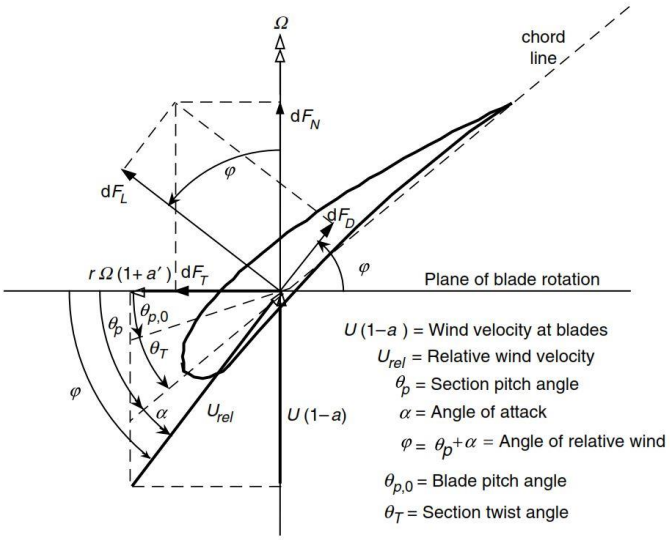

Figure 2.10 *Blade geometry for analysis of a horizontal axis wind turbine [7]*

The lift and drag forces are perpendicular and parallel, respectively, to the relative velocity between wind and blade. The relative velocity of the wind is the sum of the velocity of the blade rotation $\Omega r(1+a')$ and the wind velocity at the rotor $U(1-a)$. The first rotational component of the relative wind speed is composed by the blade section velocity Ωr, and the induced angular velocity $\Omega r a'$:

$$\Omega r + \frac{\omega r}{2} = \Omega r + \Omega r a' = \Omega r(1+a') \tag{2.36}$$

The overall flow situation is the combination of various forces, angles and velocities at the blade as shown in figure 2.10, where:

- dF_L is the incremental lift force;
- dF_D is the incremental drag force;
- dF_N is the incremental force normal to the rotor plane (contribute to the thrust);
- dF_T is the incremental force tangential to the circle swept by the rotor.

The angle of the relative wind speed depends on the section blade pitch angle and the angle of attack:

$$\varphi = \theta_p + \alpha \tag{2.37}$$

The section blade pitch angle θ_p, is the angle between the chord line and the plane of rotation. In order to define correctly a blade there are others two angle:

- the blade twist θ_T;
- the blade pitch angle at the tip $\theta_{p,0}$.

The blade twist angle is defined relatively to the blade tip, this means that a relationship exists between the section pitch angle, the twist angle and the pitch angle at the tip:

$$\theta_T = \theta_p - \theta_{p,0} \tag{2.38}$$

$\theta_T$represents the inclination of the tip of the blade with respect the plane of rotation. Then from figure 2.10 it is possible to find the following relationships by geometry:

$$tan\varphi = \frac{U(1-a)}{\Omega r(1+a')} = \frac{(1-a)}{(1+a')\lambda_r} \tag{2.39}$$

which connects the angle of relative wind φ with the two induction factors and the local tip speed ratio.

From the definition of the Lift force:

$$L = \frac{1}{2}\rho c C_l U_{rel}^2 \tag{2.40}$$

and the Drag force:

$$D = \frac{1}{2}\rho c C_d U_{rel}^2 \tag{2.41}$$

Because the important forces are those normal and tangent to the rotor plane it is necessary to project the lift and drag in these directions:

$$p_N = Lcos\varphi + Dsin\varphi \tag{2.42}$$

and:

$$p_T = Lsin\varphi - Dcos\varphi \tag{2.43}$$

The equations (2.42) and (2.43) are normalized with respect $\frac{1}{2}\rho c U_{rel}^2$. Using the drag and lift coefficient it is possible to find out the normal and tangential coefficient.

$$C_n = C_l cos\varphi + C_d sin\varphi \tag{2.44}$$

$$C_t = C_l cos\varphi - C_d sin\varphi \tag{2.45}$$

The C_n and C_t coefficients can be defined in another way to be directly dependent on the normalized tangential and normal force:

$$C_n = \frac{p_n}{\frac{1}{2}\rho c V_{rel}^2} \tag{2.46}$$

and:

$$C_t = \frac{p_t}{\frac{1}{2}\rho c V_{rel}^2} \tag{2.47}$$

From the blade geometry we are able to find the relative velocity:

$$U_{rel}sin\varphi = U(1-a) \tag{2.48}$$

or, in another way:

$$U_{rel}cos\varphi = U(1+a') \tag{2.49}$$

Further, the solidity σ is define as the fraction of the annular area that is covered by the blades:

$$\sigma(r) = \frac{c(r)B}{2\pi r} \tag{2.50}$$

in which B is blade number, $c(r)$ is the local chord dependent on the radial position r of the control volume. Since p_T and p_N are forces per length, the normal force on the control volume of thickness dr is:

$$dT = Bp_N dr \tag{2.51}$$

The torque can be found starting directly from the tangential normalized force:

$$dM = rBp_T dr \tag{2.52}$$

If substitute equations (2.46) for p_N and (2.48) for U_{rel} we can find a new expression of the thrust:

$$dT = \frac{1}{2}\rho B \frac{U^2(1-a)^2}{sin^2\varphi} cC_n dr \tag{2.53}$$

In similar way, it is possible to apply the same procedure for torque using equations (2.47) for p_T and (2.49) for U_{rel}:

$$dM = \frac{1}{2}\rho B \frac{U(1-a)\omega r(1+a')}{sin\varphi cos\varphi} cC_t r dr \tag{2.54}$$

To find out the BEM theory, the coupling of the 1-D momentum theory equations and those of the blade theory is necessary. The 1-D momentum theory refers to a control volume analysis at the blade based on the conservation of linear and angular momentum while, the blade theory refers to an analysis of forces at

a section of the blade, as function of the blade geometry. Connecting both theories all the information and the equation are available to built the BEM theory.

2.3 BEM theory

Blade element momentum theory (BEM), as defined in [6], combines 1-D momentum theory, that refers to a control volume analysis of the forces at the blade, based on the conservation of linear and angular momentum, and the blade element theory that refers on the force analysis at a section of the blade, as a function of a blade geometry.

With these two theories we are able to have a general method to design a turbine. Therefore, coupling the equations (2.23) and (2.53) allow to find an alternative expression of the axial induction coefficient:

$$a = \frac{1}{\frac{4sin^2\varphi}{\sigma C_n}+1} \tag{2.55}$$

If the equations (2.26) and (2.54) are combined the expression for a' yields:

$$a' = \frac{1}{\frac{4sin\varphi cos\varphi}{\sigma C_t}-1} \tag{2.56}$$

Once we derive all the necessary equations, it is possible to apply a numerical method in order to design the blade. The design algorithm can be summarized in 8 steps. Since the different control volumes are assumed to be independent, each strip can be treated separately and the solution for one radius can be computed before solving for another radius. For each control volume, the following algorithm is applied.

BEM algorithm	
Step 1	Initialized a and a', tipically $a = a' = 0$.
Step 2	Compute the flow angle using equation (2.39).
Step 3	Compute the local angle of attach using equation (2.20).
Step 4	Read off $C_l(\alpha)$ and $C_d(\alpha)$ from table.
Step 5	Compute C_n and C_t from equations (2.44) and (2.45) respectively.
Step 6	Calculate a and a' from equations (2.55) and (2.56).
Step 7	If a and a' are changed more than a certain tolerance go to step(2) or else finish.

Step 8	Compute the local loads on the segment of the blades.

Table 2.1 *BEM algorithm steps*

This is the principle of the BEM theory but in the algorithm two corrections are necessary in order to obtain good results:

- Prandt's tip loss factor that correct the assumption of infinite number of blades;
- Glauert correction that is an empirical relationship that modifies the calculation of the thrust coefficient in case the axial induction factor a is greater than approximately 0.4.

2.3.1 Prandtl's tip loss factor

Because the vortex system in the wake of a rotor with finite number of blades is different from the one with infinite number, Prandtl introduces a correction factor F:

$$F = \frac{2}{\pi} cos^{-1}(e^{-f}) \tag{2.57}$$

where the factor f can be computed as:

$$f = \frac{B(R-r)}{2rsin\varphi} \tag{2.58}$$

in which B is the blade number, R is the total radius of the rotor, r is the local radius and φ is the flow angle. Once the correction factor is defined it is possible to calculate the axial and angular induction factor:

$$a = \frac{1}{\frac{4Fsin^2\varphi}{\sigma C_n}+1} \tag{2.59}$$

and:

$$a' = \frac{1}{\frac{4Fsin\varphi cos\varphi}{\sigma C_t}-1} \tag{2.60}$$

In step(6) of the iterative algorithm, instead of using equations (2.55) and (2.56) we need to use equations (2.59) and (2.60). Therefore an extra step in the algorithm is needed in order to calculate the Prandtl's tip loss factor F and it should be put after step(2).

2.3.2 Glauert correction for high values of a

When the axial induction factor becomes larger than approximately 0.4 the 1-D momentum theory is not able to describe correctly the behavior of the thrust factor C_T because the wind speed in the far wake would be negative.

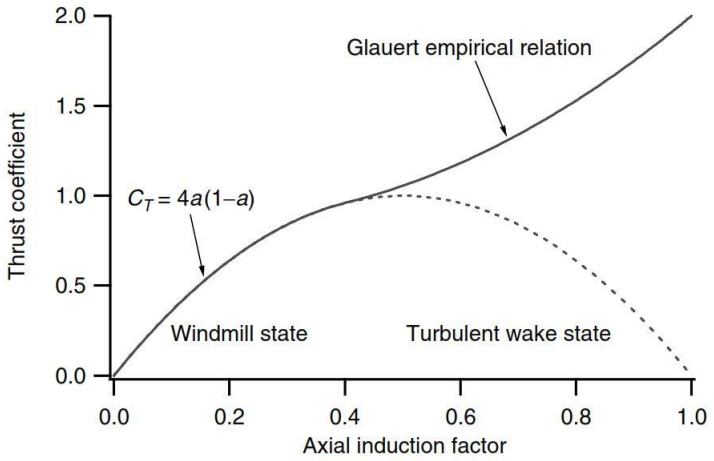

Figure 2.11 *Wind turbine thrust coefficient with and without Glauert correction [7]*

Therefore, some empirical expression are provided and the one used to correct the value of the axial induction factor is the following:

$$C_T = \begin{cases} 4a(1-a)F & a < a_c \\ 4(a_c^2 + (1-2a)a)F & a > a_c \end{cases} \tag{2.61}$$

Considering the thrust expression (2.53) and rework it in order to obtain the thrust coefficient yields:

$$C_T = \frac{(1-a^2)\sigma C_n}{sin^2\varphi} \tag{2.62}$$

Putting together the second expression of the equation (2.61) and the equation (2.62) yields:

$$a = \frac{1}{2}[2 + K(1-2a_c) - \sqrt{(K(1-2a_c)+2)^2 + 4(Ka_c^2 - 1)}] \tag{2.63}$$

where:

$$K = \frac{4Fsin^2\varphi}{\sigma C_n} \tag{2.64}$$

Therefore, another step is needed in order to compute the Glauert correction factor. The final algorithm comprehensive of the two correction already introduced is in table

BEM Algorithm	
Step 1	Initialized a and a', tipically $a = a' = 0$.
Step 2	Compute the flow angle using equation (2.39).
Step 3	Compute Prandtl's correction factor using equation (2.57) and (2.58).
Step 4	Compute the local angle using equation (2.20).
Step 5	Read off $C_l(\alpha)$ and $C_d(\alpha)$ from table.
Step 6	Compute C_n and C_t from equations (2.44) and (2.45) respectively.
Step 7	Calculate a and a' from equations (2.59) and (2.60).
Step 8	If a exceed 0.4, compute Glauert correction using equation (2.64) and (2.63).
Step 9	If a and a' are changed more than a certain tolerance go to step(2) else finish.
Step 10	compute the local loads on the segment of the blades.

Table 2.2 *BEM algorithm steps including Prandtl and Glauert correctinos*

2.3.3 Optimization

Having derived all the necessary equations to compute a given wind turbine, it possible to compute an optimum design. First, an optimum design must be defined, evaluating the optimization purpose. In the present study the aim of the optimization is the achievement of the maximum efficiency at the design wind speed.

First of all, having C_l and C_d data we need to calculate the maximum efficiency as:

$$eff = max(\frac{C_l}{C_d}) \tag{2.65}$$

of the selected blade. Once the efficiency is obtained it is possible to find out the optimum angle of attack α_{opt} correspondent to the maximum efficiency, because we have a direct dependency between α and the lift and drag coefficients. Then from an optimization algorithm the optimized lift and drag coefficients, $C_{l,opt}$ and $C_{d,opt}$ respectively, can be derived. Since the optimum angle of attach, α_{opt}, is choesen the flow remains attached to the blades and the equations (2.25) and (2.33) remain valid, as said in [6], and can be combined to give an optimum relationship between the local tip speed ratio λ_r and the axial induction factor a:

$$16a^3 - 24a^2 + a(9 - 3\lambda_r^2) - 1 + \lambda_r^2 = 0 \qquad (2.66)$$

Consequently, the optimum value of a' is found using equation (2.33). Furthermore, optimum flow angle, φ_{opt} is derived from equation (2.39), in which the inputs are the optimize axial and angular induction factor. One the optimum flow angle and the optimum angle of attach are derived, the optimize twist of the blade can be calculated through the section pitch angle:

$$\theta_{p,opt} = \varphi_{opt} - \alpha_{opt} \qquad (2.67)$$

Considering the relation between the blade pitch angle, the section blade pitch angle and the twist described by equation (2.38), imposing a blade pitch angle equal to zero the twist corresponds directly to the section blade pitch angle. After, as last optimization step, the normal coefficient can be calculated using equation (2.63) giving in input the optimize flow angle:

$$C_n = C_{l,opt} cos\varphi_{opt} + C_{d,opt} sin\varphi_{opt} \qquad (2.68)$$

Finally, the optimum chord can be derived after the number of blade, B, is fixed:

$$\frac{c(r)}{R} = \frac{8\pi a \lambda_r sin^2\varphi}{(1-a)BC_n\lambda} \qquad (2.69)$$

Therefore, the optimization process works in favor of the BEM model since provides the BEM inputs such the optimized chord and the optimized twist that are necessary to design the blade that maximize the performance.

3 Design

In this chapter the previously described BEM model is applied to design a centimeter scale turbine. The points of discussion are related to the fundamental parameters that characterize the project of the turbine, the objective, the constraint, the numerical limitation of the model and the construction procedure. Power and power coefficient results are presented and discussed in the following paragraphs.

3.1 Objectivess and constraits

Before starting the numerical analysis of the cm-scale turbines, it is important to fix the constraints to have a clear idea on which are the logical steps that brings to the final design. First, the turbine needs to be installed on a freight train, therefore, the wind velocity is represented by the relative speed between the train and the ambient air.

In the literature, in most of the applications, as seen in [3], [5] in paragraph 1.2.2, the centimeter turbine is positioned in a duct where the air velocity is almost constant and does not reach high speed (the maximum value in an air ventilation duct is 12 m/s); there is no dust, it is not exposed to environmental phenomena like snow and storm. In other applications, as explained in [8], the turbine is positioned under a bridge using the environment wind characterized by an average speed of 5 m/s. In all these applications the air moves in one case forced in a ventilation duct, in the other, the energy comes from the atmospheric wind.

In the present study, the purpose is to force the turbine to work in a wide range of wind velocity, due to the movement of the train, maximizing the power coefficient at the lower design wind speed. Taking this into account, the range of velocity application in which the turbine need to extract energy goes from 10 m/s to 30 m/s that are, respectively, the minimum velocity below which it is acceptable that the turbine cannot produce and the maximum velocity of the freight train. Therefore, in case the wind speed is 10 m/s, it is important to design the blade in order to maximize the power coefficient such that the turbine can produce as much power as possible; while, at 30 m/s, even if the turbine is not optimized, there is sufficient available power to feed a sensor due to the increase of the available power increasing the wind velocity, as explained in equation (2.13). Once the wind design velocity is fixed, there are others constraints regarding:

I. the maximum rotational speed;
II. the tip speed ratio;

III. the fabrication.

The reduction in rotor size leads to an increase in rotational speed, hence, it is important to limit the rpm in order to select an available commercial generator.

The first step is the selection of the tip speed ratio to obtain high power coefficient; in fact, as explained in [7], the increase of the TSR enhances the power coefficient. Based on the theory [6] and on the literature, especially on [1], it was selected TSR equal to 1: this value is the lower limit to obtain optimum power coefficient and, as seen in figure 1.5, it seems a feasible value for centimeter wind turbines on which design the blade to obtain the maximum efficiency. Afterwards, the rotor diameter must be selected. The choice is done using the equation (3.1):

$$R = \frac{TSR\ U}{\omega} \tag{3.1}$$

where the rotational speed is derived from the fixed maximum rpm of the generator. A reasonable value is supposed equal to 5000 rpm. The design velocity of wind is selected as 10 m/s. From the equation (3.1), a rotor radius of 2 cm is derived. However, the radius calculation need to pass through considerations regarding the minimum Reynolds number at the tip, and fabrication issues.

Another important factor to be considered in the design phase is the expected Reynolds number value for the cm-scale rotor. Small dimension wind turbines have to work with low Reynolds number, but it is important to maintain the Reynolds above $3 * 10^5$ at least near the blade tip in order to have reliable airfoil polars [11]. The minimum chord can be calculated through equation (3.2):

$$Re = \frac{\rho V_{rel} c}{\mu} \tag{3.2}$$

V_{rel} takes into account the wind speed, U, and the rotor rotational velocity, $V_{rot} = \omega R$; ρ is the air density, μ is the viscosity of the air, c corresponds to the chord and Re represents the Reynolds number. Therefore, fixed the Reynolds at the minimum admissible value at the tip, correspondent to $3 * 10^5$, the chord is calculated and results equal to 2 cm, that is sufficient to overcome the fabrication issues. Hence, validating the turbine's dimension early derived, a rotor diameter of 4 cm is selected.

Because the final application requires a compact device, another rotor diameter is investigated: 3 cm rotor diameter. A decrease in diameter causes an increase in rotational velocity in order to maintain TSR equal to 1 at the same wind speed, equation (3.1). The 3 cm design starts through a backward procedure using equation (3.2); the chord can be derived and it reduces but it is similar to the 4 cm turbine chord because the

relative velocity remains almost constant and the Reynolds number is fixed. Therefore, two turbines are designed: one with a rotor diameter equal to 4 cm and another with a rotor diameter equal to 3 cm.

3.2 Airfoil horizontal axis wind turbine

3.2.1 Main characteristics

The propeller used is the SD7032 which maximum thickness is equal to 9.6% of the chord length and the blade has chamber angle. It defines the thicknesses and their distribution, asymmetric along the chord, of airfoil (see figure 3.1).

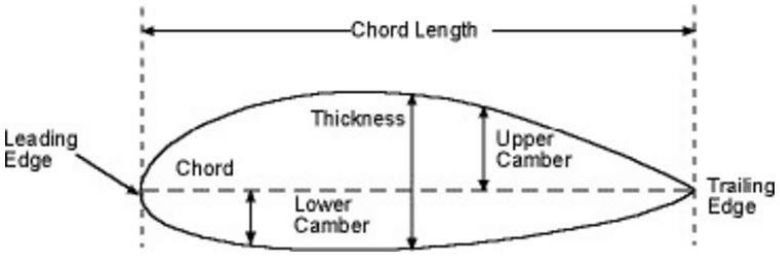

Figure 3.1 *Schematization of an airfoil [11]*

Figure 3.2 shows a sketch of the SD7032 airfoil used in BEM model to design the cm-turbines.

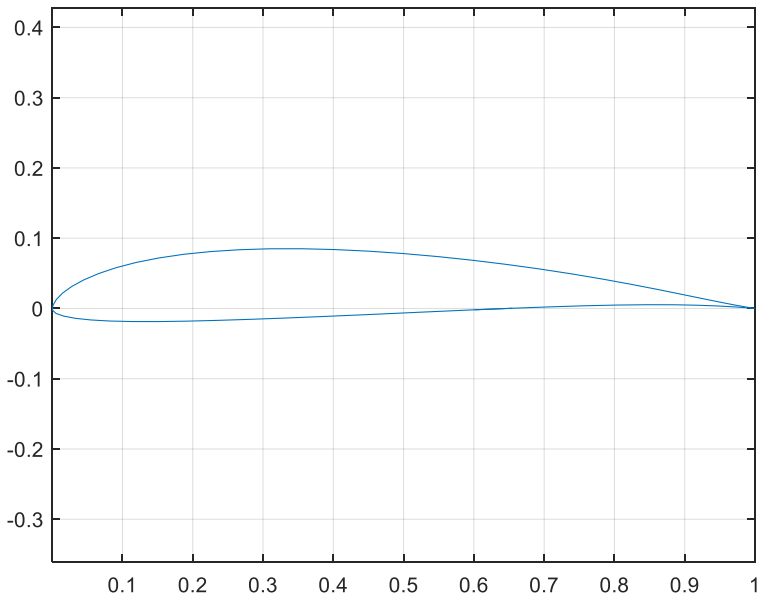

Figure 3.2 *Sketched of SD7032 airfoil used to design the turbines*

Adopting the reference system introduced in figure (1.2) lift and drag coefficient are evaluated in the range of Reynolds number of $3 * 10^5 - 1 * 10^6$. The coefficients are determined for a small range of the angle of attach, α, from -4° to 18°. Therefore, in order to cover a wider angle domain, the polars are numerically extended using the standard viterna extrapolation method [12] between -180° and 180°, see figure (3.3).

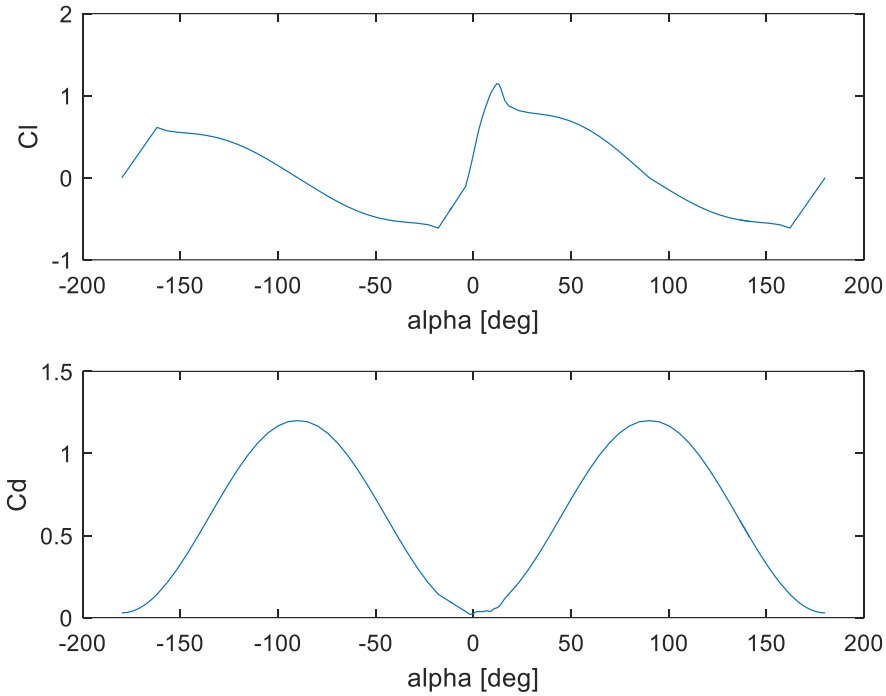

Figure 3.3 *Lift and Drag coefficient as function of the angle of attach for Re=3*10^5*

After that it is important to select the number of blades because they influence the optimum chord distribution along the radius, as seen in the equation (2.69), and influence the power coefficient (see figure 3.4).

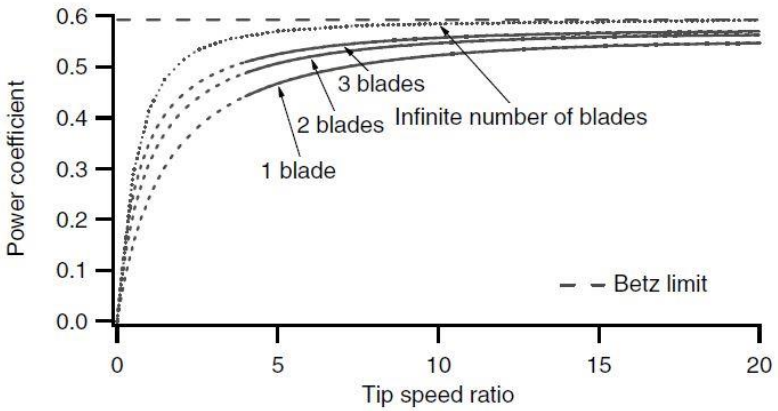

Figure 3.4 *Influence of the blade number on the power coefficient for large-scale wind turbine [7]*

Therefore, a reasonable 4 blades wind turbine is selected. The choice is given by the project objective: the goal is the optimization of the power coefficient that can be achieved using 4 blade. The addition of other blades cannot provide a significant contribution to the power coefficient increase, see figure 3.4. In addition, because the tip speed ratio is fixed and equal to 1, the turbine has high solidity meaning that large surface of the rotor needs to be covered by the blades. Therefore, the choice is: less number of blades but with higher chord length, or large number of blades with a reduced chord. In this study, the preference choice is the second, hence, the turbines are design with 4 blades.
Once the number of blades, the TSR, the design velocity and the radius of rotor diameter are selected, they can be given in input to the BEM algorithm. The algorithm implements the following procedure:

- optimization process: it is based on the polar efficiency curve, obtained by the ratio Cl/Cd, as a function of the angle of attach, α. Entering in the curve with the maximum efficiency value, it is possible to find the corresponding angle of attach α_{opt} (figure 2.10) and, consequently, the lift and the drag coefficient values. After, the optimum flow angle and the optimum axial and tangential factors are researched. Then, having the optimum flow angle, φ_{opt} (figure 2.10), and the optimized angle of attach, it is possible to extract the optimize blade twist and then, thanks to equation (2.69), the optimized chord distribution along the radius of the blade. The inputs of the optimization process are reported in table 3.1.

Optimization process input
1. Polar efficiency curve
2. Optimum angle of attach
3. Wind design speed
4. The design TSR
5. The rotor radius

Table 3.1 *Optimization process inputs*

- BEM iteration process: using the steps described at paragraph 2.3.2, it is possible to calculate the power production, the power coefficient, the torque and the force applied along the blade of the turbine. The inputs of the BEM algorithm are described in the following table 3.2.

BEM iteration process input

6. the velocity of the wind on which the performance of the turbine wants to be evaluated
7. the range of rotational velocity of the generator
8. the optimum chord and twist determined in the optimization procedure.

Table 3.2 *BEM iteration process inputs*

3.2.2 Modified BEM numerical model

The previously described BEM iteration process presents an issue. Because BEM model is normally used for large-scale wind turbines, when the turbines are scaled until centimeter size the tangential induction factor causes problems of numerical convergence when some parameters overcome a certain limit. For example, when the TSR is equal to 1 or it is fixed below the unity value, the tangential induction factor start to produce unreasonable results inducing a convergence problem of the numerical model. Obviously, this problem influences the numerical results of the power and power coefficient. A method to limit the problem is to switch off the calculation of the tangential induction factor as defined in equation (2.60), imposing it equal to zero. However, to neglect the tangential induction factor means to ignore part of the physic of the model because the tangential induction factor is present as a reaction of the air to the rotational movement of the turbine. In figure 3.5 is sketched the difference in terms of power coefficient for BEM numerical model with and without tangential induction factor.

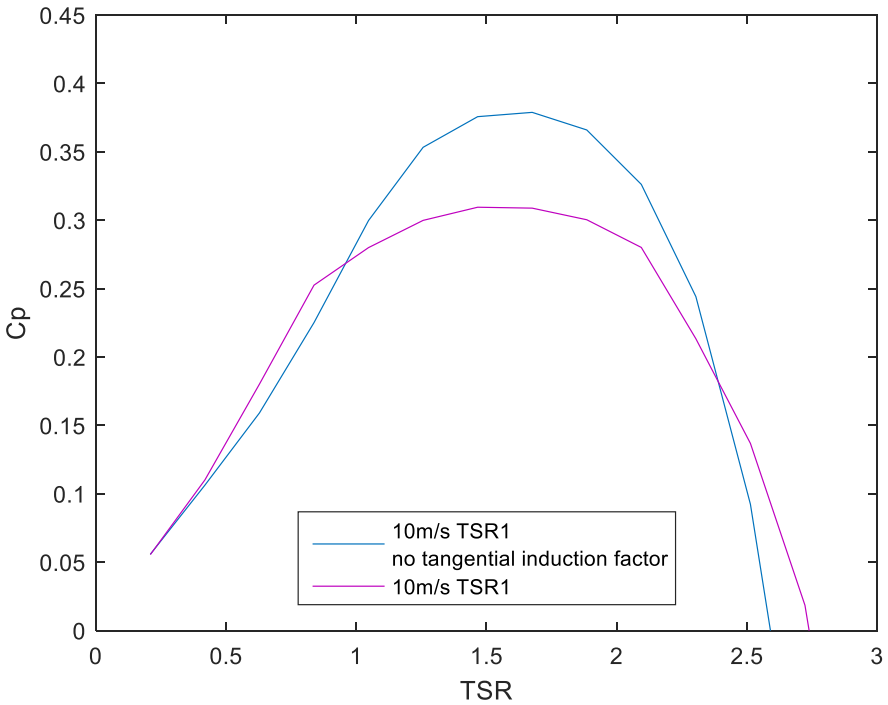

Figure 3.5 *Cp vs TSR of a 4 cm wind turbine with and without the presence of the tangential induction factor*

The power coefficient is higher because, without the tangential induction factor, the velocity component (see figure 2.7), that is opposed to the rotational speed of turbine's rotor, is neglected.

3.2.3 Numerical results

The numerical results are presented for both 3 cm and 4 cm turbines for reference wind speeds: 10 m/s, 20 m/s and 30 m/s (see figures 3.6-3.9).

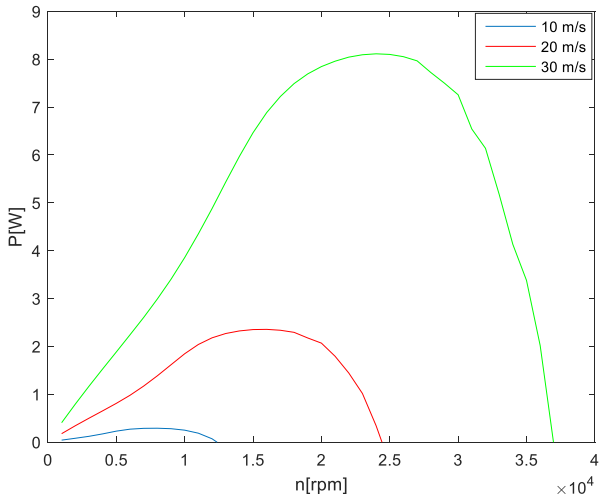

Figure 3.6 *Numerical results Cp vs TSR of a 4 cm airfoil wind turbine*

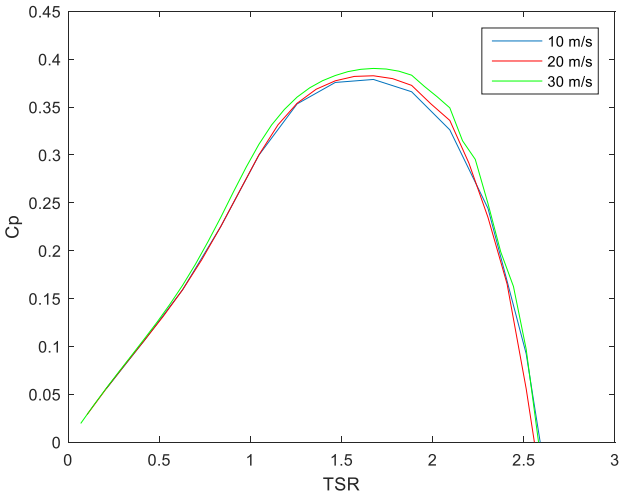

Figure 3.7 *Numerical result Cp vs TSR of 4 cm airfoil wind turbine*

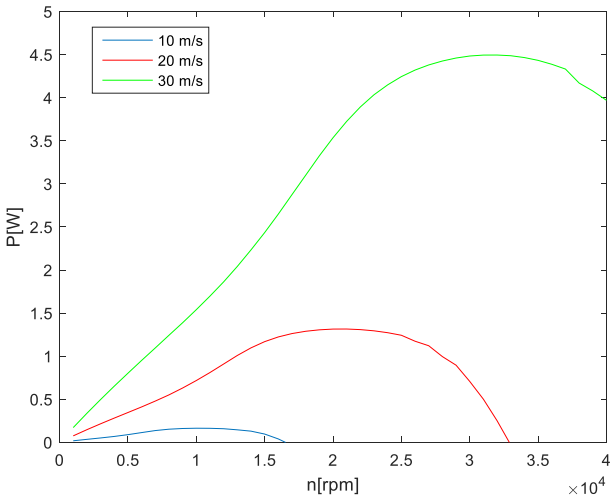

Figure 3.8 *Numerical result Pvs RPM of 3 cm airfoil wind turbine*

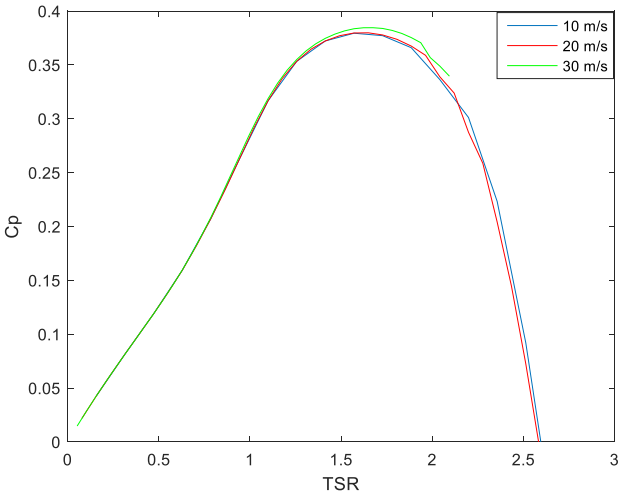

Figure 3.9 *Numerical result Cp vs TSR of 3 cm airfoil wind turbine*

Finally, after the modification applied on the numerical BEM model, the algorithm provides the sketch of the design blade surface, useful to model the entire turbine by CAD, see figures 3.10-3.13.

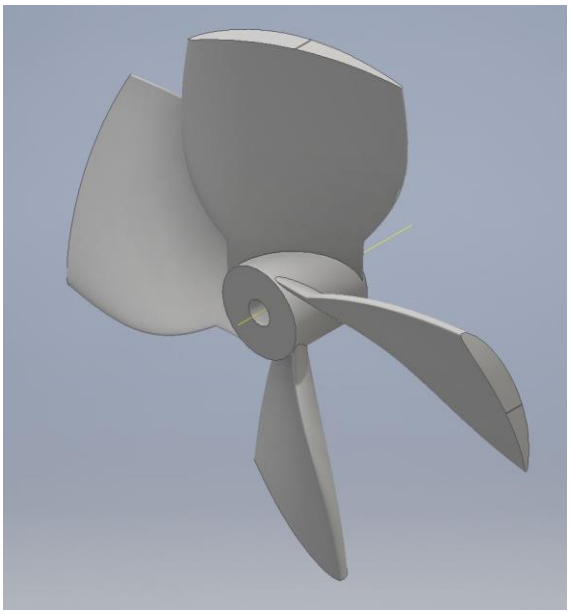

Figure 3.11 *Front view of 4 cm airfoil wind turbine3D model*

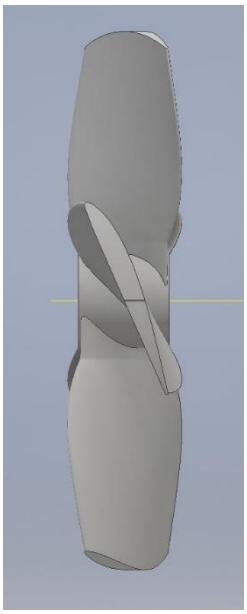

Figure 3.10 *Lateral view of 4 cm airfoil wind turbine 3D model*

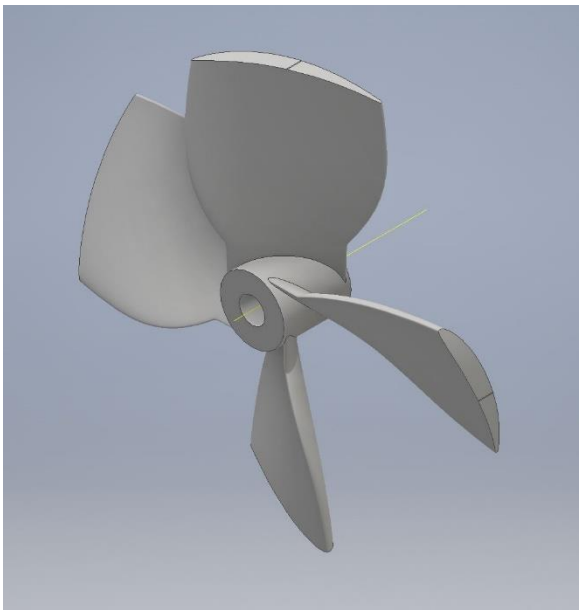

Figure 3.13 *Front view of 3 cm airfoil wind turbine 3D model*

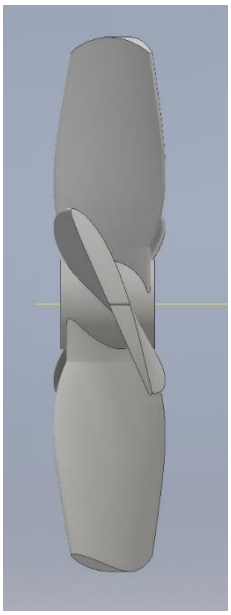

Figure 3.12 *Lateral view of 3 cm airfoil wind turbine 3D model*

As can be seen, the 3 cm turbine is only a scaled version of the 4 cm. In fact, they have the same twist and the same chord distribution along the blade, see in figures 3.14-3.17.

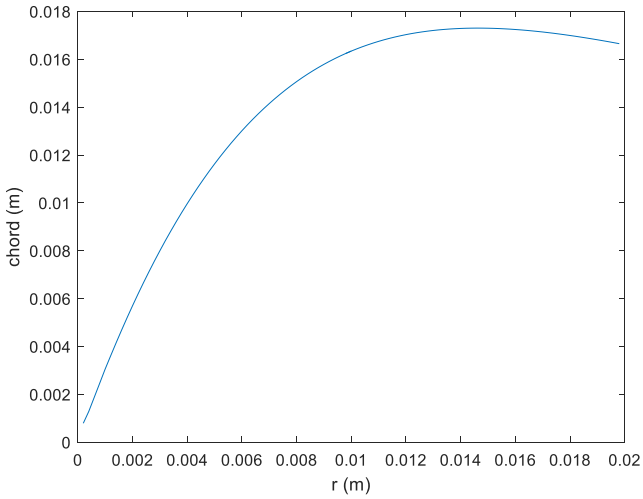

Figure 3.15 *Chord variation along the blade radius of 4 cm airfoil wind turbine*

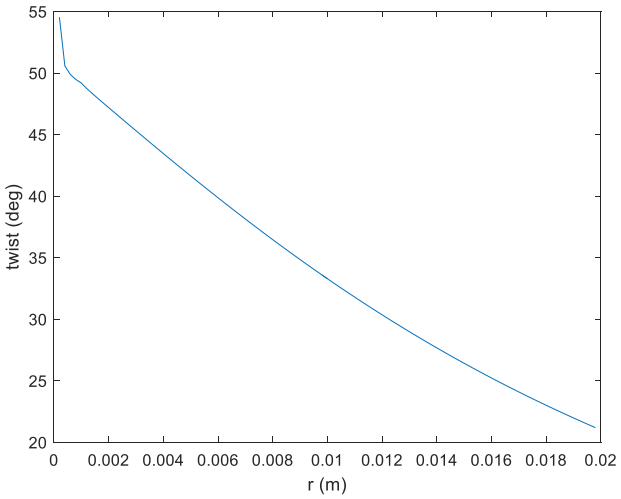

Figure 3.14 *Twist variation along the blade radius of 4 cm airfoil wind turbine*

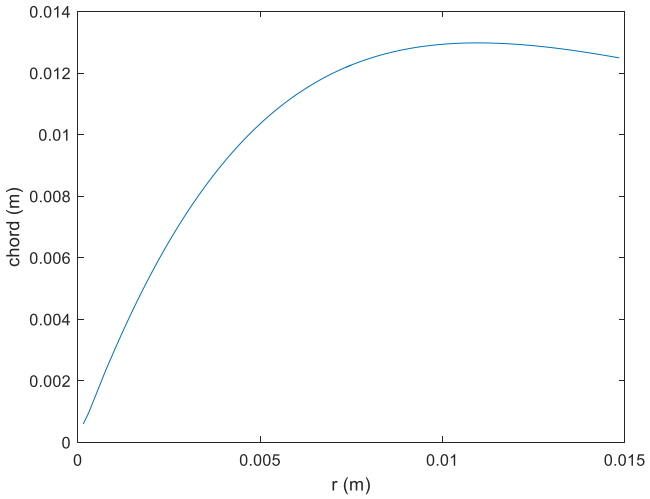

Figure 3.17 *Chord variation along the blade radius of 3 cm airfoil wind turbine*

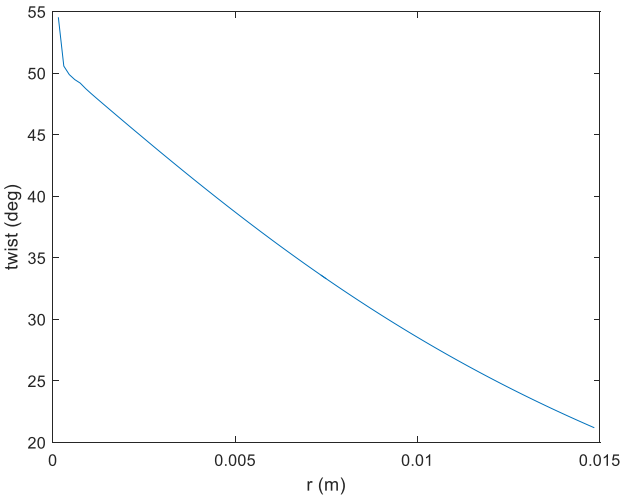

Figure 3.16 *Twist variation along the blade radius of 3 cm airfoil wind turbine*

Then, it is possible to impose the wind velocity on which having the results about the power production and the turbine's performance.

Table 3.1 gives an idea of the numerical peak performances in terms on power and power coefficient for both wind turbines.

Wind speed [m/s]	4 cm airfoil wind turbine		3 cm airfoil wind turbine	
	P [W]	Cp	P [W]	Cp
10	0.29	0.378	0.16	0.38
20	2.36	0.383	1.32	0.38
30	8.11	0.39	4.5	0.385

Table 3.3 *Power and power coefficient for different wind speed*

3.3 Symmetric turbine profile

3.3.1 Objective and constraint

In the previous section, the 4 cm and 3 cm airfoil wind turbine are discussed and analyzed, assuming that the wind has fixed direction with respect the turbine, see figure 3.18.

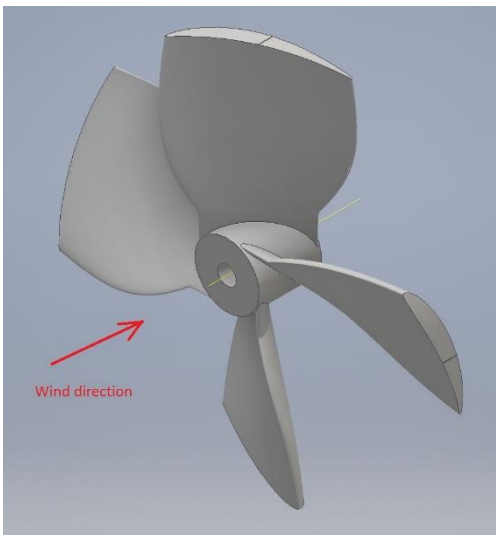

Figure 3.18 *Airfoil wind turbine correctly positioned with respect the wind direction*

In the final application, the wind turbine needs to extract energy in both wind directions, since the wind direction is given by the direction of the freight train's movement, the airfoil is not adapt because it produces correctly and efficiently only when the air comes from the correct direction of the propeller, see figure 3.18. Hence, in order to guarantee the correct mode of operation in both wind directions, a symmetric profile is designed. The diameter was kept equal to 4 cm.

3.3.2 Symmetric design

The airfoil shape for the symmetric rotor is built from a rounded square, see figure 3.19, having a thickness equal to 3.5% of the blade length.

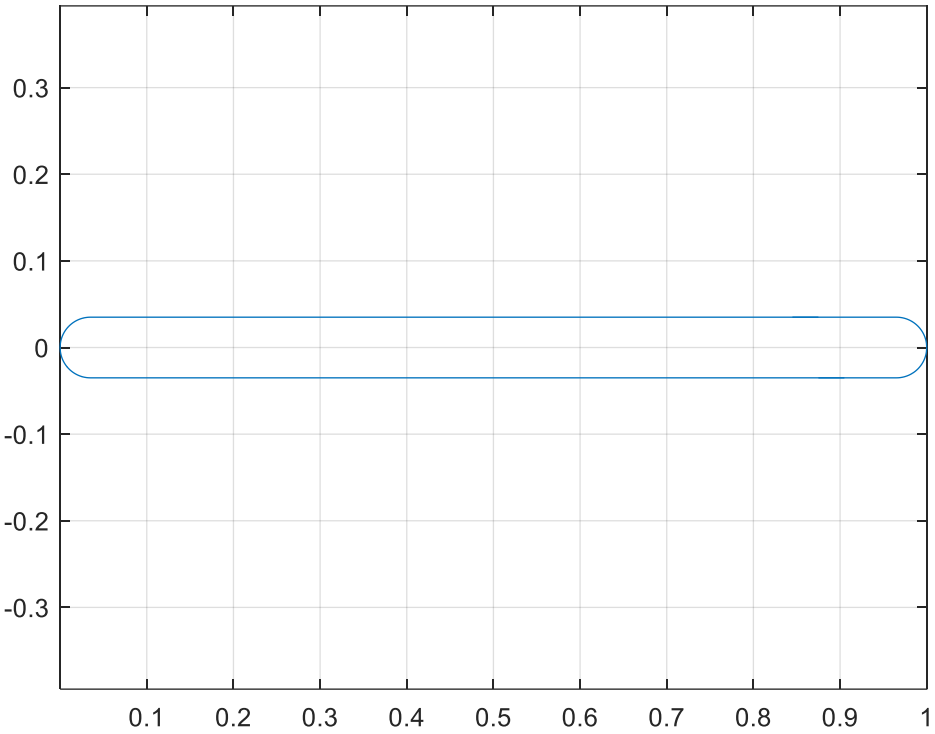

Figure 3.19 *Symmetric profile sketch used to design the symmetric turbine*

The 4 cm symmetric turbine maintains the same chord distribution of the 4 cm airfoil blade, see figure 3.15. The twist is imposed to be zero. The blade has a pitch angle equal to 45°. The choice derives from the polars of the flat plate blade that maximized the lift coefficient for an angle of attack, α; equal to 20°, see figure 3.20.

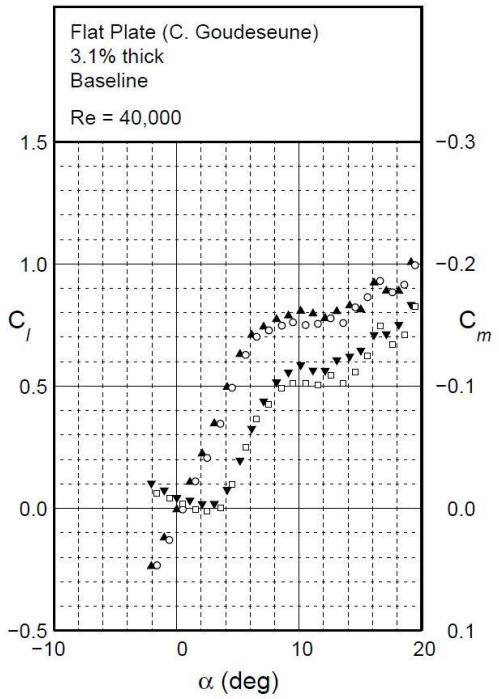

Figure 3.20 *Flat plate lift coefficient as a function of the angle of attack α [14]*

Knowing the flow angle φ from the optimization process, using equation (2.20) the pitch angle can calculated and at the blade tip the it equal is equal to 43°.

As for the airfoil profile, the BEM algorithm gives in output the surface of the blade useful for CAD design of the entire turbine (see figures 3.21-3.22). But unfortunately, because the polars of the symmetric profile are not experimentally characterized, the numerical performance results are not available. Therefore, the turbine characterization must be done experimentally as illustrated in chapter 4.

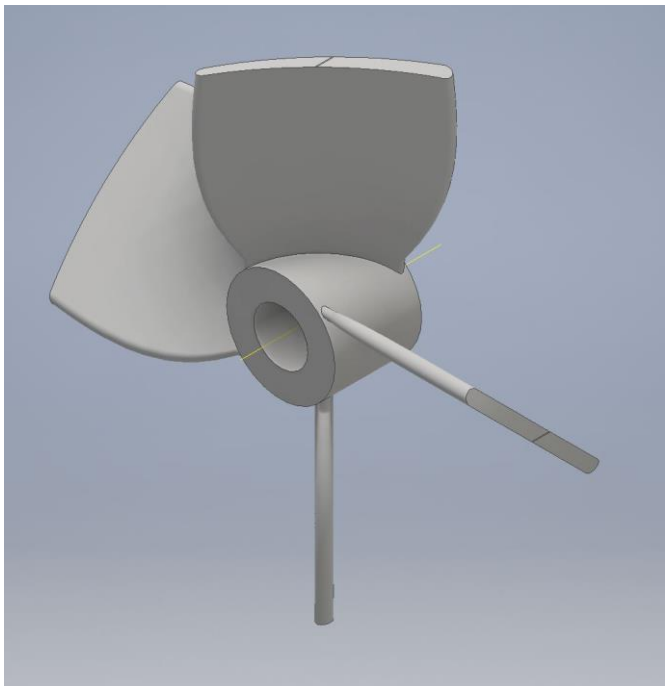

Figure 3.22 *Front view of 4 cm symmetric profile wind turbine 3D model*

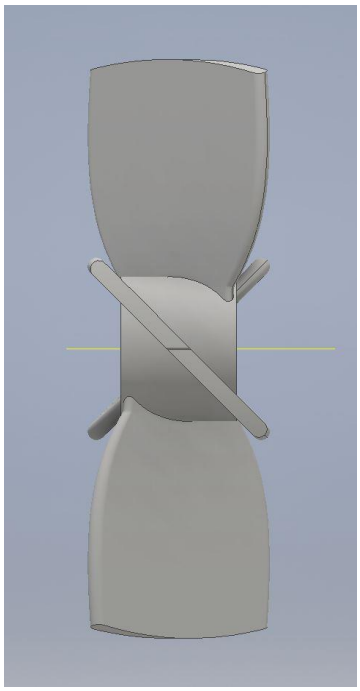

Figure 3.21 *Lateral view of 4 cm symmetric profile wind turbine 3D design*

3.4 Ducted wind turbine

3.4.1 Motivations

Since the turbines must be mounted on a freight train they will be subjected to storm, snow, dust, rocks and other environmental phenomena. For this reason a duct is useful, also, to guarantee the preservation of the turbine.

3.4.2 Diffuser analysis and design

IN order to maximize the power production of the ducted turbine a diffuser is studied, starting from the researches presented in literature. Jafari [13] gives guidelines to understand the principals of power augmentation and the related limits of application of simple frustum diffuser. The paper evidences the geometrical characteristics of a diffuser able to enhance the performance of the turbine.

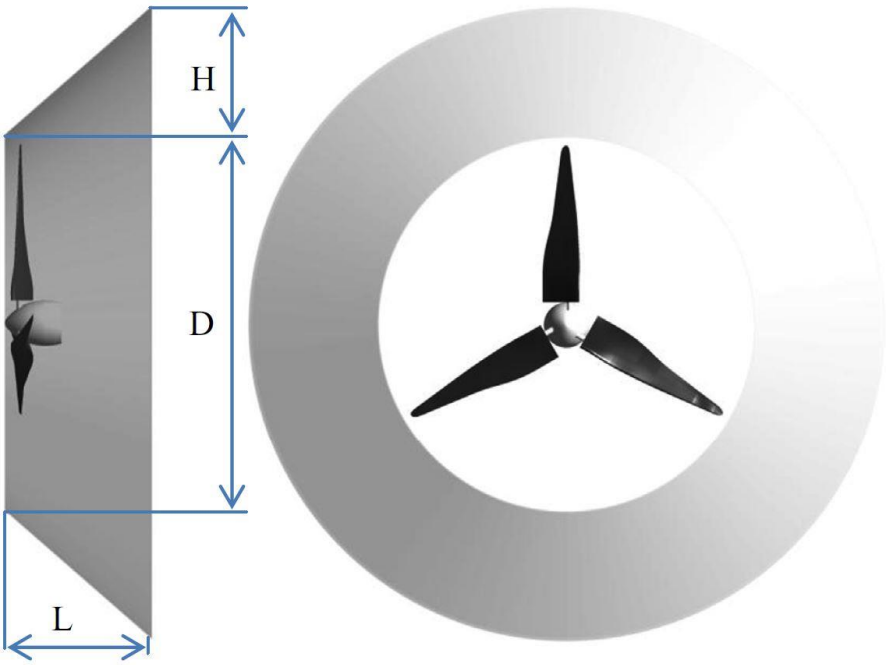

Figure 3.23 *Dimension of simple frustum diffuser [13]*

As explained in [13], the performances are evaluated in terms of H/D and L/D parametrization, see figure 3.23. The principle behind the study is related to the geometry of the diffuser, that force the flow downstream to expand through the diffuser. The expansion reduces the pressure at the outlet of the diffuser and causes an increase in the mass flow at the inlet due to the higher pressure drop between inlet and outlet. An increase of a mass flow through the rotor means an increase of power production. This effect is called "back pressure effect".

Furthermore, the sub-atmospheric pressure created at the outlet of the diffuser also lowers the air pressure at the suction side of the rotor blades, which creates greater lift on the blades. The study evidences that the increasing of ratio H/D beyond a certain limit is counter-productive, in fact higher is the back pressure due to H/D increment, earlier the flow separates, causing a reduction of the power. To compensate this effect, it is possible to increase the length L of frustum diffuser increasing consequently the ratio L/D. Doing so, it is possible to obtain a decrease separation surface but also higher viscous losses. However, viscous losses can be neglected when the diffuser is very short. Even within a long diffuser, viscous losses effect might be dominated by the back pressure effect. After these considerations, in [13], optimum length L and an optimal outer radius diameter H are established in a combine range of L=0.03-0.04D and H=0.1-0.15D to increase the power output from the wind.

3.4.3 Components

The final application requires the use of a compact system including, the duct in which the turbine and the generator are positioned, and the acquisition card. The minimum length is imposed by the card that is 145 mm length while the duct is a parallelepiped with a square section of 55 mm, with an internal radius of 42 mm based on the 4 cm turbine rotor diameter. The motor and the turbine inside the tube are sustained by a motor support properly design; it is attached to the tube wall by a tower with an airfoil profile in order to have the lowest impact on the airflow passing through the duct.
The tube realization is accomplished through a modular approach, because of the evaluation of parameters influence on the power harvested, like:

1. The duct length;
2. The turbine position;
3. Type of divergent/convergent used at the inlet or at the outlet.

The duct is divided in four pieces and the logic behind the partition is related to the dimension of the base block (module B) in figure 3.26. It is designed to host only the motor support (see figure 3.30), and it is the module connected to the wind tunnel support.
In following table 3.4 are presented the main dimension of the module B.

	Module B
Length [mm]	62
Duct radius [mm]	42

Table 3.4 *Main characteristic dimension of module B*

Therefore, the size of the remaining modules is determined by:

- the turbine: the modules with divergent shape (module D and module E) are dimensioned in order to host the turbine and they have a length comparable with the rotor height and the design parameter L/D.
- The motor nozzle: at the rear part, the motor support needs to be closed by a top that has a nozzle shape. Once it is mounted on the motor support, it increases the support length that overcomes the dimension of the B module. Therefore, another block is added (module A) in order to increase the length of the tube and to cover the nozzle-support system and promote the wake motor closing to enhance the performance.

Finally once the modules A, B, D and E are determined, the module C, that is only a straight tube, is dimensioned in order to reach the minimum duct length.

Module A represented in figure 3.29, has a length of 18 mm and an internal radius equal 42 mm. it is design only as a straight tube in order be mounted at the outlet/inlet (in upwind or downwind respectively, depending on the turbine arrangement) of the tube.

Module D and E correspond to the diffuser shown in figure 3.27 and figure 3.31 respectively, and they are designed to hots the turbine in order to increase its power production. The main characteristics are summarized in table 3.5.

	Module D	**Module E**
Length [mm]	18	22
H/D	0.1	0.1
L/D	0.3	0.4
Duct radius [mm]	42	42

Table 3.5 *Main characteristics of module D and module E*

In table 3.5 the ratios H/D and L/D are the non-dimensional parameters described in the paragraph 3.4.2 that characterize the design of the diffuser. Their choice is related to the performance that are able to guarantee. As shown in figure 3.24, the power exhibits a maximum for H/D equal to 0.1 for both the curved described by the ratio L/D equal to 0.3, in case of module D, and equal to 0.4 in case of module E.

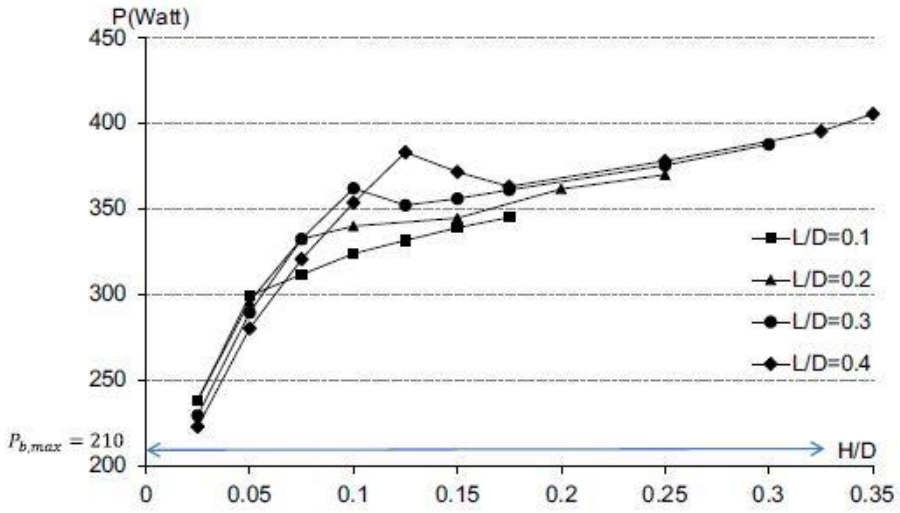

Figure 3.24 *Maximum power output of the turbine model shrouded by diffuser with different L/D and H/D [13]*

In figure 3.25, as confirmation of good performance of the selected $^{L}/_{D}$, the power coefficient in correspondence of $^{H}/_{D}$ equal to 0.1, is more stable with respect the others.

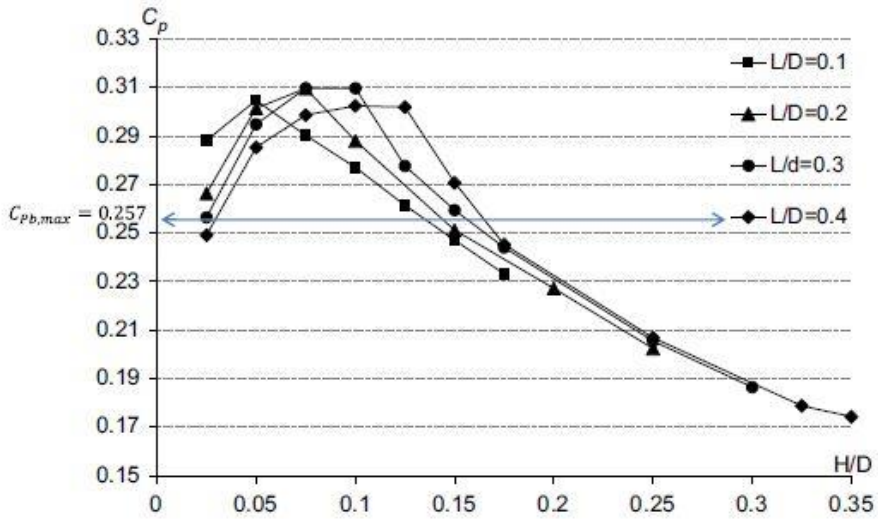

Figure 3.25 *Maximum Cp of the turbine model shrouded by diffuser with different L/D and H/D [13]*

Finally, module C (see figure 3.28)is designed to be 47 mm length and it corresponds to a straight tube added to reach the minimum duct length of 145 mm, and it is positioned near the B module.

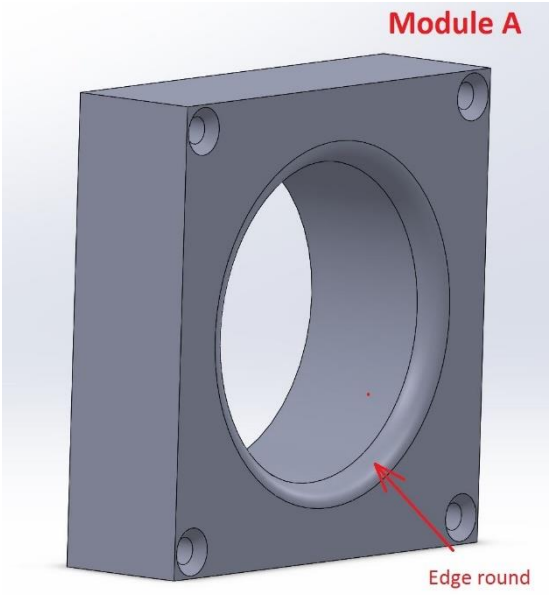

Figure 3.27 *Module A 3D design with rounded edge*

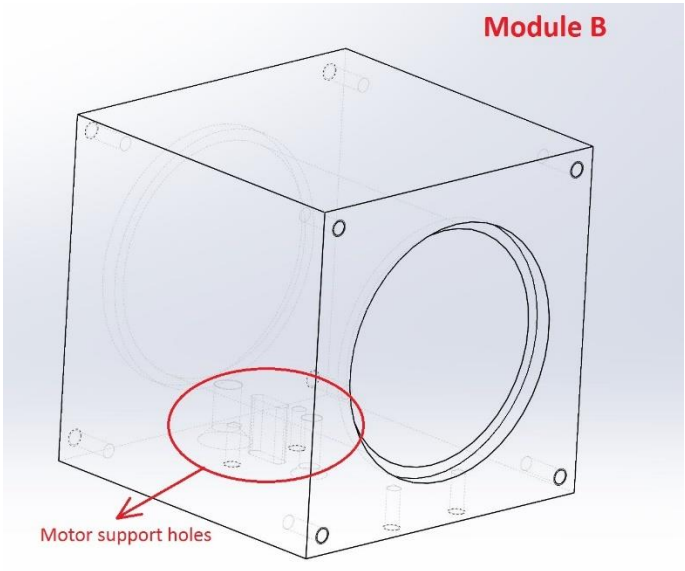

Figure 3.26 *Module B 3D design and details regarding the attacks of the motor support and the wind tunnel support*

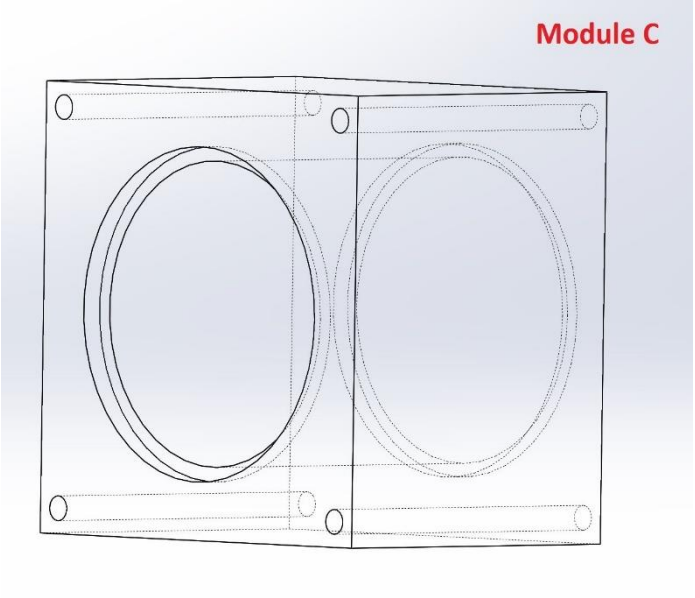

Figure 3.31 *Module C 3D design*

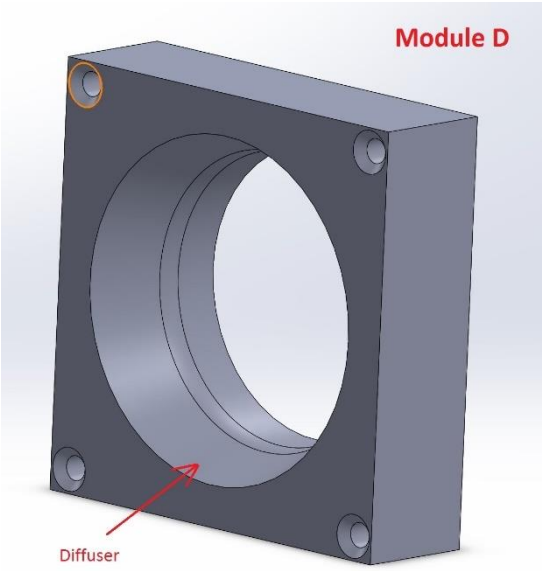

Figure 3.30 *Module D 3D design diffuser with L/D=0.3 and H/D=0.1*

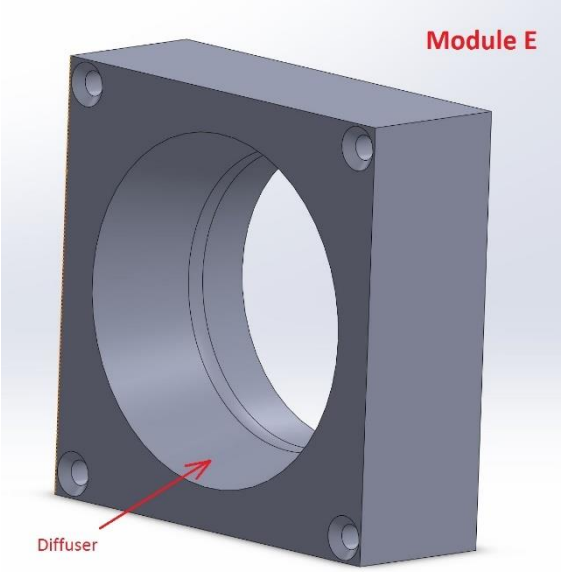

Figure 3.29 *Module E 3D design diffuser with L/D=0.4 and H/D=0.1*

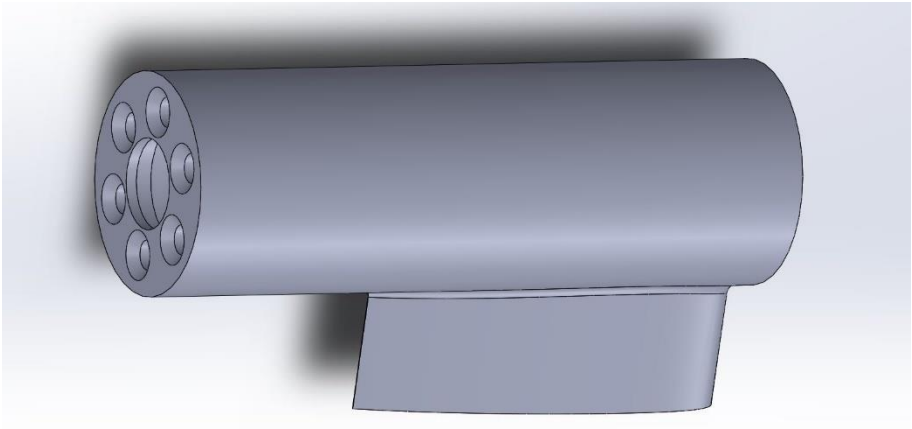

Figure 3.28 *Module support 3D design with the airfoil shape tower*

3.5 Construction

The turbines are produced using bronze casting technology with a tolerance at the order of micrometer. A modification is applied on the blade trailing edge because it must be rounded with respect the sketch in figure 3.2, otherwise the 3D printing machine is not able to produce pieces with sharp corners (see figure 3.32). The motor support is also produced using bronze with the same procedure.

Module B is fabricated in aluminum to increase the piece stiffness, since it must be connected to the wind tunnel support, and it sustains all the others modules including the motor support the generator and the turbine attached to the generator shaft. The others parts of the duct are fabricated in reinforced nylon additive using 3D printing technology.

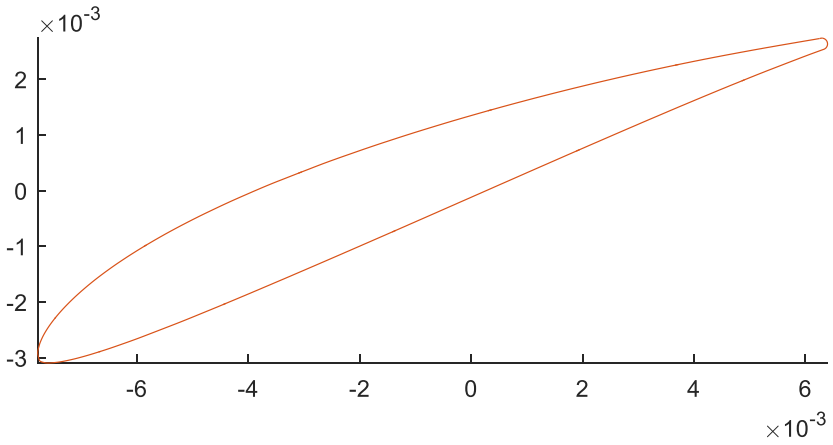

Figure 3.32 *4 cm Airfoil blade section with rounded trailing edge*

In figures 3.33-3.35 the turbines produced are presented.

Figure 3.35 *3 cm airfoil wind turbine*

Figure 3.34 *4 cm airfoil wind turbine*

Figure 3.33 *4 cm symmetric wind turbine*

4 Experimental tests

Experimental tests are performed with the designed turbines in order to analyze the performance in terms of power and power coefficient. In this section the experimental setups used for the identification and validation procedure, the facilities and tools used for testing purposes are described in details.

4.1 Experimental setup

The experimental tests are carried out in two configurations:

- open field tests;
- confined flow tests.

In the open field arrangements two operational condition are investigated:

- active control test (ACT);
- passive test (PT).

Tests were performed in open field on 4 cm and 3 cm airfoil turbines to estimate the performances and to compare them with those numerically evaluated by the BEM code. Furthermore, open field tests are achieved on 4 cm symmetric wind turbine to a performances comparison with airfoils turbines.
In addition the open field tests are accomplish using a prolongation shaft to favor the wake disposal, and with turbine directly attached to the motor shat.
In confined flow tests the symmetrical turbine is investigated, only in passive operational condition, in a duct with different duct arrangement (duct length, with/without diffuser,…) to identify the best configuration for the final application.
In the active control tests the motor rotates at a fixed angular speed. The power generated or absorbed by the motor correspond to the power introduced by the turbine, except for the bearing dissipations.
In passive tests the motor is directly connected to an electrical circuit with a resistive passive load. By changing the resistance, it is possible to modify the operating steady-speed.

4.1.1 "Sergio De Ponte" POLIMI wind tunnel

The wind tunnel is the environment aimed at reproducing the turbines behavior under study. The objective is achieved by reproducing different wind speeds in a proper facility, where the fluid characteristics are uniform and under control. All the tests are carried out in the "Sergio De Ponte" wind tunnel shows in figure 4.1 located in the aerospace engineer department (DIA). It presents a closed air circuit and a test chamber of size 1.5 x 1 m and length of 3 m. As seen in figure 4.1 airflow comes from a convergent located on the right side in blue, passes though the test chamber and goes to a divergent on the left part of the wind tunnel in blue. The wind velocity obtained is measured using a pitot tube. The main characteristics are reported in table 4.1.

a

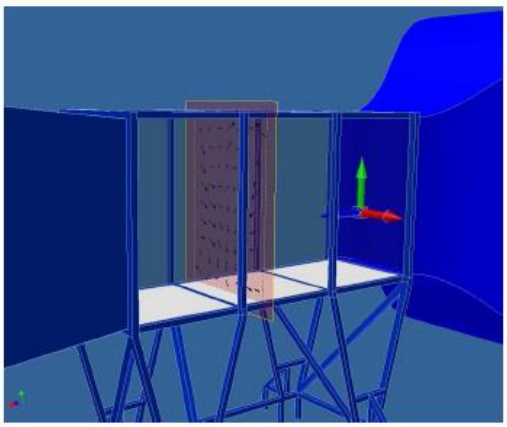

b

Figure 4.1 *CAD model a) and real picture b) of "Sergio De Ponte" at Politecnico of Milan (DIA)*

	"Sergio De Ponte" wind tunnel
Type	Closed-jet
Section width x height	1.5 x 1 m
Max wind speed [m/s]	55
Control	open-loop
Location	*Politecnico di Milano* *Dipartimento di Ingegneria Aerospaziale (DIA)*

Table 4.1 *Main characteristics of wind tunnel*

4.1.2 Active control tests

The active control tests are performed to evaluate the actual power introduced by the turbine. A block diagram of the ACT is sketched in figure 4.2.

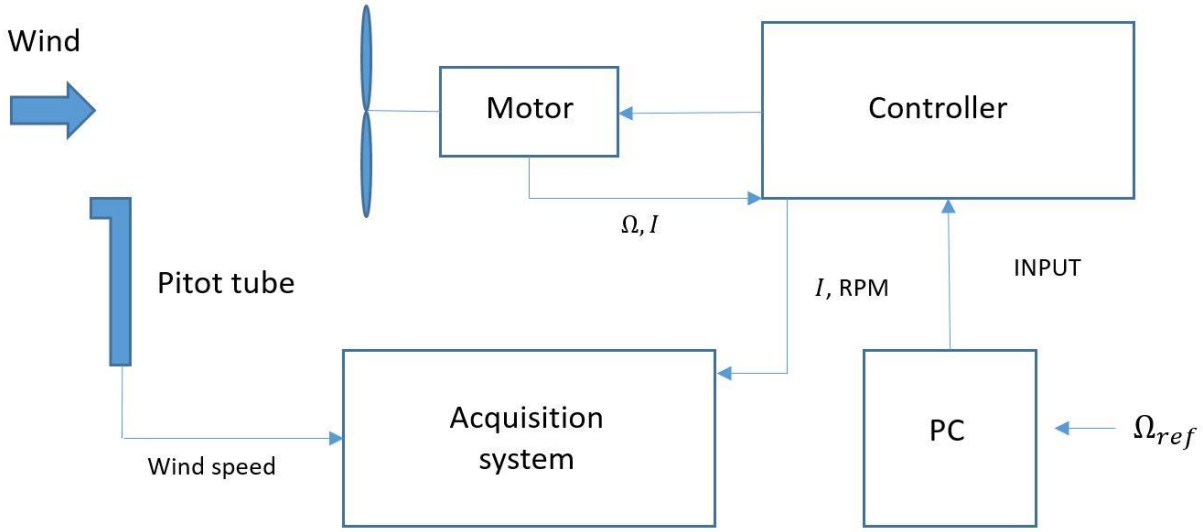

Figure 4.2 *Block diagram of the ACT configuration*

where Ω_{ref} represents the angular velocity of the motor given in input to the system by the user, Ω is the angular velocity of the motor shaft, I represents the motor current feedback.
The inputs of the acquisition system are the following:

- the current, I, feedback by the motor;
- the rpm derives from the angular velocity of the motor shaft, Ω;
- the wind speed measured by the pitot tube.

In the ACT the controller gives an input to the motor in order to maintained the selected reference speed, therefore the current sign derived in the acquisition system is negative, opposition to the sign for generation purpose.
The motor used is 16ECP36 – 8B Ultra EC^{TM} Portescape three phase brushless motor which main characteristics are summarized in table 4.2.

	Portescape motor
Power	23 W
Nominal voltage	24 V
No-load speed	12420 rpm
Max rotor speed	63000 rpm

Table 4.2 *Portescape brushless motor characteristics*

The maximum motor velocity was imposed to 16000 rpm because, in the present study, the working voltage range was 4-18 V, correspondent to the working range of the monitoring system in the final application. Furthermore, it is equipped with a digital encoder, hence, it is possible to know the velocity, Ω, of the shaft that is feedback to the controller, see figure 4.2.

The controller block is composed by Maxon motor control which gives in input to the motor a tension proportional to the reference velocity in order to maintain the rotational velocity as stable as possible. A sketch of the control block diagram implemented is in figure 4.3.

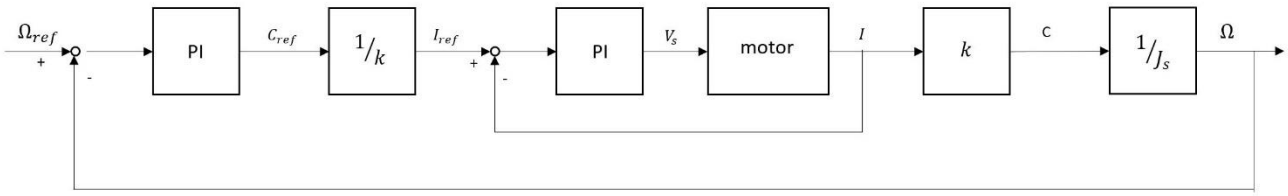

Figure 4.3 *Control block diagram*

There are two proportional-integral (PI) controllers, one able to control the velocity and one the tension in input to the motor.

First of all, the user gives in input a reference velocity, Ω_{ref}, that is compared with the one coming from the motor, Ω. The inertia of the motor shaft, J_s, is known therefpre from the eq. 4.1 is possible to calculate the reference torque, C_{ref}, passing through a proportional and integral control.

$$C_{ref} = k_p(1 + \frac{k_i}{k_p})J_s\,\Omega_{ref} \qquad (4.1)$$

where k_p and k_i represents the proportional and integral gain. Then the reference current is derive using eq. 4.2:

$$I_{ref} = \frac{C_{ref}}{k} \qquad (4.2)$$

in which k correspond to the motor constant. An internal current loop is also present with PI controller where the current derived by the motor is compared with the reference one. Afterwards, using equation 4.2 with actual current value, I, it is possible to evaluate the effective torque. Therefore using eq. 4.3:

$$\Omega = \frac{I_s}{C} \tag{4.3}$$

it possible to calculate the actual angular velocity of the motor that needs to be compared with the reference. This procedure is accomplish every time the angular reference velocity is changed in order have the actual velocity, Ω, as similar as possible with the reference.

4.1.3 Passive tests

Passive tests are performed in order to evaluate the actual power available at the circuit accounting for all the mechanical and electrical efficiencies. In figure 4.4 is presented the passive block diagram.

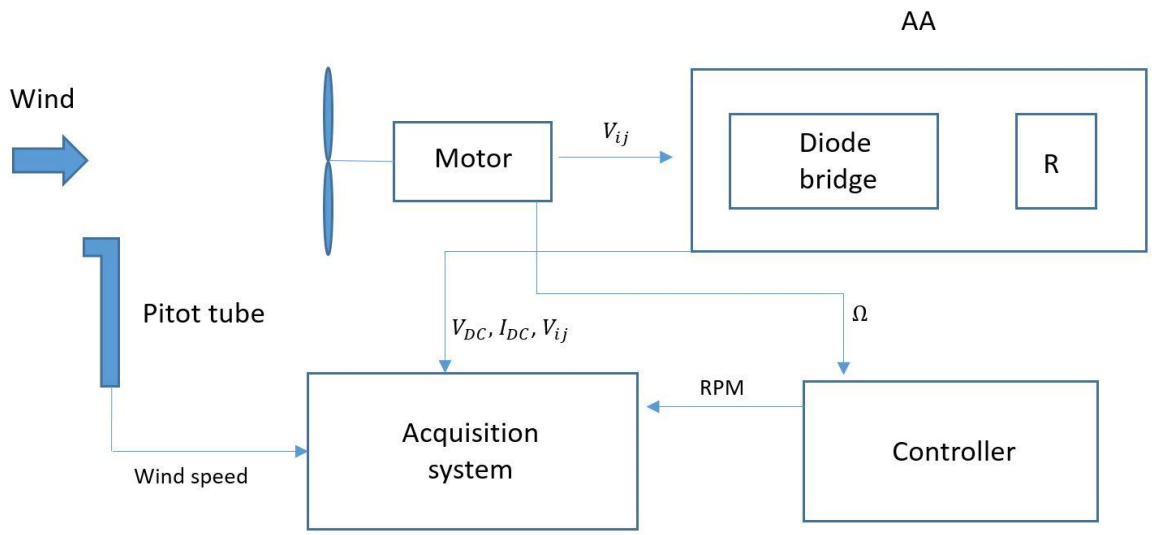

Figure 4.4 *Block diagram of the PT configuration*

Also in this case the controller participates on the analysis and it has only the objective to provide the angular velocity to the acquisition system. The motor used in passive configuration is the same of ACT arrangement.

The principal block is the "AA", sketched in figure 4.5, composed by:

- three phase diode bridge rectifier;
- resistive loads.

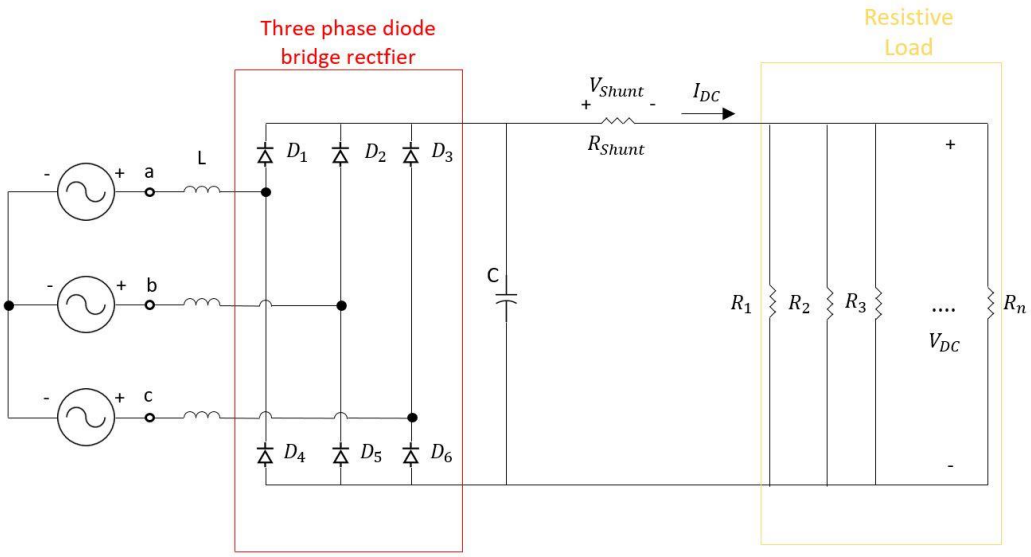

Figure 4.5 *Block AA representation*

In figure 4.5, L represents the motor induction, D_i corresponds to the diodes, C is a condenser; R_{Shunt} is called "Shunt" resistance and it is equal to 0.5 Ω and R_n represents each resistive load.
The motor gives in output three voltage, V_a, V_b and V_c represented by sinusoidal signals 120° out-of-phase. The aim of the rectifier is to transform the out-of-phase signal in a single continuous one. After the diode bridge the outcoming signal passes through a condenser, C, that contributes to reduce the signal disturbance. Then, after the diode bridge the resistive load is present and it is composed by different types of resistances, organized in three rank of ten resistances each, with the aim of simulate the real load. Three type of resistance are adopted:

- 3300 Ω;
- 1500 Ω;
- 220 Ω.

Those are organized in parallel and, in order to generate the points to built the performance curve, are composed in different combinations.
What the block AA gives in output are:

- the voltge V_{DC};
- the current I_{DC};
- one of the cross-phase of the motor output V_{ij}.

The first is measure across the resistive load applied on the system, while the current is obtained by using a known resistance, R_{Shunt}, called "Shunt resistance" equal to 0.5 Ω, and measuring the tension, V_{Shunt}, across it. Then the current can be derive using the Ohm's law, equation 4.4.

$$I_{DC} = \frac{V_{Shunt}}{R_{Shunt}} \tag{4.4}$$

Therefore, in PT, the acquisition system receives in input the current I_{DC}, the voltage across the resistive load V_{DC}, the angular velocity coming from the controller, the wind speed from the pitot tube and V_{ij} that represents one of the three voltages ($V_{ab}, V_{ac}\ or\ V_{bc}$) across the motor terminals.

4.1.4 Turbine supports

Because the turbine needs to stay at the center of the wind tunnel, a support is used to maintain the motor and the turbine lifted from the floor, hence, the undisturbed airflow, incident the turbine blades, does not be affected by the wind tunnel walls.

The experimental campaign is accomplished using two motor and turbine supports: S_1 and S_2. The first, S_1, sketch in figure 4.9.

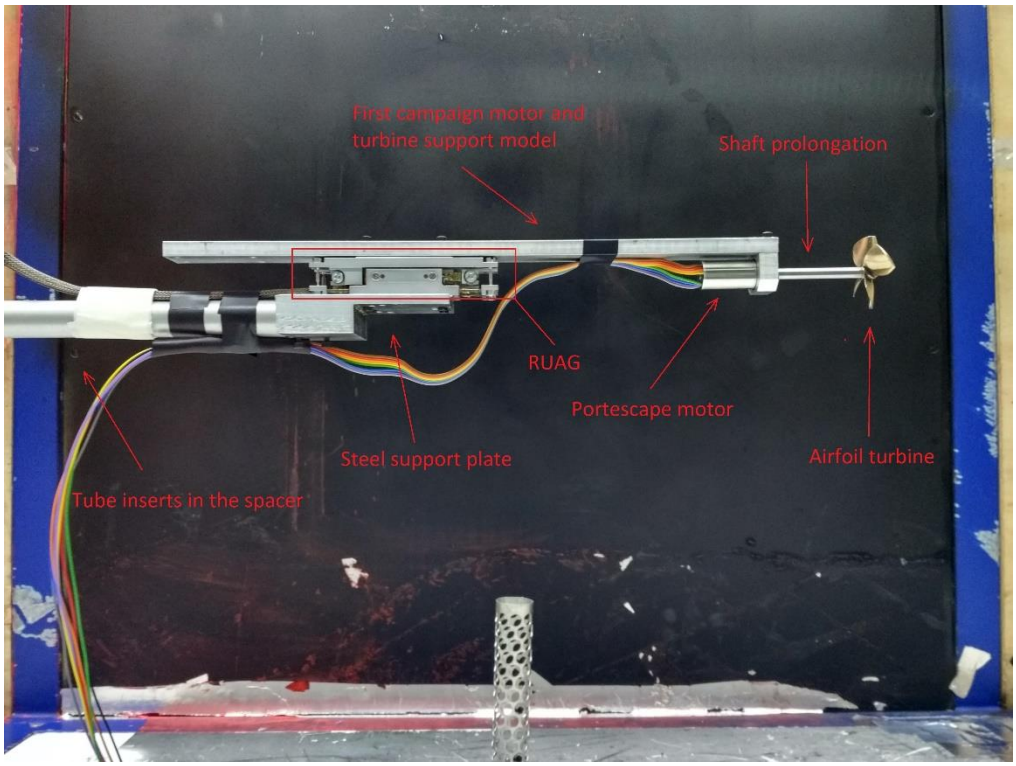

Figure 4.6 *Turbine and motor support S_1*

The second support, S_2, is design specifically for the confined flow application, therefore it has a shape that enhance the performance with respect the S_1 support even if the turbine is mounted directly on the motor shaft. It is composed by the tower with an airfoil shape to favor the passage of the air especially in the duct application. Furthermore, the block behind the turbine has reduced dimension, based on the motor, in order to have less influence on the wake disposal.

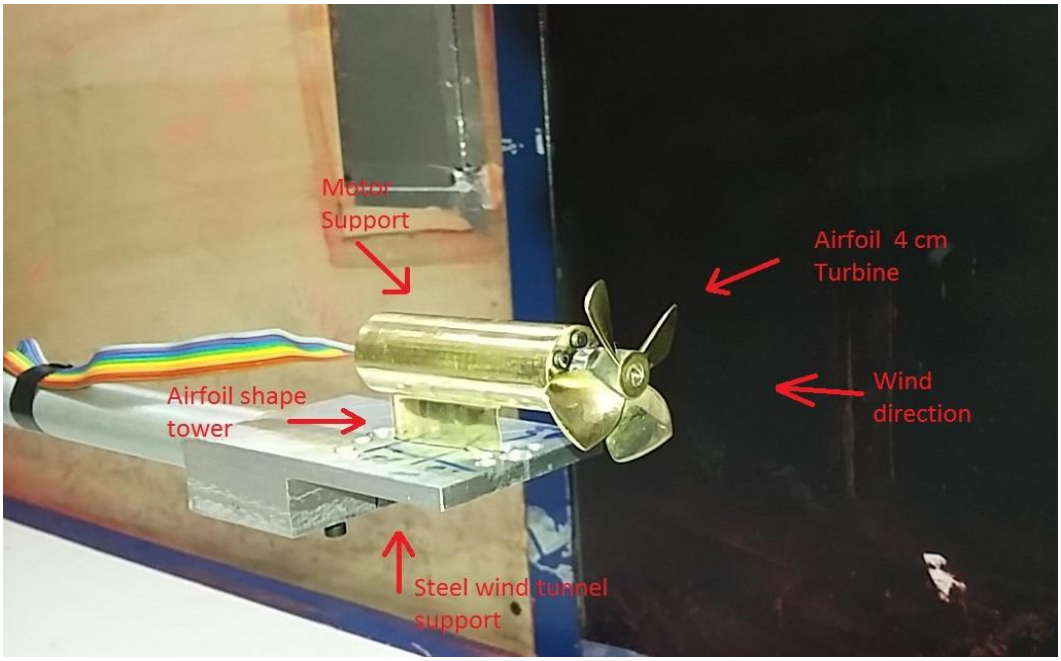

Figure 4.7 *Turbine and motor support S_2*

4.2 Open field tests results

4.2.1 Active tests

The open field configuration is adopted as reference configuration because the airflow incident the turbine's blades is not subjected to any structural influence that can cause (i) viscous losses, and (ii) turbulent flow. Therefore the open field tests guarantee that the harvested energy derives completely from the undisturbed wind.

The goal of the active tests is to validate the BEM numerical model by means of a comparison in terms of power produced by the turbine and the corresponding power coefficient. The correspondent curves are recreated by means of discrete step given by the variation of the tip speed ratio at fixed wind velocity. The eq.(1.3) derives the motor velocity that is given in input to the control system. The advantage of the active

controlled tests regards the possibility to built the performance curve staring from the left side: starting from low rpm and going forward increasing the motor rotational velocity.

4.2.2 Preliminary tests

The data coming to the post process are comprehensive of motor losses. Therefore preliminary tests are done to predict the real aerodynamic torque through the equation 4.5:

$$C_{aero} = (I_{mot} - I_{diss})k \tag{4.5}$$

where k represents the motor constant, I_{diss} is the current dissipated in friction and motor element resistances while I_{mot} represent the current given to the system by the power supply. Hence two preliminary tests are done:

- evaluation of the motor constant k;
- evaluation of the bearing losses to find $\mathrm{I_{diss}}$.

In order to evaluate the motor constant k, a specific campaign of experimental tests is performed on the system schematize in figure 4.8, described by the equation (4.6):

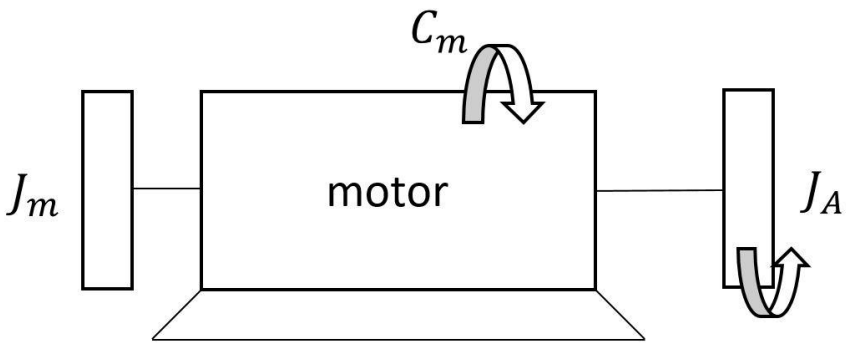

Figure 4.8 *Motor and inertial load schematization*

$$C_m - J_m\dot{\omega_m} - J_A\dot{\omega_m} = 0 \tag{4.6}$$

where J_m is motor inertia, J_A represents the inertia of the load, C_m corresponds to the motor torque while $\dot{\omega_m}$ is the motor velocity.

The estimation of the motor constant is achieved by the ratio between the maximum motor torque amplitude and maximum current amplitude (equation 4.7):

$$k = \frac{C_m}{I} \tag{4.7}$$

To estimate the motor torque, C_m, the inertia terms in eq. (4.6) are estimated. The motor inertia, $J_m = 0.06\ Kgmm^2$ is given in motor datasheet while, the inertia $J_A = 0.054\ Kgmm^2$ is estimated from an aluminum cylinder by CAD, figure 4.9.

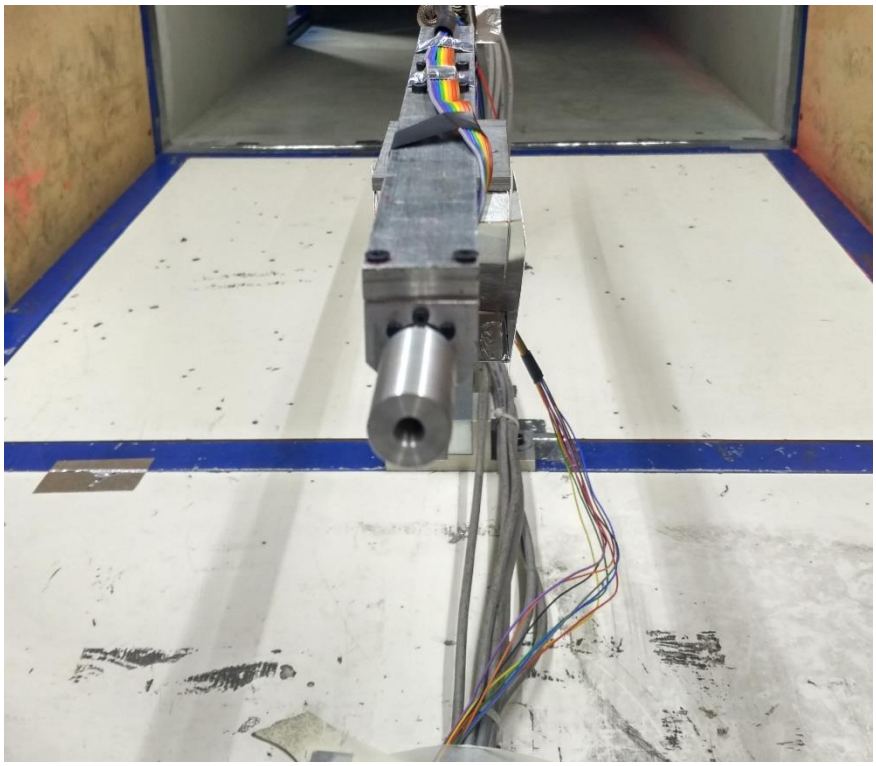

Figure 4.9 *Cylinder used for calculation of the motor constant*

The tests are performed in active configuration giving in input to the system a sinusoidal signal representing the motor angular velocity with constant mean value but variable amplitude at different frequencies. Then, the fourier transform of the signal is computed and the rpm and current module at the tested frequency are logged. Knowing the module of the angular motor velocity and the inertia of the system the actual motor torque can be computed using eq. (4.6) and finally the motor constant derived by means of eq. (4.5). In table 4.3 are presented the data and results used in the estimation of the motor constant.

RPM Mean value	Frequency	RPM amplitude	I amplitude	Torque amplitude	Motor constant $\mathbf{k}$
3000	1	472	0.0117	1.87 E-4	1.6 E-2
3000	1	946	0.0231	3.83 E-4	1.66 E-2
3000	1.5	434	0.0155	2.51 E-4	1.62 E-2
3000	1.5	867	0.0305	5.35 E-4	1.75 E-2
5500	1	452	0.0104	1.83 E-4	1.76 E-2
5500	0.5	485	0.00614	1.04 E-4	1.69 E-2

Table 4.3 *Data from the motor constant evaluation tests*

Therefore the final motor constant $\mathrm{k} = 0.0169$ is the mean value of those in table 4.3.

To evaluate the bearing losses, the system is positioned into the wind tunnel and the inertial mass attached on the motor shaft, J_A, is put in rotation by the motor in active control configuration, at different rotational velocities without any wind flow. The current necessary to maintain the motor at constant rotational speed, that has a positive sign because it is required by the system to preserve the rotation, represents the current needed to overcome the bearing losses, $\mathrm{I_{diss}}$. For each test the current is measured and the trend of $\mathrm{I_{diss}}$ as function of the RPM is represented in figure 4.10.

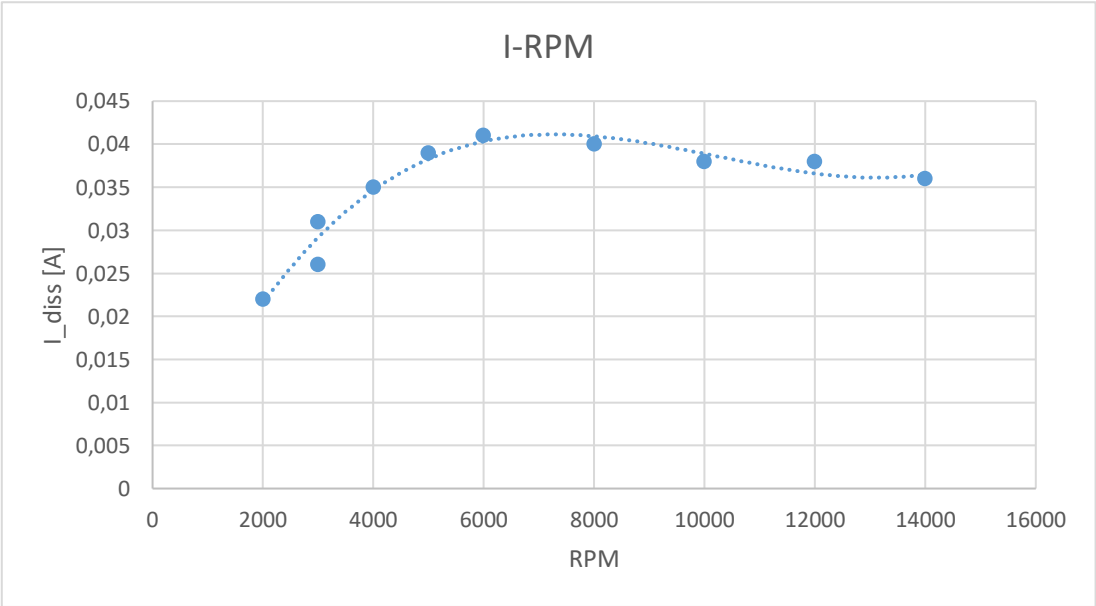

Figure 4.10 *Behavior of the current I_{diss} due the bearing losses as function of the RPM*

Interpolating the value of the current it is possible to obtain $\mathrm{I_{diss}}$ and making the difference with $\mathrm{I_{mot}}$ as known value coming from the acquisition system, $\mathrm{C_{aero}}$ can be calculated by means of equation 4.5.

4.2.3 Numerical model comparison

Both cm-scale turbines are tested in active configuration which means to impose to the controlled system the rotational speed of motor at fixed wind speed then, the acquisition system acquires data for each steady-state evaluation point. Those points are researched imposing the TSR variation at constant steps, therefore the rotational speed according to equation 1.3 increases until the motor rpm limit at the tested wind flow. Both airfoil turbines active tests are accomplished using a shaft prolongation of 50 mm length between the motor and the turbine to favor the wake disposal. After the current correction, due to the bearings losses previously described, it is possible to known the effective aerodynamic power generated.

In figure 4.11 and figure 4.13 are presented power coefficient and power without any current correction but considering all the motor friction losses. The same graphs with the applied current correction (figure 4.12 and figure 4.14) are shown and then the comparison between the numerical and the experimental results are represented in figure 4.15-4.16.

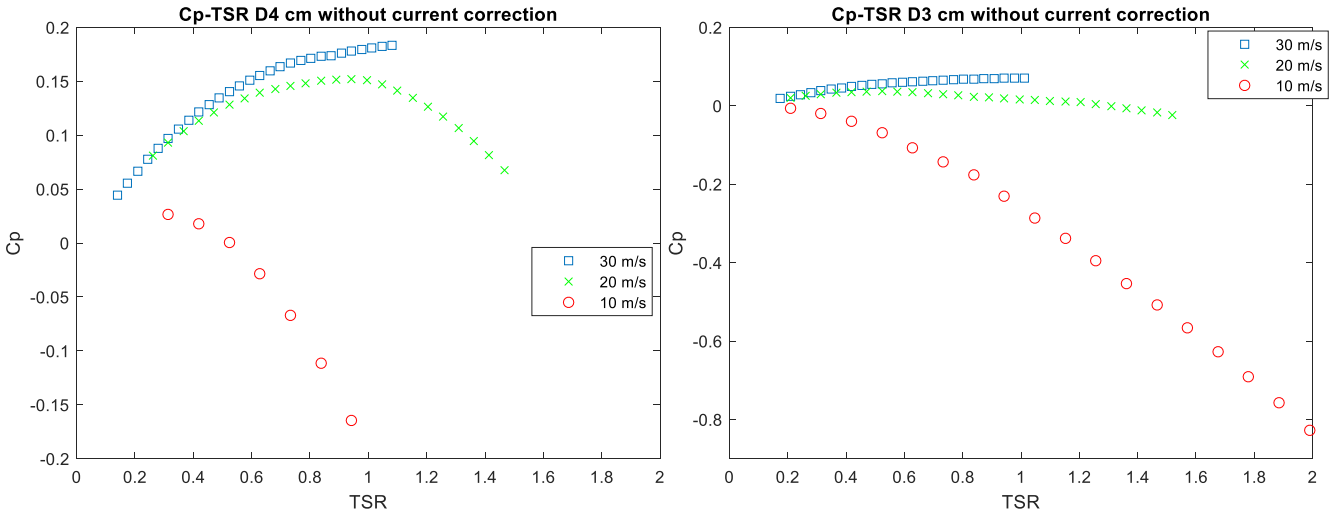

Figure 4.11 *Active control test: C_P vs TSR without current correction for 4 cm airfoil turbine (a) and 3 cm airfoil turbine (b)*

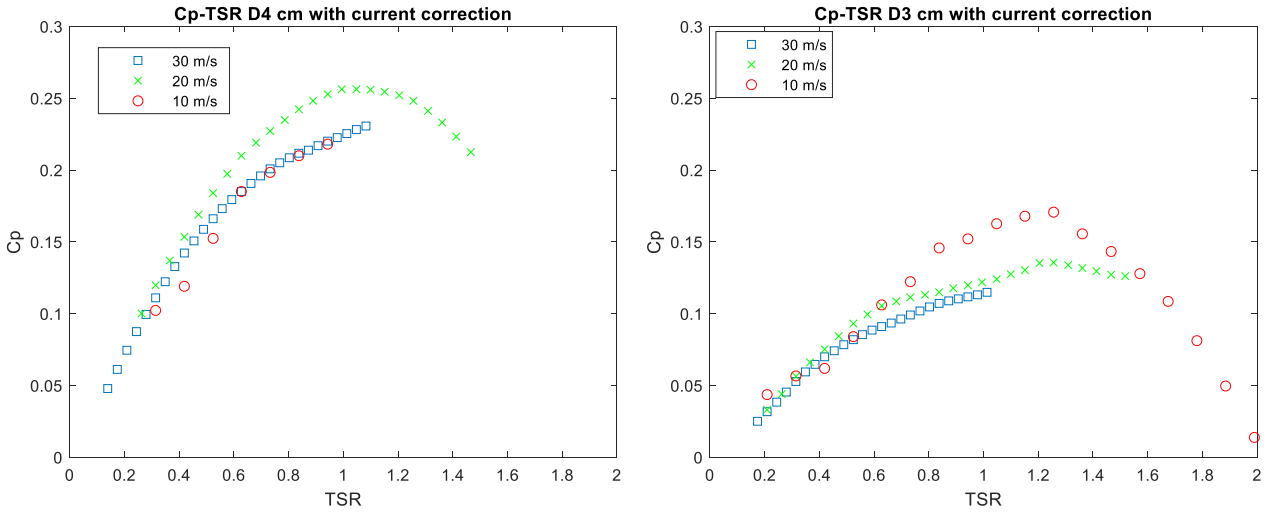

(a) (b)

Figure 4.12 *Active control test: C_P vs TSR with current correction for 4 cm airfoil turbine (a) and 3 cm airfoil turbine (b)*

The power coefficient is linked to the turbine's blade geometry therefore may not vary with air speed, while in case without correction in figure 4.11, this does not happen. Once the torque is purified from the bearing losses as in figure 4.12, the power coefficient seems to collapse on a single curve, at least, at low tip speed ratio. Furthermore the current correction is able to raise the curves to the pure aerodynamics value. It is important to notice that the efficiency of the 3 cm wind turbine is almost halve in comparison with the 4 cm turbine. In addition, the 3 cm-scale turbine seems to have a higher efficiency at 10 m/s wind speed. This happens because the current correction is higher with respect to the current value introduced by the aerodynamic torque, hence, the curve al low wind speed rise more.

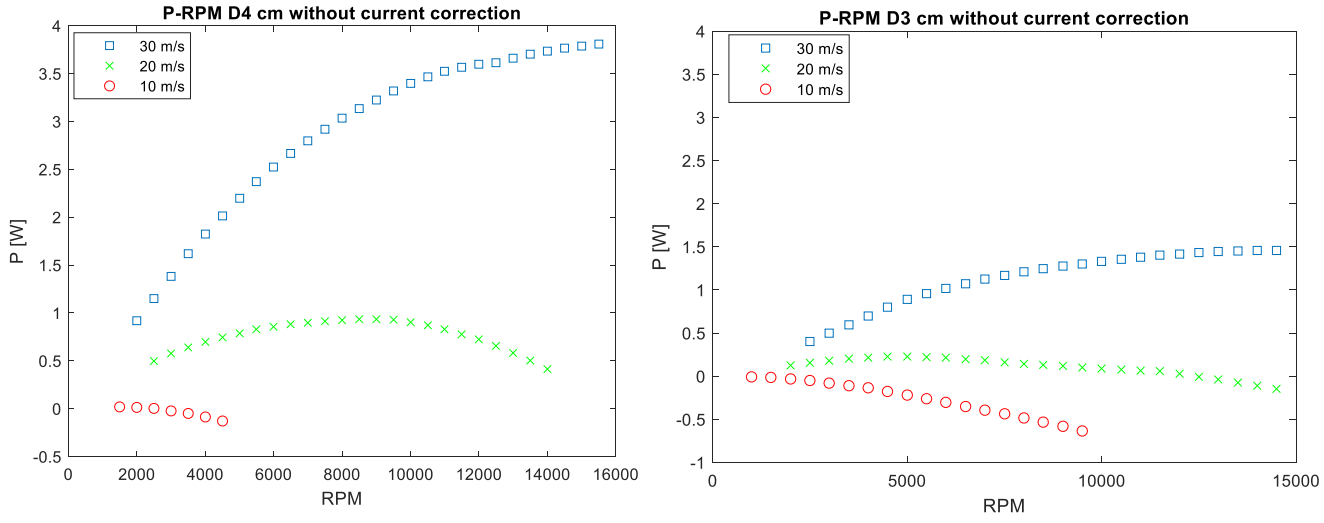

(a) (b)

Figure 4.13 *Active control test: P vs RPM without current for 4 cm airfoil turbine (a) and 3 cm airfoil turbine (b)*

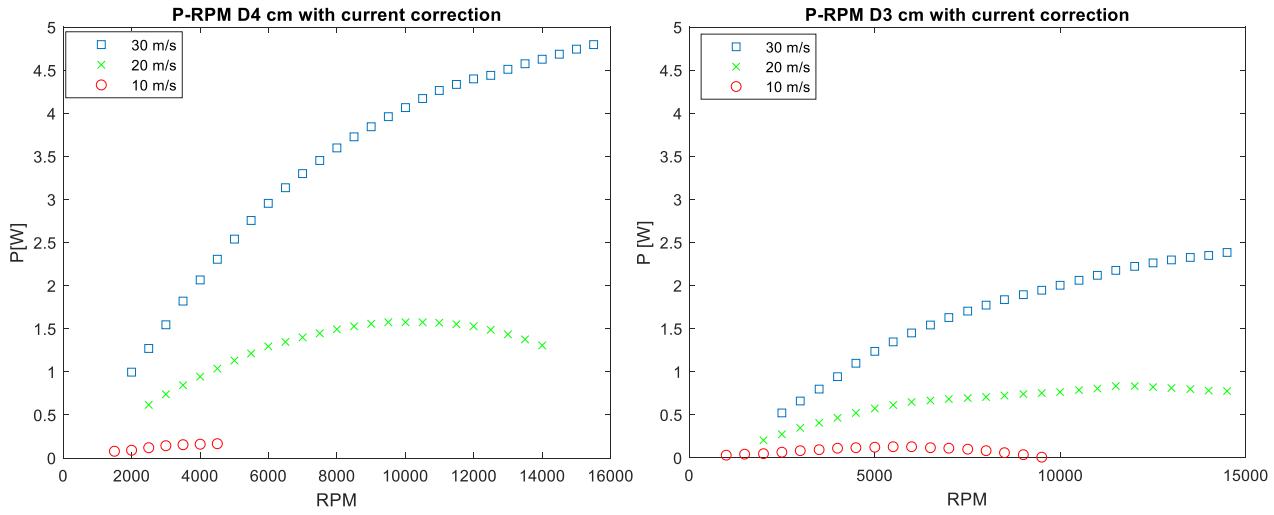

Figure 4.14 *Active control test: P vs RPM witht current correction for 4 cm airfoil turbine (a) and 3 cm airfoil turbine (b)*

The power produced by the 3 cm wind turbine is almost half the power generated by the 4 cm. This is more evident at 20 m/s and 30 m/s.

Table 4.2 summarizes the peak experimental values regarding power and power coefficient.

Wind speed [m/s]	**4 cm airfoil wind turbine**		**3 cm airfoil wind turbine**	
	P [W]	Cp	P [W]	Cp
10	0.17	0.22	0.13	0.30
20	1.58	0.26	0.83	0.24
30	4.79	0.23	2.4	0.20

Table 4.4 *Active control test: experimental peak values of power and power coefficient for different wind velocity*

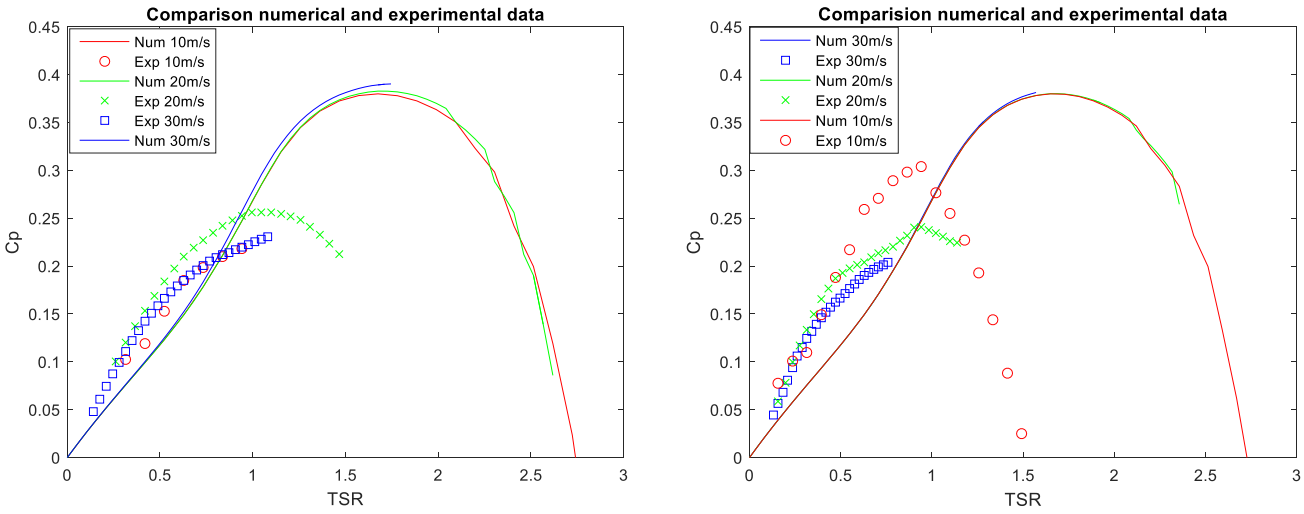

Figure 4.15 *Active control test: C_P vs TSR experimental and numerical comparison for 4 cm airfoil turbine (a) and 3 cm airfoil turbine (b)*

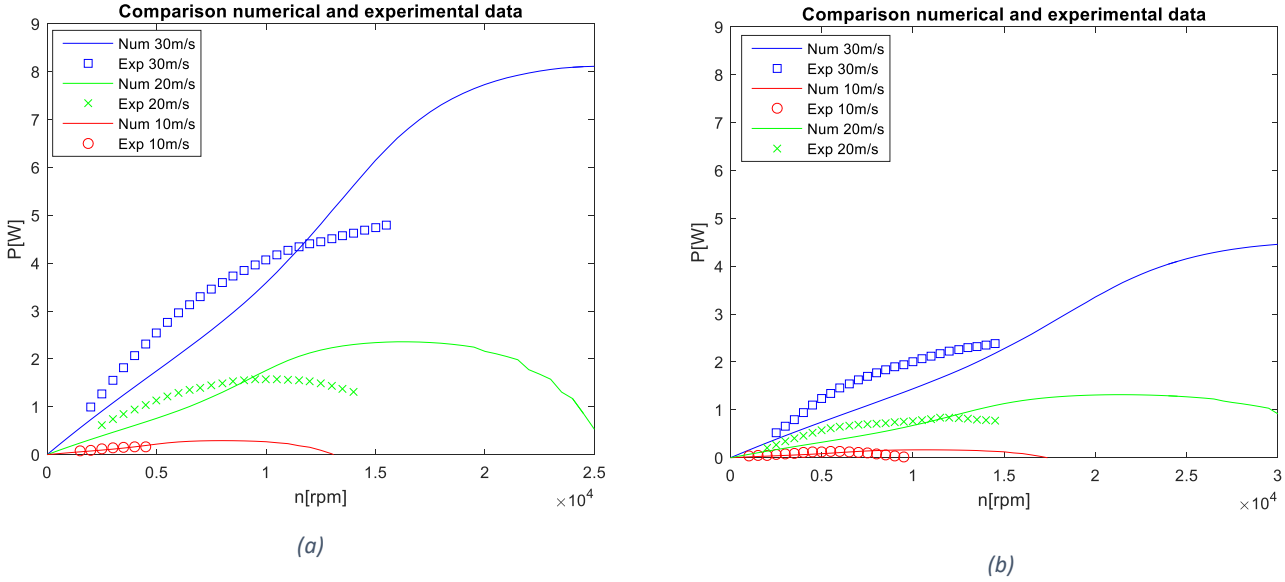

Figure 4.16 *Active control test: P vs RPM experimental and numerical comparison for 4 cm airfoil turbine (a) and 3 cm airfoil turbine (b)*

The experimental power coefficient of both turbines, see figure 4.15, has lower peak with respect the numerical result. Furthermore, the peaks derived from the numerical simulations seem to be shifted towards right while the experimental one corresponds to the TSR design point.

Regarding the power, only the 10 m/s experimental curve almost corresponds to the numerical one; the others experimental curves have a similar behavior with respect the numerical simulations, though, the

experimental curves tend to decrease more rapidly reaching a much less peak power than the numerical values.
Similar results of those in figure 4.15-4.16 were found in [3] where the agreement with the BEM code results was discrete in the increasing portion of the curve but the experimental maximum C_P value was lower and anticipated with respect to the numerical prevision

4.2.4 Passive tests

The passive tests are carried out because they represent the actual working condition of the turbine in its final application. "Passive" means that the electrical arrangements in which the motor has only generator function, therefore the centimeter turbine recovers wind energy in order to produce electricity and it happens only when the wind speed is high enough to win the internal motor/generator friction resistances. It is important to underline that in the passive tests the effective measured power is the one available downstream the rectifier, different from the one purely aerodynamic of the active tests, but purify by the mechanical and electrical losses.
Once the turbine rotates, the generator, without any resistive load, reaches its maximum rotational velocity at the given wind speed. Then resistances are applied to the system in order to reproduce different operating conditions. The loads are represented by three types of resistances: (i) 3300 Ω, (ii) 1500 Ω and (iii) 220 Ω.
Every acquisition is done only when the system reaches the steady-state value of current, rpm and voltage after the addition of a resistance. Each acquired point is dependent on the applied load, this means that it is possible to built performance curves point by point thanks to combination of different loads. Knowing the resistance load and the voltage it is possible to calculate the electric power extracted after the conditioning electrical circuit (accounting for the electrical losses), as in equation (4.3):

$$P = \frac{{V_{DC}}^2}{R_{eq}} \tag{4.5}$$

where V_{DC} is the voltage derived, in figure 4.5, and $\mathrm{R_{eq}}$ is the equivalent parallel resistive load calculated as the reciprocal of the sum of the reciprocal of each resistance as in equation 4.4:

$$R_{eq} = \frac{1}{\frac{n_1}{R_1}+\frac{n_2}{R_2}+\frac{n_3}{R_3}} \tag{4.6}$$

where R_1, R_2, and R_3 represent the applied resistances while n_1, n_2, and n_3 correspond to the number of each applied resistance. Because of the parallel arrangement of the resistances, the addition of load means to reduce the equivalent resistance, therefore the power generated increases. Furthermore, because the

motor is feed by a current proportional to the nominal velocity, increasing the load the rotational speed reduces while the tension, as compensation of the rise of the current, raises. Then the power generated passes through the resistances that dissipates it as heat. The curves are obtained starting from the operating condition reached by the turbine without resistive load (that corresponds to the maximum rotational velocity) and then adding one by one resistive load and reducing, consequently, the operating rotating speed. The passive configuration is deeply investigated in various open field configurations. These arrangements are indicated using a compact notation as:

$$D_i AS_j LU$$

where the letter D indicate the diameter and the subscription i indicates the diameter size (4cm or 3 cm); the second letter corresponds to the shape of the blade, A= airfoil and S=symmetric; third letter represents the support used in the actual configuration and the pedix j indicates which one of those previously described is adopted. The fourth letter indicates if a shaft prolongation is used, L, or if the turbine is directly attached to moto shaft,S. Finally the last letter corresponds to the position of the turbine with respect the wind direction: upwind, U, while downwind, D. In table 4.5 the tested configurations are summarized specifying the type of the turbine tested, the support (type 1 in figure 4.6, type 2 in figure 4.7), and the shaft length, if the test is done with the extended shaft or directly attached to the motor shaft.

Configurations	Turbine	Support	Shaft length
D_3AS_1LU	3 cm Airfoil	Type 1	50 mm
D_4AS_1LU	4 cm airfoil	Type 1	50 mm
D_4SS_1LU	4 cm Symmetric	Type 1	50 mm
D_4AS_2SU	4 cm Airfoil	Type 2	6 mm
D_4SS_2SU	4 cm Symmetric	Type 2	6 mm
D_4SS_1SD	4 cm Symmetric	Type 1	6 mm
D_4SS_1SU	4 cm Symmetric	Type 1	6 mm

Table 4.5 *Passive tests: table represents various tested configurations*

In configuration 1, 2 and 3 of the table 4.5 the prolongation shaft is used to favor the wake disposal and in order to be as similar as possible to the ideal machine conditions, in order to compare the performances of the three cm-scale turbines.

Furthermore, because the final application requires a compact system and because shaft requires bearings that cannot be placed in a duct due to space problem, the airfoil 4 cm turbine is directly attached to the motor shaft in configuration D_4AS_2SU in table 4.5. It is tested with the motor support type 2, in order to

compare its performances with the 4 cm symmetric turbine in the same conditions, as in configuration D_4SS_2SU. Finally tests with the symmetric turbine attached to the motor shaft are performed, because of the two ways wind directions, in configurations D_4SS_1SD and D_4SS_1SU, in order to evaluate the influence of the wind direction on the performances of a symmetric turbine.

4.2.5 Experimental results and comparisons

The first comparison is about the performance of the two airfoils and symmetric blades turbines in order to understand how much power is lost scaling the dimensions of the airfoil turbine and adopting a non-airfoil blade turbine, see figure 4.23. All tests done in figure 4.23, are computed using the support model S_1 and regards the configurations D_3AS_1LU, D_4AS_1LU and D_4SS_1LU.

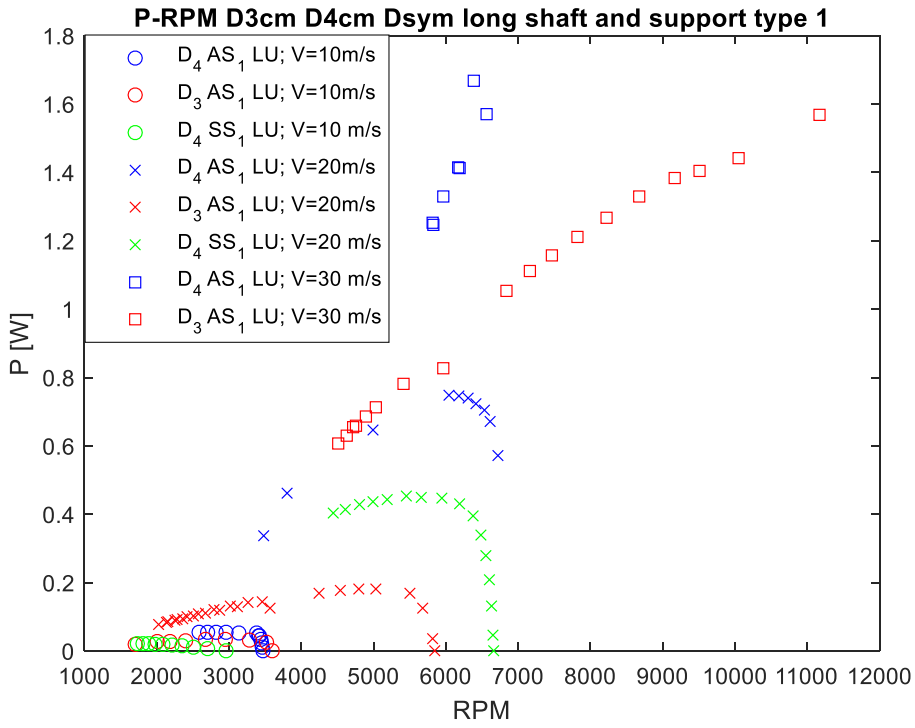

Figure 4.17 *Passive tests: Comparison of 3cm airfoil (D_3AS_1LU), 4cm airfoil (D_4AS_1LU) and 4 cm symmetric (D_4SS_1LU) wind turbines*

The table 4.3 resumes the maximum power [W] value for each wind velocity for tested prototypes in figure 4.17.

	4 cm airfoil		3 cm airfoil		symmetric	
Wind Speed	**P [W]**	**RPM**	**P [W]**	**RPM**	**P[W]**	**RPM**
10 m/s	0.05	2824	0.03	2947	0.021	1728
20 m/s	0.75	6179	0.18	5036	0.45	5944
30 m/s	1.66	6385	1.56	11170	-	-

Table 4.6 *Indication of maximum power performance at different wind velocity of cm-scale wind turbines*

As shown in figure 4.23, the 4 cm airfoil blade turbine is the one that generates more power, therefore it can be taken as reference and compare its performances with the others turbines. Considering both the airfoil turbines, the 3 cm presents a reduction of power production of 40% at 10 m/s wind speed. The gap increases at 20 m/s until 76% of generated power reduction. The symmetric turbine at 10 m/s presents a power reduction equal to 58% with respect the 4 cm airfoil, but at 20 m/s the symmetric turbine increase the power production, hence reducing the percentage of power decrease until 40%. Therefore, at wind speed of 20 m/s the power produced by the symmetric turbine is 60% higher than the 3 cm airfoil turbine, while at 10 m/s the generated power by the symmetric turbine is 30% less than the 3 cm airfoil. A comparison at 30 m/s wind speed of the three turbines is not possible because the 4 cm turbine shaft presents instability due to bending around 7000 rpm; the same problem appears on the symmetric blade earlier, reason why no points are available at 30 m/s. The only one that is stable at the higher wind flow is the 3 cm airfoil turbine.

After these considerations on power production, in the following tests the 3 cm turbine will be not considered anymore but the campaign focuses the attention on the 4 cm turbines, airfoil and symmetric blade.

Therefore, symmetric blades turbine is tested, as shown in figure 4.18, without the additional shaft to evaluate the penalties as a consequence of direct motor shaft-turbine connection that not guarantee a good wake disposal. Also in this case the support used is the type 1 (S_1) and the configurations tested are D_4SS_1LU and D_4SS_1SU.

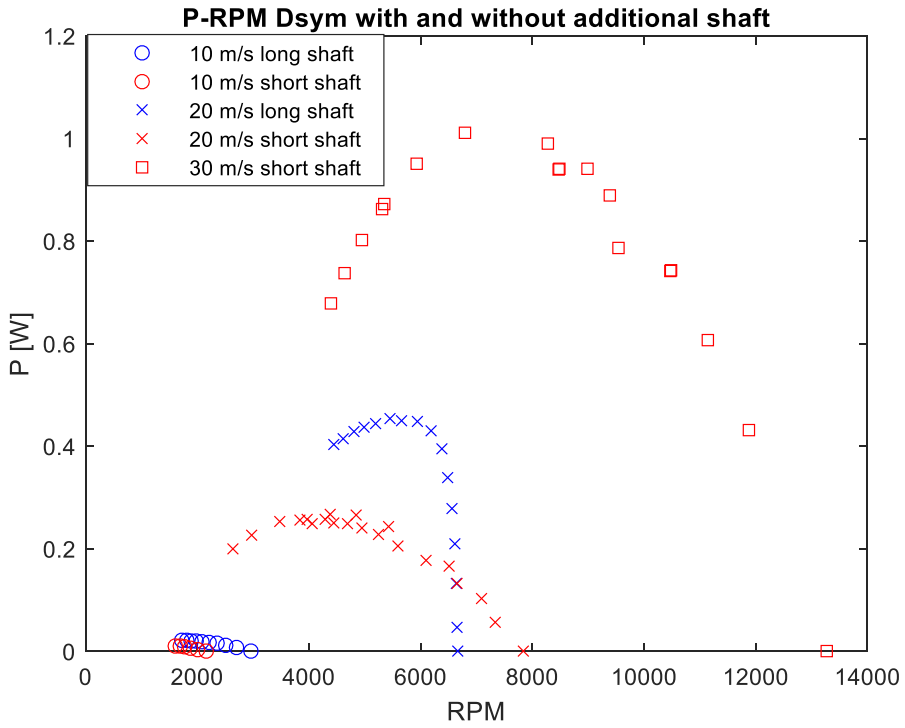

Figure 4.18 *Passive tests: Comparison of symmetric turbine with short shaft (D_4SS_1SU) and symmetric turbine with long shaft (D_4SS_1LU)*

Table 4.4 summarized the peak power production of both symmetric turbine configurations.

	Long shaft		Short shaft	
Wind Speed	**P [W]**	**RPM**	**P [W]**	**RPM**
10 m/s	0.02	1728	0.01	1606
20 m/s	0.45	5451	0.26	4375
30 m/s	-	-	1.01	6794

Table 4.7 *Maximum power performance regarding symmetric turbine with the long and short shaft*

As expected, the turbine attached to the motor shaft generates less power than the one with the extended shaft. The turbine with short shaft presents a power reduction of about 50% at 10 m/s. Furthermore, at 20 m/s wind speed the gap of the generated power decrease and it is around 42.2%. Hence, in percentage at higher wind speed the power reduction is less.

Because of the long shaft instability at high wind speed a comparison cannot be possible. The great advantage of the turbine with short shaft is the higher stability at elevated wind speed, hence, the turbine is able to reach 30 m/s wind velocity and high rotational speed presenting a maximum power production of about 1W.

Because the symmetric blades turbine needs to operate also in downwind situation, tests are computed to quantify the amount of power lost with respect the upwind arrangement. Hence, a comparison between the configuration upwind and downwind in short shaft arrangement with the type 1 support model (D_4SS_1SU and D_4SS_1SD respectively), is given in figure 4.19.

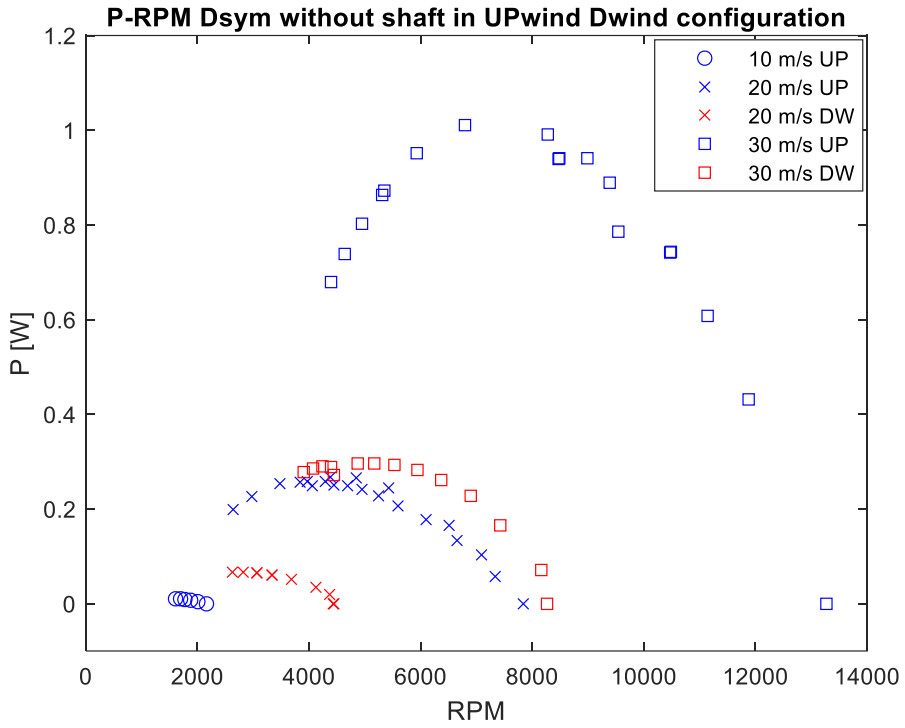

Figure 4.19 *Passive tests: Comparison symmetric blades turbine in upwind (D_4SS_1SU) and downwind arrangement (D_4SS_1SD)*

Table 4.8 summed up the peak power performance of the upwind and downwind configurations of symmetric blade wind turbine.

	Down-wind		**Up-wind**	
Wind Speed	**P [W]**	**RPM**	**P [W]**	**RPM**
10 m/s	-	-	0.01	1606
20 m/s	0.07	2627	0.26	4375
30 m/s	0.30	5174	1.01	6794

Table 4.8 *Peak power comparison of downwind and up wind symmetric blades turbine configuration*

As expected, the downwind configuration produces less electrical energy than the case upwind. At 20 m/s wind speed the downwind arrangements, the power is reduced by 73% with respect the other in up wind configuration. While raising the wind velocity the until 30 m/s, the power reduction of the downwind

arrangements remains almost constant, around 70.3%. When the turbine is in downwind configuration, the starting wind speed is higher than 10 m/s.

Afterwards, a comparative analysis between the symmetric turbine configuration with support type 1 and type 2 is needed because the type 2 support was designed in order to optimize the turbine short shaft configuration. See figure 4.20 for comparison of arrangements D_4SS_1SU and D_4SS_2SU.

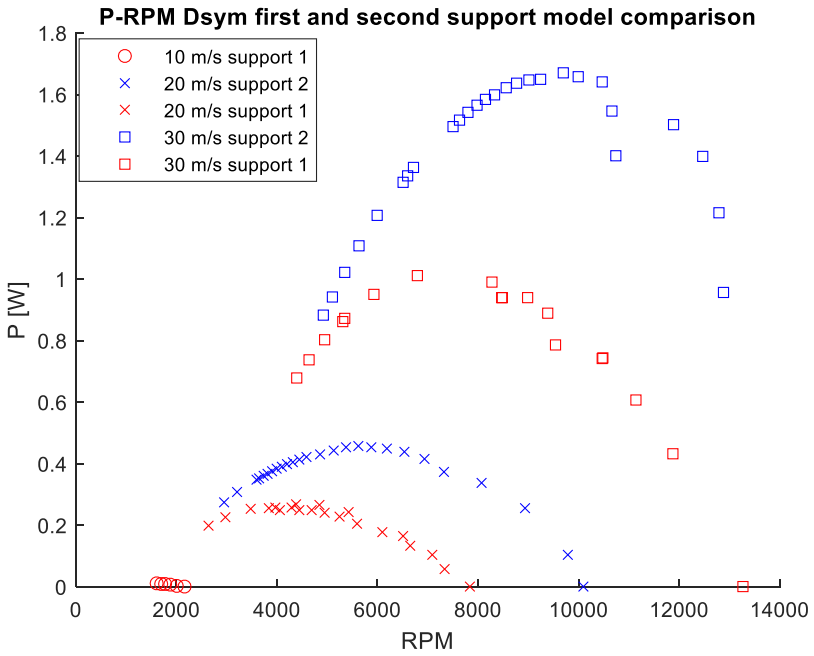

Figure 4.20 *Passive tests: Comparison symmetric blade turbine with support 1 (D_4SS_1SU) and support 2 (D_4SS_2SU)*

Table 4.6 summarized the different performance with the first and the second support model.

	Support 1		**Support 2**	
Wind Speed	**P [W]**	**RPM**	**P [W]**	**RPM**
10 m/s	0.01	1606	-	-
20 m/s	0.26	4375	0.46	5623
30 m/s	1.01	6794	1.67	9701

Table 4.9 *Peak power comparison of first support model and second support model*

Even if the second support model prevents the turbine rotation at 10 m/s, at higher wind velocity it increases the power generated by the symmetric blade turbine. In fact at 20 m/s the improvement given by the support 2 (S_2) compensates the elimination of long shaft because, as can be seen in table 4.9 and table 4.7, it is possible to obtain the same power production of the case D_4SS_1LU that has the shaft extension.

Considering the table 4.9, at 20 m/s the type 2 support increase the power generated by 43.5%, while at 30 m/s the support 2 enhances the power of about 39.5%, but in percentage is less with respect the same case at 20 m/s.

To verify the effect of the blade section (airfoil or symmetric) a new test is performed evaluating the 4 cm airfoil and the 4 cm symmetric wind turbine in order to understand how much energy is wasted adopting a non-optimized blade. Therefore, both turbines are tested in the same configuration (D_4AS_2SU and D_4SS_2SU respectively):

- upwind position;
- the turbines mounted directly on the motor shaft;
- support 2 (S_2) is used.

Performance results are available in figure 4.21.

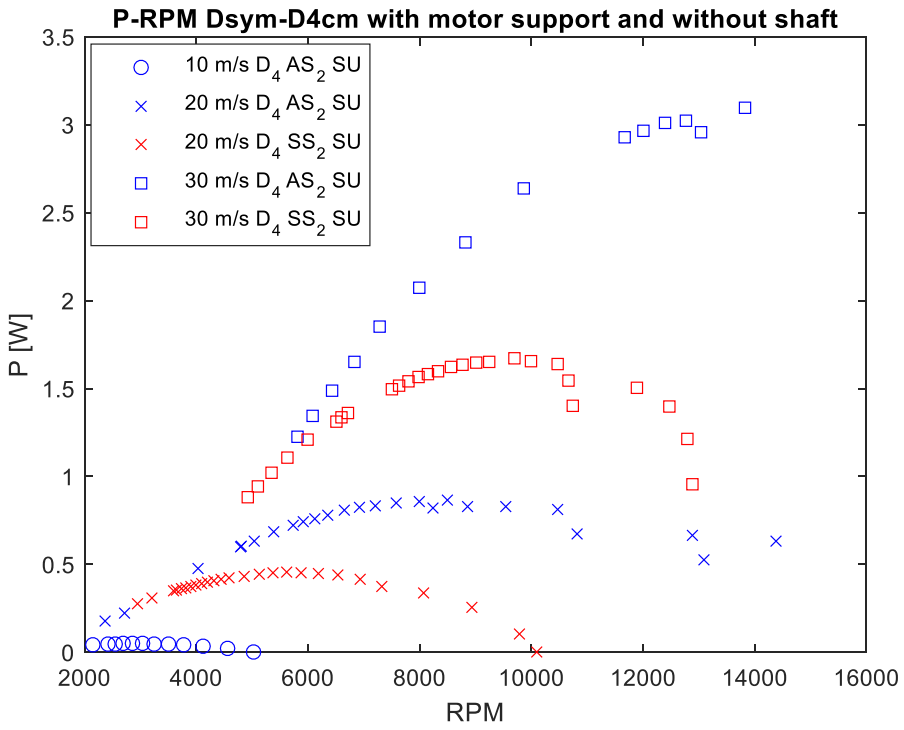

Figure 4.21 *Passive test: 4 cm airfoil wind turbine (D_4AS_2SU) and 4 cm symmetric blade wind turbine (D_4SS_2SU) comparison*

Table 4.10 summed up the peak power performance of the 4 cm airfoil wind turbine and the symmetric blade turbine.

	Airfoil		Symmetric	
Wind Speed	**P [W]**	**RPM**	**P [W]**	**RPM**
10 m/s	0.05	2552	-	-
20 m/s	0.86	8491	0.46	5623
30 m/s	3.09	13820	1.67	9701

Table 4.10 *Passive tests: Peak power performance of 4 cm airfoil turbine and symmetric turbine directly attached on motor shaft*

The symmetric turbine has power generation 46.5% less than the airfoil shape at 20 m/s and the reduction in percentage remains unchanged at 30m/s.
The airfoil turbine with support type 2 and short shaft, D_4AS_2SU, at 20 m/s, comparing table 4.10 and table 4.6, generates 12.8% more than 4 cm airfoil with support 1 and long shaft, D_4AS_1LU, while at 10 m/s the power produced is the same.

4.3 Confined flow tests

After the analysis of the open field tests in passive configuration to investigate the performance, in particular, of the 4 cm airfoil wind turbine and the symmetric blades turbine, in this paragraph the symmetric turbine is set within a duct and its performance are examined in both upwind and downwind configurations.
The need of these tests derives from the final application that requires a confined flow turbine for reasons related to compactness of the entire system and the preservation of the turbine.
The objective is the determination of the best duct layout in terms of power production, in particular the investigation is focused on.

- the presence of a divergent downstream;
- the presence of a convergent upstream;
- the position of the turbine inside the tube in upwind and downwind configuration;
- the duct length.

Different configurations are tested depending on the relative position of the modules described in chapter 3 with respect to module B. Therefore, the tested arrangements can be classified in “Long” and “Short” based on the number on module used. Each “Long” and “Short” has a subdivision due to the relative position of the modules. Furthermore, in order to switch from an upwind configuration to a downwind configuration using the same modules arrangement, the system is rotated around the axis perpendicular to the duct of B module.

4.3.1 Description of the tested duct configurations

The first four letters in the code name indicate the modules arrangement and the number of the letters correspond to the "Long" (4 letter) or "Short" (3 letter) configuration. The symbol T_i represents the turbine while the subscript indicates the module in which the turbine is located. Finally the last two letters reveal the wind direction, upwind (UP) or downwind (DW), and consequently the relative arrangement turbine/generator.

The table 4.11 summarized all the confined flow configurations tested.

Conf.	Code Name	Turbine Position	Wind Direction	Schematization
1	ACBD-T_DDW	Mod. D	Downwind	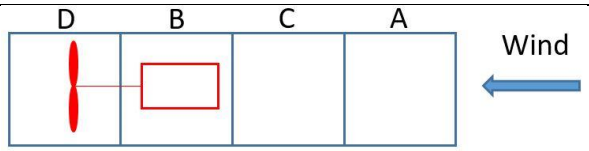
2	DBCA-T_DUP	Mod. D	Upwind	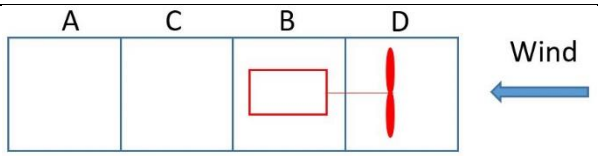
3	ECBD-T_DDW	Mod. D	Downwind	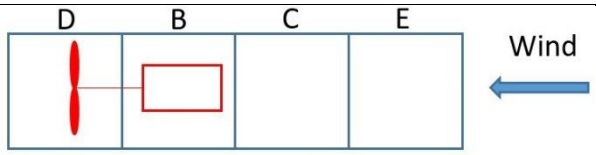
4	DBCE-T_DUP	Mod. D	Upwind	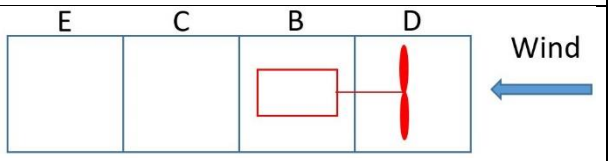
5	ACBE-T_EDW	Mod. E	Downwind	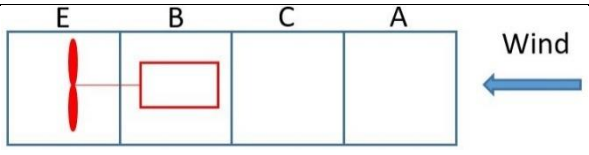
6	DCBE-T_CUP	Mod. C	Upwind	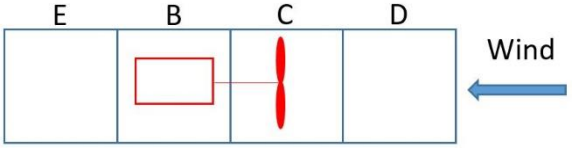
7	EBCD-T_CDW	Mod. C	Downwind	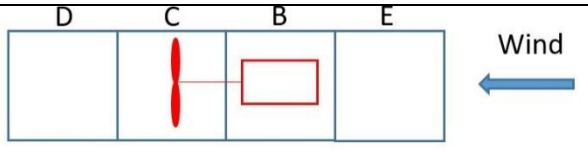

8	EBD-T_DDW	Mod. D	Downwind	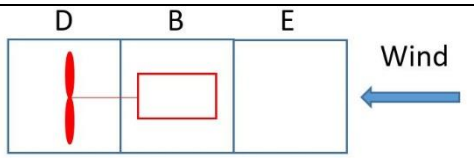
9	DBE-T_DUP	Mod. D	Upwind	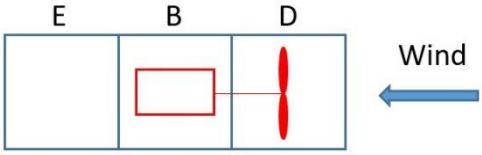

Table 4.11 *Summary of the confined flow configurations tested*

In the following the configurations are described:

1. ACBD-T_DDW (configuration 1): downwind turbine arrangements, see figure 4.22. The turbine is positioned in module D, divergent with $L/D = 0.3$. This is the first proposed duct design, it is characterized by a constant section inlet end a divergent section outlet.

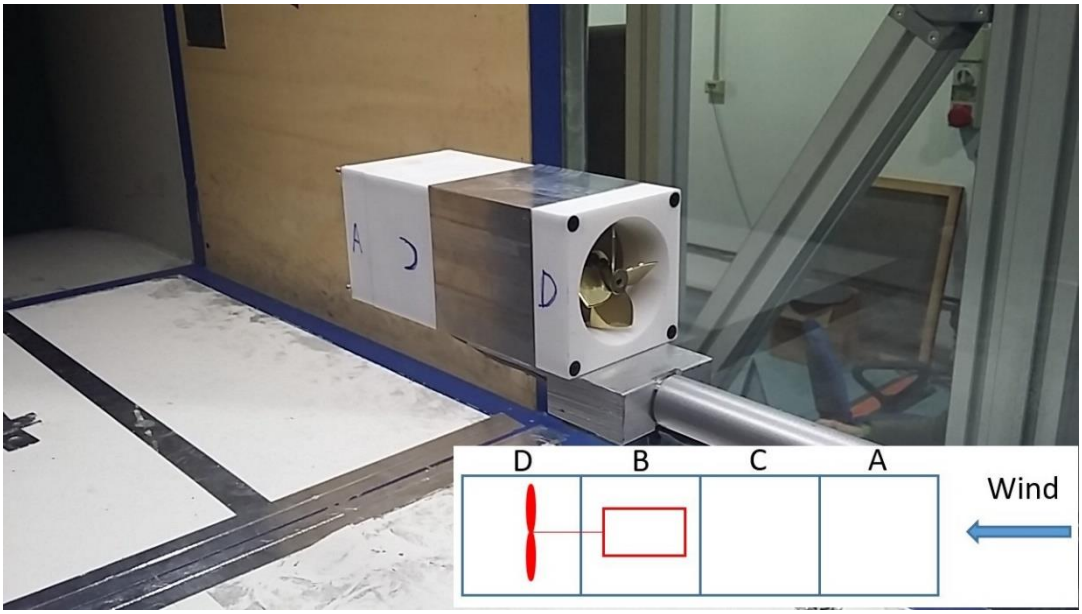

Figure 4.22 *Configuration 1-ACBD-T_DDW in downwind arrangement*

2 DBCA-T_DUP (configuration 2): the modules arrangement is the same of figure 4.22 but the all system is rotated of 180° to have the turbine in upwind configuration. The most important difference occurs in module D that has no more the simple frustum divergent function, but it behaves as a convergent (see figure 4.23).

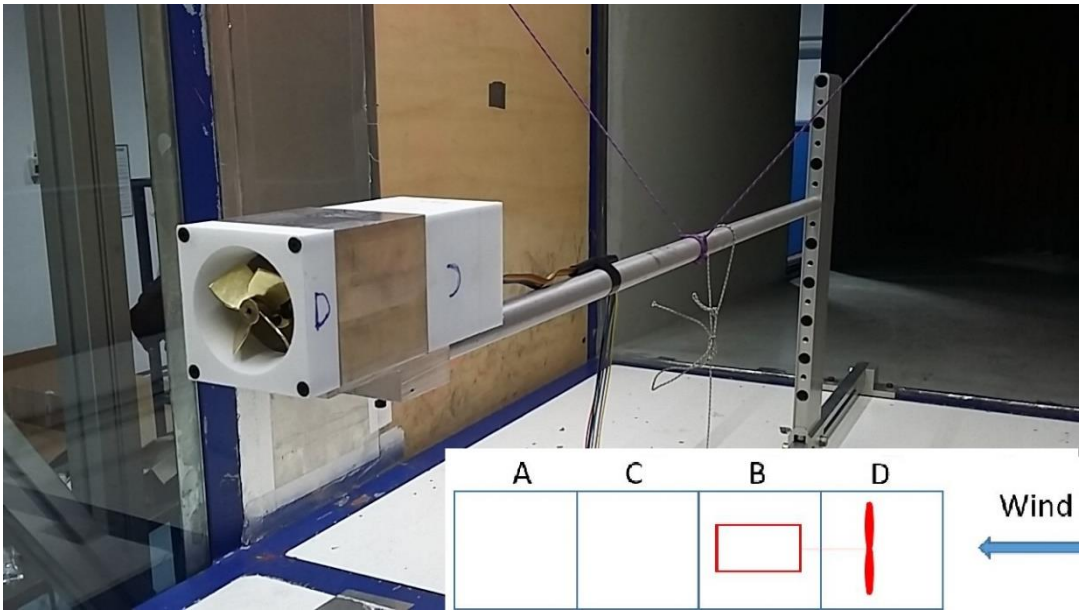

Figure 4.23 *Configuration 2-DBCA-T_DUP in upwind arragement*

3 ECBD-T_DDW (configuration 3): turbine in downwind configuration. Also in this case the configuration is similar to the one in figure 4.22, with the substitution of the module E instead of module A, sketch in figure 4.24.

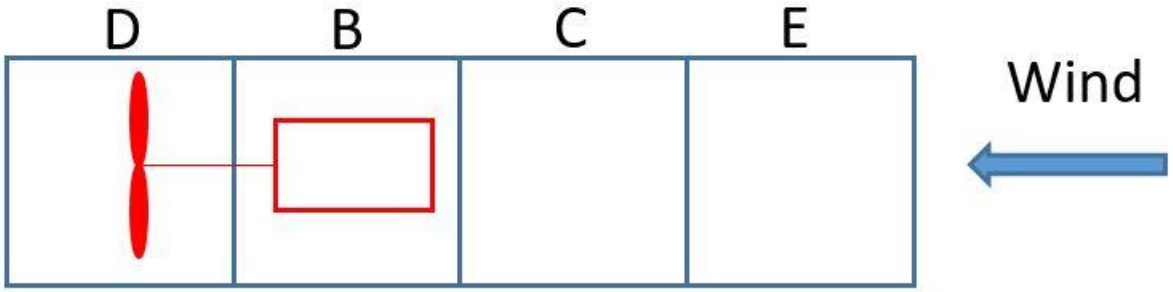

Figure 4.24 *Configuration 3-ECBD-T_DDW in downwind configuration*

4 DBCE-T_DUP (configuration 4): equal to configuration 4 but rotated by 180° with the turbine arrangement is in upwind.

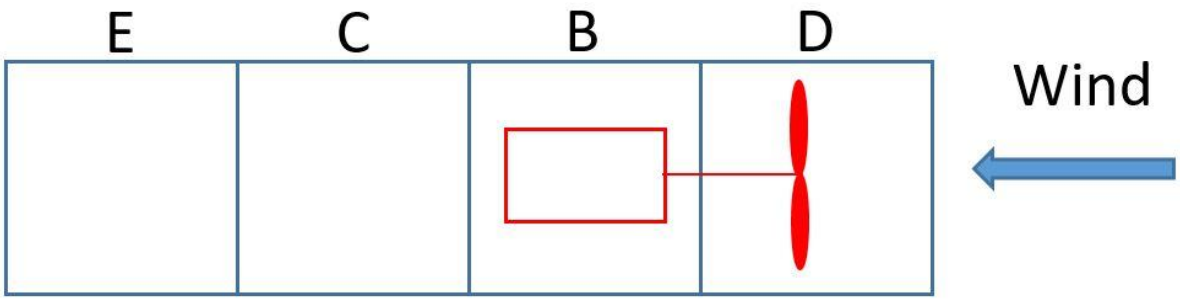

Figure 4.25 *Configuration 4-DBCE-T_DUP in upwind arrangement*

5 ACBE-T_EDW (configuration 5): turbine arrangements in downwind. This configuration is similar to configuration 1 but it includes a longer divergent (module E with $^{L}/_{D} = 0.4$).(figure 4.26).

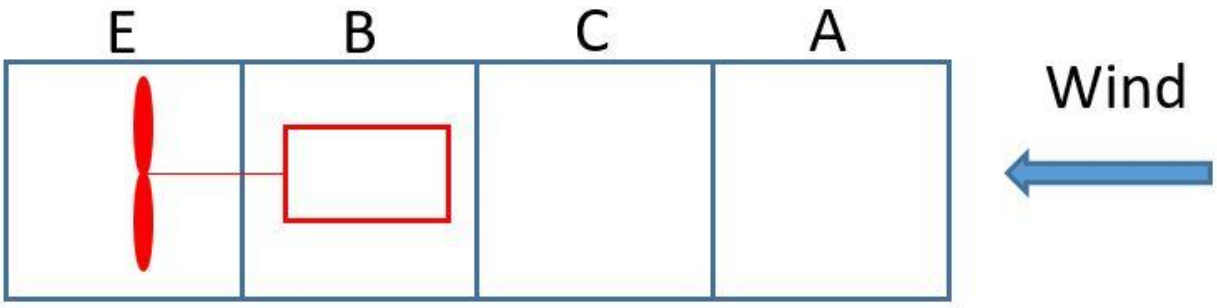

Figure 4.26 *Configuration 5-ACBE-T_EDW in downwind arrangement*

6 DCBE-T_CUP (configuration 6): the turbine is in upwind configuration. This configuration is studied in order to understand if the turbine positioned at the center could enhance the power production due to the convergent in D and diffuser in E, schematization in figure 4.27.

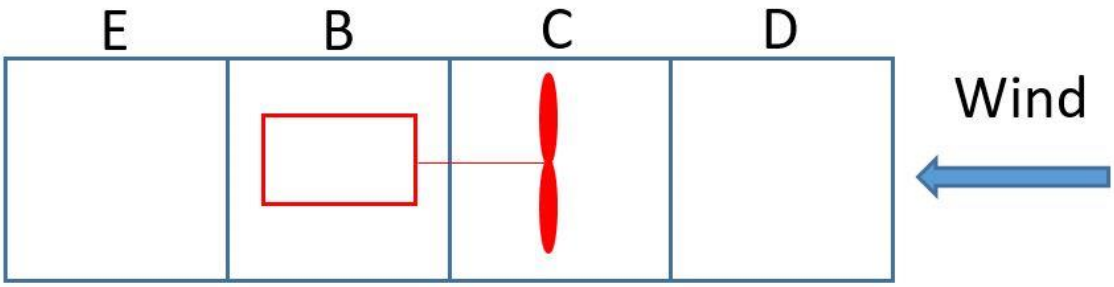

Figure 4.27 *Configuration 6-DCBE-T_CUP in upwind arrangement*

7 EBCD-T_CDW (configuration 7): equal to configuration 6 but rotated by 180° and with turbine in downwind arrangement. (figure 4.28).

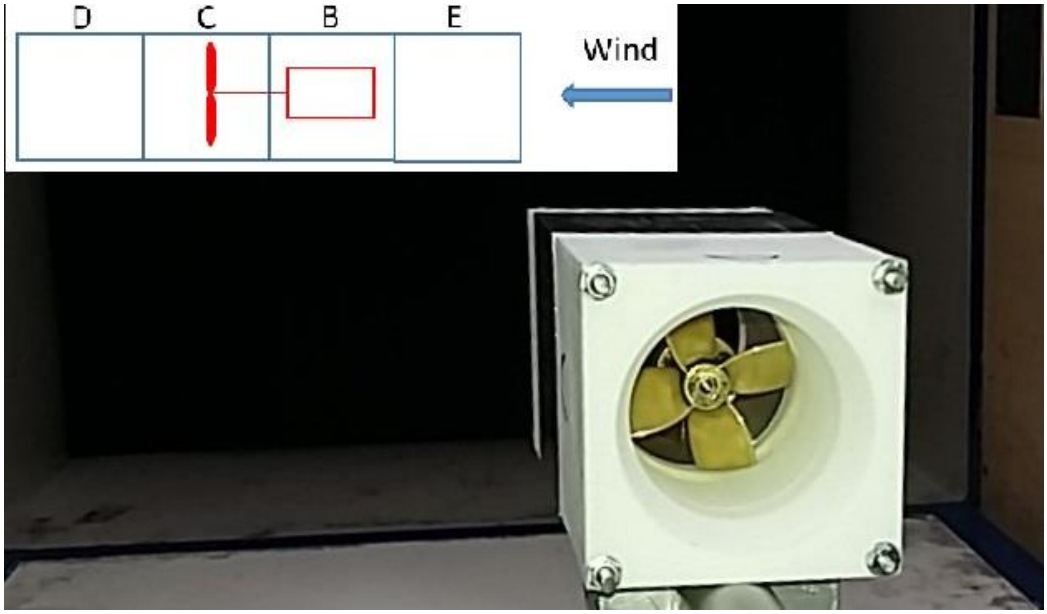

Figure 4.28 *Configuration 7-EBCD-T_CDW in downwind arrangement*

8 DBE-T_DDW (configuration 8): turbine arrangements downwind. This configuration is used to compare the influence of the duct length on the performance and it has a longer convergent on the turbine, module E, and the divergent downstream, module D (see figure 4.29).

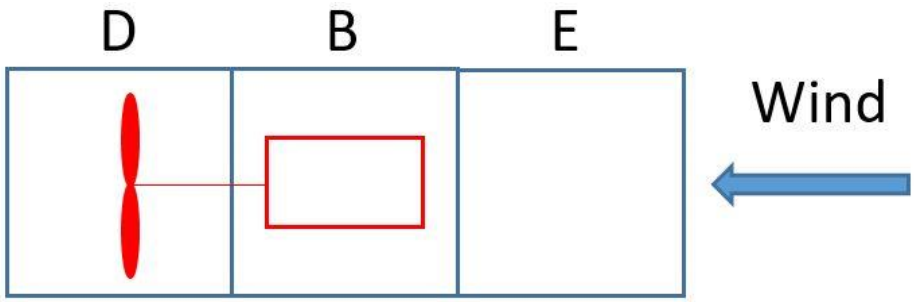

Figure 4.29 *Configuration 8-EBD-T_DDW in downwind arrangement*

9 DBE-T_DUP (Configuration 9): turbine arrangements upwind. This configuration is equal to the prevision one rotate by 180° in order to have the E module as convergent while module D becomes a divergent and it is the one that host the turbine, schematization in figure 4.30

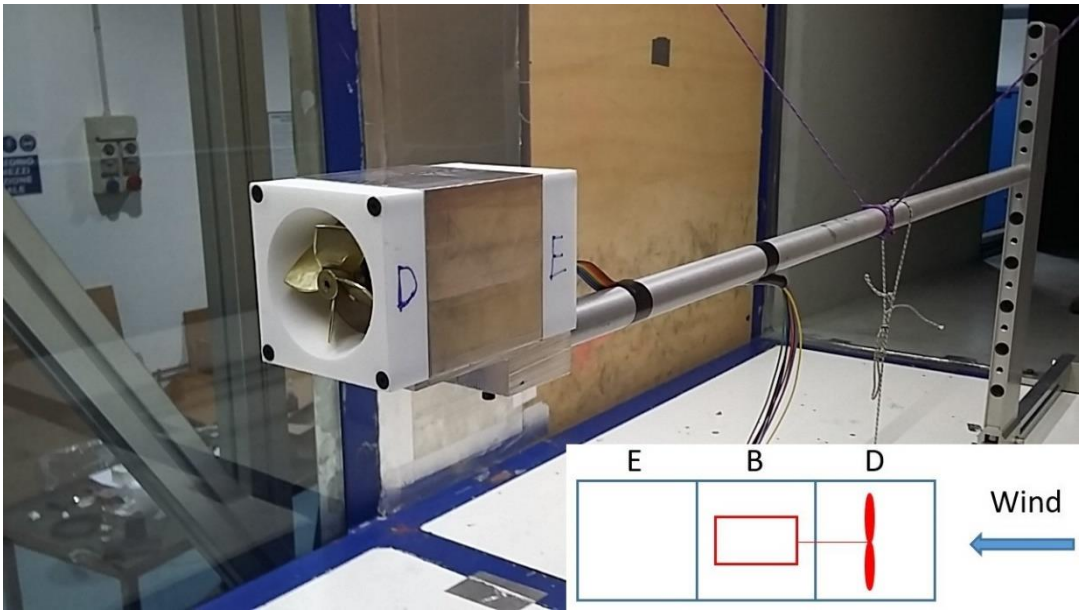

Figure 4.30 *Configuration 9-DBE-T_DUP in upwind arrangement*

4.3.2 Ducted turbine performance and comparison with open field results

As already mentioned, configuration 1 is the first design proposed for the ducted turbine.

It is taken as reference point for the following comparison on the effects of the different variations in the duct modules arrangement.

Configuration 1 has a simple constant section inlet while the outlet has a divergent shape, the turbine is placed in the divergent section in order to produce the configuration of [13].

Figure 4.31 shows the results in term of power compared to the performance of the turbine tested in open-field configuration.

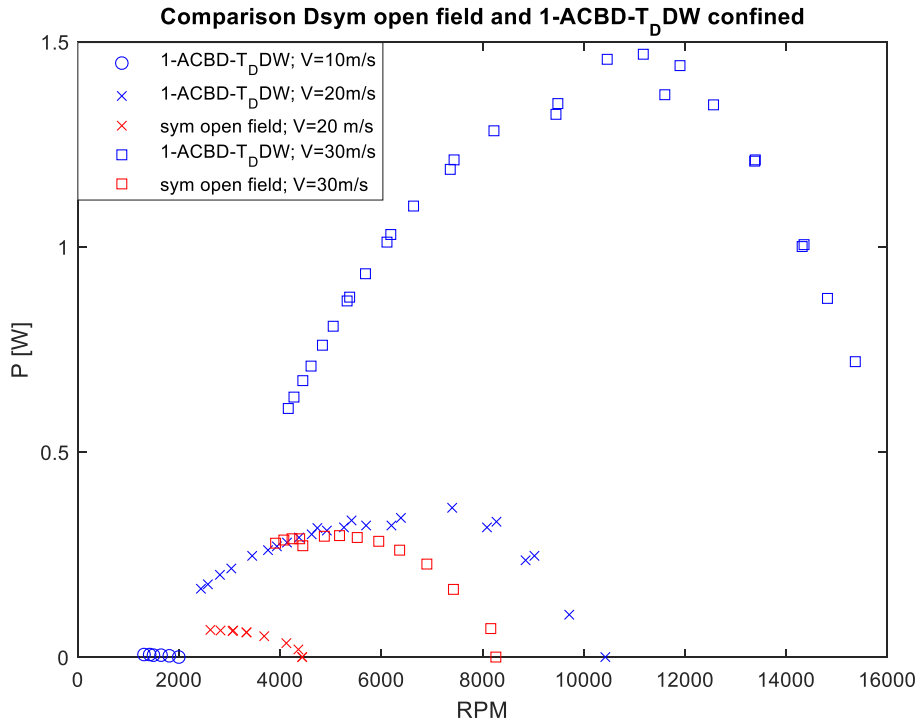

Figure 4.31 *Confined test: P vs RPM of the symmetric turbine in open field and 1-DBCA-T_DDW confined arrangement*

Table 4.12 reports the peaks power point data for the configuration 1 duct and the open field turbine.

	1-ACBD-T_DDW		**symmetric open field**	
Wind Speed	**P [W]**	**RPM**	**P [W]**	**RPM**
10 m/s	0.007	1306	-	-
20 m/s	0.36	7394	0.067	2627
30 m/s	1.47	11180	0.29	5174

Table 4.12 *Peak power comparison of open field symmetric turbine and 1-ACBD-T_DDW confined configuration*

As can be seen, confining the flow reduces the starting wind velocity of the turbine and increases the power generate by the turbine. In fact at 20 m/s the confined turbine power production increase of 81.3%, that remains almost the same, in percentage, increasing the wind speed.

The results show a very high power increase, definitely, higher the one found numerically in [13] using the same diffuser shape. The motivation could be related to the motor support effect, it is reasonable to assume that the ducted configuration has a beneficial effect in closing the motor support wake faster than in open field configuration resuting in a lower influence on the turbine performances.

4.3.3 Effect of divergent shape

IN the previous section a beneficial effect of the ducted configuration with a divergent outlet was shown. The next study is focused on the divergent length variation. Therefore a longer frustum diffuser is tested, in particular divergent module E, with $^{L}/_{D} = 0.4$ is substituted to module D. The configurations correspond to 1-ACBD-T_DDW and 5-ACBE-T_EDW in which both the turbines are in downwind configuration. Figure 4.32 shows the results in terms of power production.

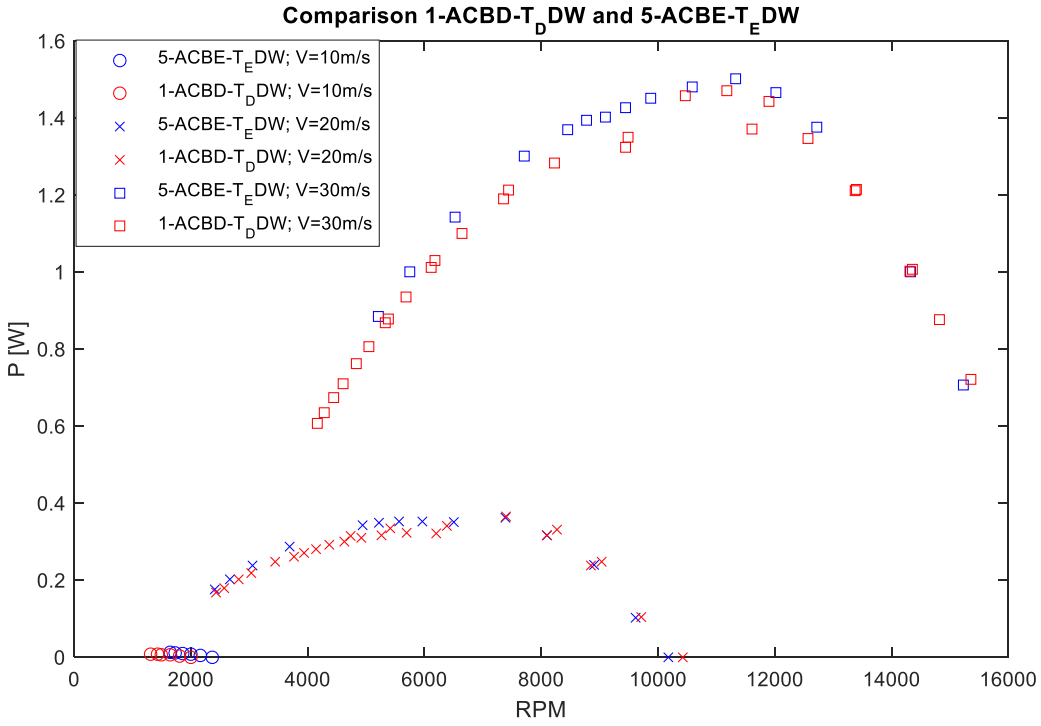

Figure 4.32 *Confined tests: P vs RPM of 1-ACBD-T_DDW and 2-ACBE-T_EDW comparison*

The results are comparable as in figure 4.32, therefore the longer diffuser, module E has a little to null effect in increasing the turbine power. The following table 4.13 shows the peak power results.

	1-ACBD-T_DDW		**2-ACBE-T_DDW**	
Wind Speed	**P [W]**	**RPM**	**P [W]**	**RPM**
10 m/s	0.007	1306	0.01	1643
20 m/s	0.36	7394	0.36	7388
30 m/s	1.47	11180	1.5	11330

Table 4.13 *Peak power results of 1-ACBD-T_DDW and 2-ACBE-T_DDW*

Since a longer divergent outlet do not enhance the power production another test is performed in order to understand if the same module can guarantee advantages if used as convergent. In fact the configuration 1, ACBD-T_DDW, has been tested and compared with configuration 3 (3-ECBD-T_DDW) using the module E as a convergent instead of module A at the inlet of the tube, in order to comprehend the effect of the addition of a convergent upstream the turbine, see figure 4.33.

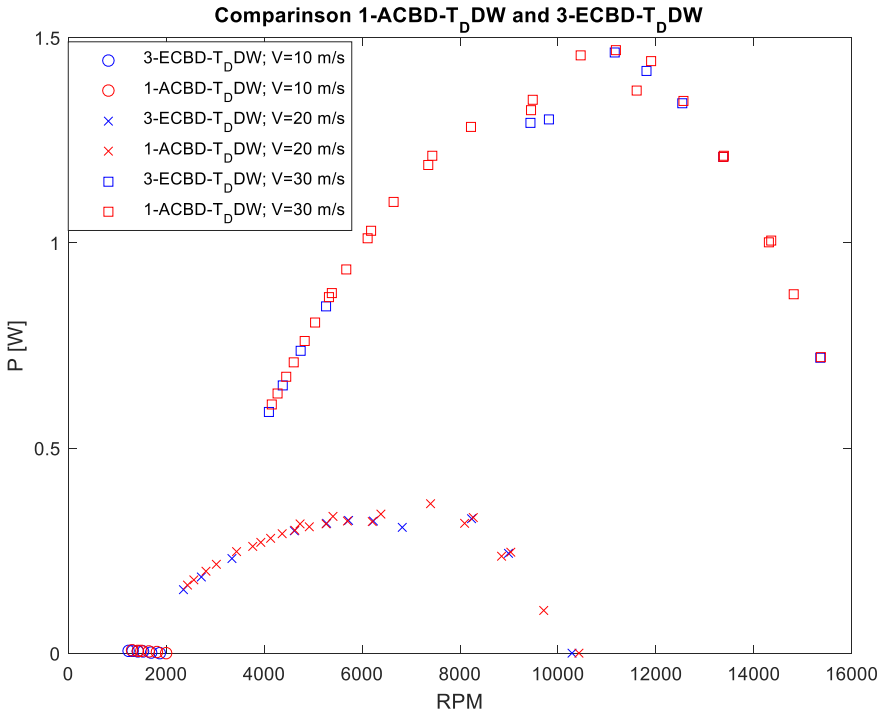

Figure 4.33 *Confined test: P vs RPM of 3-ECBD-T_DDW and 1-ACBD-T_DDW comparison*

As the graph shows the performance are comparable, hence, no additional effect can be appreciated by the addition of a convergent at the inlet. Therefore, no performance improvements can be noted using the modules D or E as divergent (figure 4.32), at the outlet of the tube, and using module E as convergent (figure 4.24).

Up to this point the base ducted configuration showed performance improvement in respect of the open field configuration. Analysis on the divergent shape and on the inlet type (constant section vs convergent) showed no influence on the results.

As final test on the divergent effect a configuration with constant section outlet is tested. The configuration 2, with module A as outlet, is compared with configuration 3 which is identical except for the presence of module E as outlet.

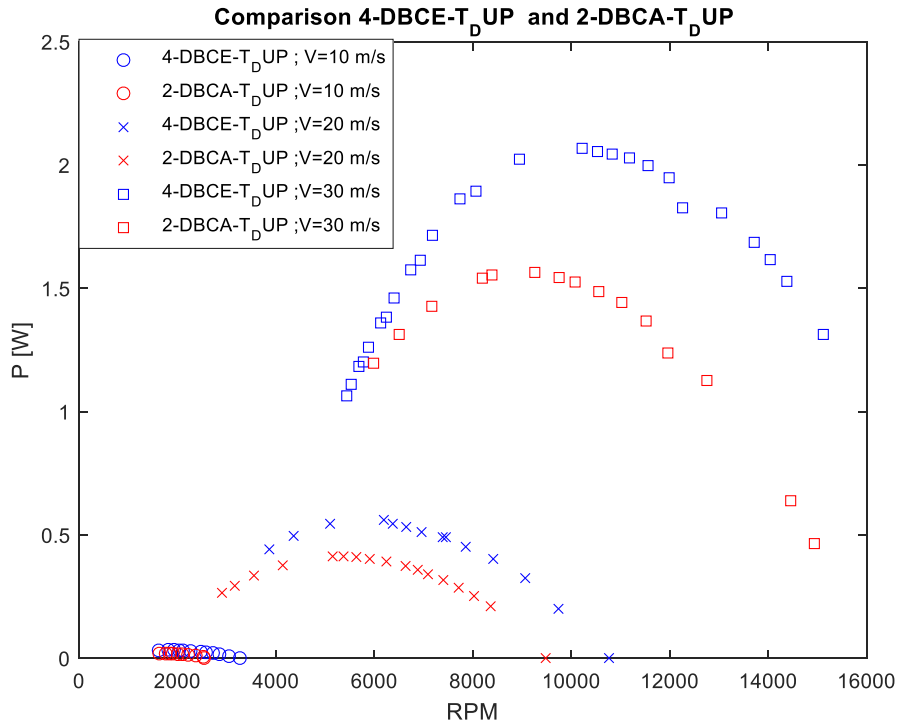

Figure 4.34 *Confined tests: P vs RPM of 4-DBCE-T_DUP and 2-DBCA-T_DUP conparinson*

The following table 4.14 gives an idea of the peaks power results difference, adopting downstream a divergent or a straight tube.

	4-DBCE-T_DUP		**2-DBCA-T_DUP**	
Wind Speed	**P [W]**	**RPM**	**P [W]**	**RPM**
10 m/s	0.034	1814	0.02	1633
20 m/s	0.56	6188	0.41	5379
30 m/s	2.07	10220	1.56	9264

Table 4.14 *Peak power results of 4-DBCE-T_DUP and 2-DBCA-T_DUP*

As expected the divergent located downstream increases the power production of about 24.4% thanks to the "back pressure" effect at 30 m/s, while at 20 m/s the power generated by the 4-DBCE-T_DUP configuration is 27% higher than the 2-DBCA-T_DUP arrangement at the same wind speed. In this case the power improvement percentage is similar to the one found in [13] using similar divergent section.

4.3.3.1 Conclusion on divergent effect

Some consideration could be drawn on the divergent and duct effect.

- The ducted turbine has higher performance than the open field one possibly due to a motor support wake reduction.
- A divergent outlet section can improve the overall performance by 20-30% aligned with the literature findings.
- A convergent section has almost null effect on the system behavior.
- The divergent shape has little effect on the performance. However only a little variations were tested for this work.

4.3.4 *Influence of turbine position and wind direction*

The turbine position inside a duct, at the extremities or in the center, and its arrangement with respect the wind direction, upwind or downwind, could influence the generated power. In this paragraph a comparison between different arrangements of the turbine are examined.

Firstly the wind direction effect is examined. The 4-DBCE-T_DUP and 3-ECBD-T_DDW, (configurations 4 and 3 respectively) are analyzed and in figure 4.35 results are presented. The two configuration have the inlet and the outlet switched in respect to the other one. As found in the previous section this have little influence on the results, thus any performance difference must be primarily related to the wind direction.

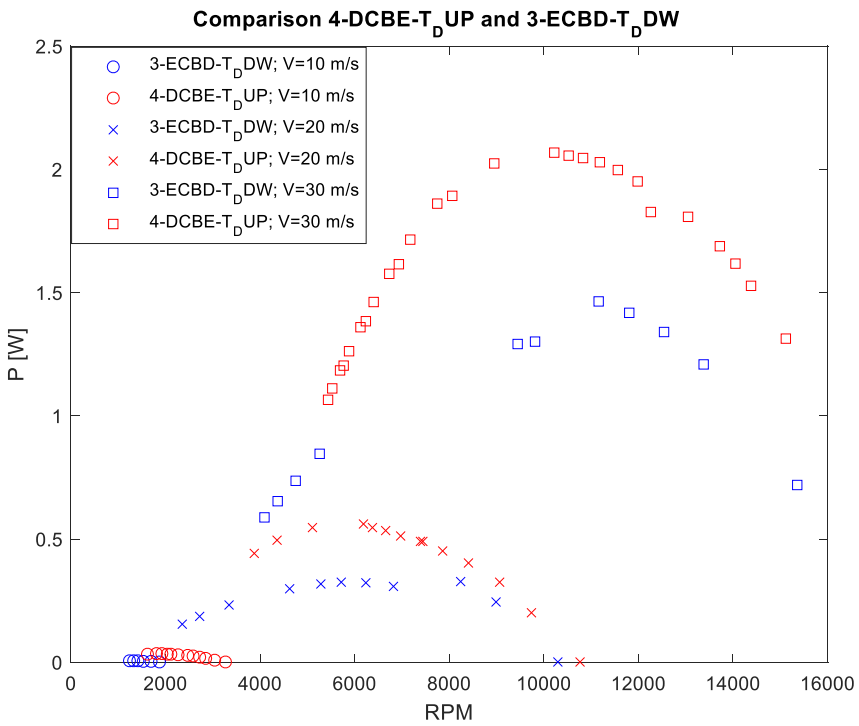

Figure 4.35 *Confined tests: P vs RPM of 4-DBCE-T_DUP and 3-ECBD-T_DDW comparison*

The table 4.15 shows the peaks power of both configuration to appreciate the increase of performance of the upwind arrangement.

	4-DBCE-T_DUP		3-ECBD-T_DDW	
Wind Speed	**P [W]**	**RPM**	**P [W]**	**RPM**
10 m/s	0.034	1814	0.006	1233
20 m/s	0.56	6188	0.62	6233
30 m/s	2.07	10220	1.46	11160

Table 4.15 *Peak power results of 3-ECBD-T_DDW and 4-DBCE-T_DUP*

The downwind configuration generated less power than the other one. This happens because the wake in downwind configuration do not have enough tube length to close and to benefit by the divergent property in module D. While in upwind arrangements the wake has more length before the tube outlet that favor its closing, and to take advantage of the divergent "back pressure" effect in module E to increase the generated power of about 82% at 10 m/s. In upwind arrangement the increase of power production in percentage reduces rising the velocity of the wind, in fact at 30 m/s the power is 30% higher than in downwind arrangement. It means that lower is the wind velocity higher is the contribution of the divergent.
In table 4.16 are summarized the comparison between:

- configurations 4-DBCE-T_DUP and the correspondent open field up wind arrangement;
- configurations 1-DBCA-T_DDW and the symmetric turbine in downwind arrangement (paragraph 4.3.2).

	4-DBCE-T_DUP	Sym open field upwind	1-DBCA-T_DDW	Sym open field downwind
Wind	**P [W]**	**P [W]**	**P [W]**	**P [W]**
10 m/s	0.034	0.01	0.007	-
20 m/s	0.56	0.27	0.36	0.067
30 m/s	2.07	1.01	1.47	0.29

Table 4.16 *Peak power comparison upwind and downwind arrangement considering open field and confined flow*

The upper table 4.16 shows a comparison between the confined flow and the open field in upwind and in downwind arrangements. From the data, It is possible to see that in upwind configuration the power increase up to 52% from the open field to the ducted system at 20 m/s; while in downwind, at the same wind speed, the performance increase is higher, equal to 80%. This means that the combination of a diffuser and a tube advantages more the downwind configuration respect to the upwind one.

Because the downwind arrangements (in figure 4.35) do not benefit by the divergent effect due to the short length of the tube in configuration 3-ECBD-T_DDW, the turbine is relocated at the center as in configuration 7, 7-EBCD-T_CDW, in order to understand if the turbine position is able to influence the power generation. In figure 4.36 a comparison between configuration 3 and 7 (3-ECBD-T_DDW and 7-EBCD-T_CDW respectively) is presented.

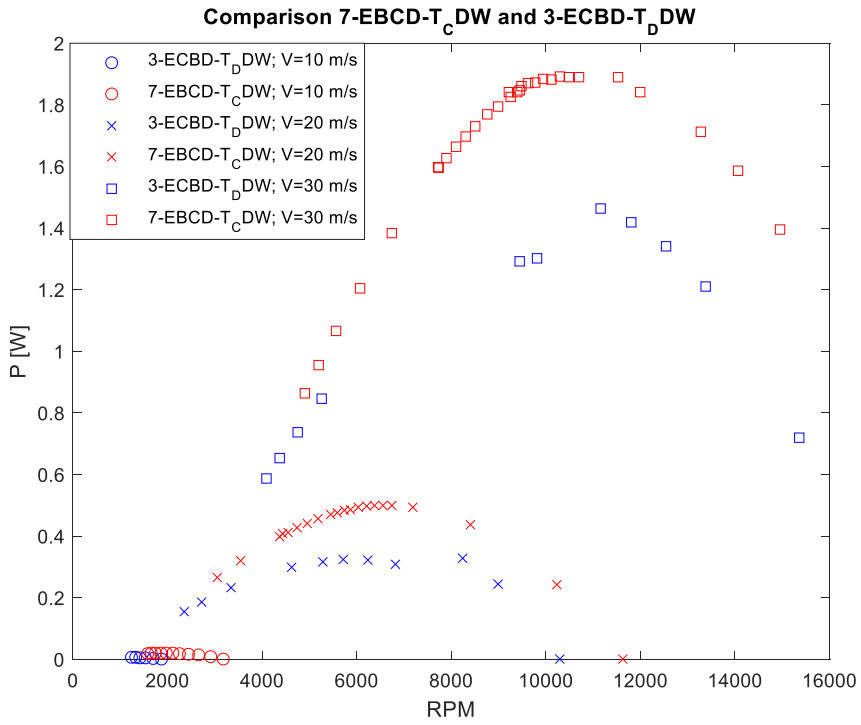

Figure 4.36 *Confined test: P vs RPM of 3-ECBD-T_DDW and 7-EBCD-T_CDW comparison*

In table 4.17 a peak power comparison of the previous analyzed configurations is shown.

	3-ECBD-T_DDW		**7-EBCD-T_CDW**	
Wind Speed	**P [W]**	**RPM**	**P [W]**	**RPM**
10 m/s	0.006	1233	0.02	1856
20 m/s	0.32	6233	0.48	6556
30 m/s	1.46	11160	1.88	10049

Table 4.17 *Peak power comparison of confined configurations 3-ECBD-T_DDW and 7-EBCD-T_CDW*

From the figure 4.36 the increase of the power is appreciated in configuration 7-EBCD-T_CDW, where the turbine's location is at the center of tube. The power raises by means of the advantage given by the diffuser in module D. As results, the turbine located at the center of the duct in downwind arrangement, has better performance than the configuration with the turbine at the extremity in 3-ECBD-T_DDW. In fact at 10 m/s

wind speed, 70% more power can be produce by the centered turbine, but in percentage the decrease of power generated reduces raising the wind velocity, passing from 33% at 20 m/s to 22% at 30 m/s. Furthermore the performance of configuration 7 arrived to be comparable with those of configuration 4 (4-DBCE-T_DUP).

Due to this consideration, a comparison of the turbine located at the center of the tube in upwind and downwind configuration is performed to understand if, also the upwind arrangement of configuration 6 (DCBE-T_CUP), could have the same amount of power production. Therefore a test between 7-EBCD-T_CDW and 6-DCBE-T_CUP is accomplish and results are presented in figure 4.37.

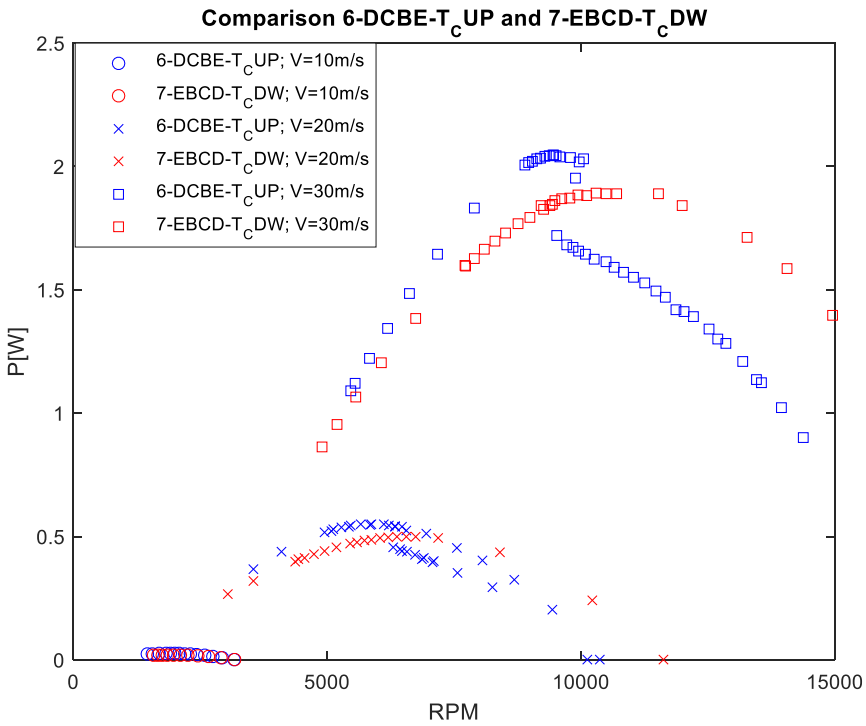

Figure 4.37 *Confined tests: P vs RPM comparison of 6-DCBE-T_CUP and 7-EBCD-T_CDW*

Table4.18 describes the behavior of the power regarding 6-DCBE-T_CUP and 7-EBCD-T_CDW configurations.

	6-DCBE-T_CUP		**7-EBCD-T_CDW**	
Wind Speed	**P [W]**	**RPM**	**P [W]**	**RPM**
10 m/s	0.026	1916	0.02	1856
20 m/s	0.55/0.45	6300	0.48	6556
30 m/s	2.08/1.7	9700	1.88	10049

Table 4.18 *Comparison of peak power of configurations 6-DCBE-T_CUP and 7-EBCD-T_CDW*

As can be seen, the power results are almost comparable at all the tested wind speed. The problem is the presence of an instability at the peak, as the velocity increases, regarding the upwind configuration 6-DCBE-T_CUP. This problem could probably caused by the reduced length of the duct in conjunction with the presence of the motor support.

4.3.5 Duct length effect

In the previous paragraphs the configurations compared regard the "Long" duct in different arrangements. In this section the "Short" duct configuration is examined in order to analyzed the differences in upwind and downwind configurations with the same block arrangements, and then the comparison is extended between "Long" and "Short" duct.

Therefore the short configurations considered are 8-EBD-T_DDW in downwind turbine arrangements and 9-DBE-T_DUP in upwind. The results are presented in figure 4.38.

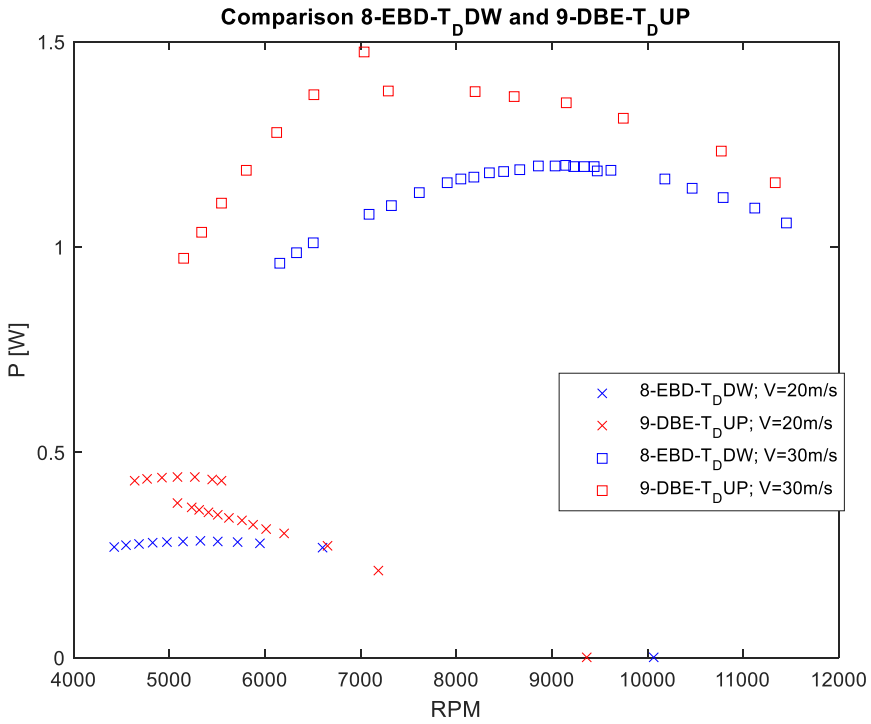

Figure 4.38 *Confined tests: P vs RPM comparison of 8-EBD-*T_D*DW and 9-DBE-*T_D*UP*

Table 4.19 summarized the results of both turbines arrangements.

	8-EBD-T_DDW		9-DBE-T_DUP	
Wind Speed	**P [W]**	**RPM**	**P [W]**	**RPM**

20 m/s	0.28	5327	0.44/0.38	5086
30 m/s	1.21	9230	1.47/1.38	7300

Table 4.19 *Peak power comparison of configurations 9-DBE-T_DUP and 8-EBD-T_DDW*

The result show that the upwind turbine in "Short" configuration 9, 9-EBD-$T_D UP$, presents the same instability (as for configuration 6-DCBE-T_CUP) that cause a reduction of power produced of about 6% at 30 m/s, while at 20 m/s the decrease in power becomes worst reaching 13.6%. The downwind configuration EBD-T_DDW, instead, is more stable even if it generates considerably less power at all the motor rotational speed.

A comparison between the "Short" and the "Long" configuration is necessary to examine the influence of the length on the confined flow turbine at the same wind direction ad same modules arrangement. Therefore, case 4-DBCE-T_DUP and 9-DBE-$T_D UP$ (configuration 4 and 9 respectively) are investigated in figure 4.39.

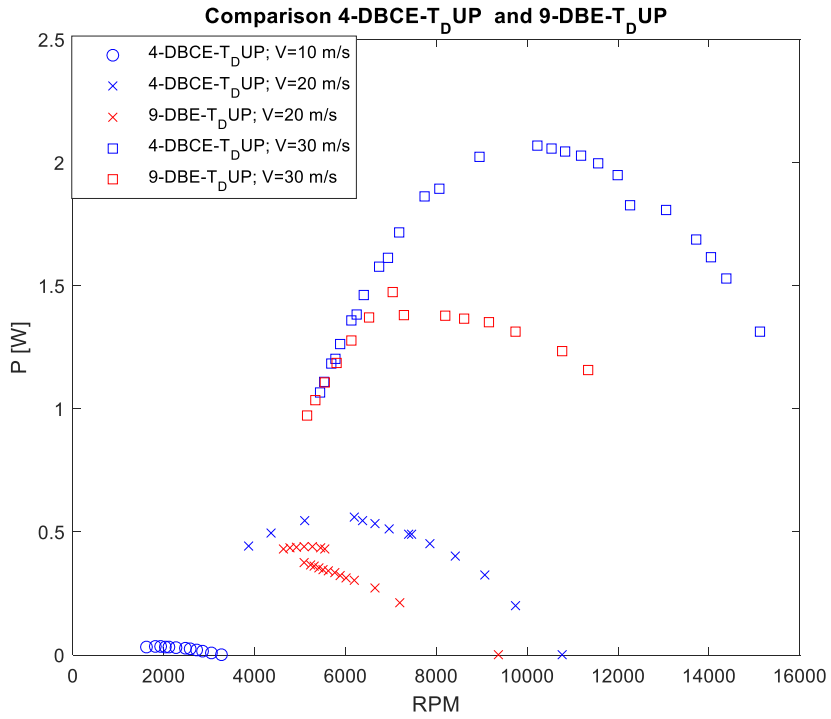

Figure 4.39 *Confine tests: P vs RPM comparison of 4-DBCE-T_DUP and 9-DBE-T_DUP*

In the following table 4.20 there is a peak power comparison between the two configurations.

	4-DBCE-T_DUP		**9-DBE-T_DUP**	
Wind Speed	**P [W]**	**RPM**	**P [W]**	**RPM**
10 m/s	0.035	1814	-	-

20 m/s	0.56	6188	0.44/0.38	5086
30 m/s	2.07	10220	1.47/1.38	7300

Table 4.20 *Peak power comparison between 4-DBCE-T_DUP and 9-DBE-T_DUP*

As can be seen in the graph the longer version generates more power and it is more stable. The decrease in power production with the "Short" configuration is about 33% for both wind velocity. Furthermore, in the rising part of the curve at 30 m/s the two configurations are superimposed.

The same comparison can be done in downwind turbine arrangement for both configurations, 4-ECBD-T_DDW and 8-EBD-T_DDW. The results are presented in figure 4.40.

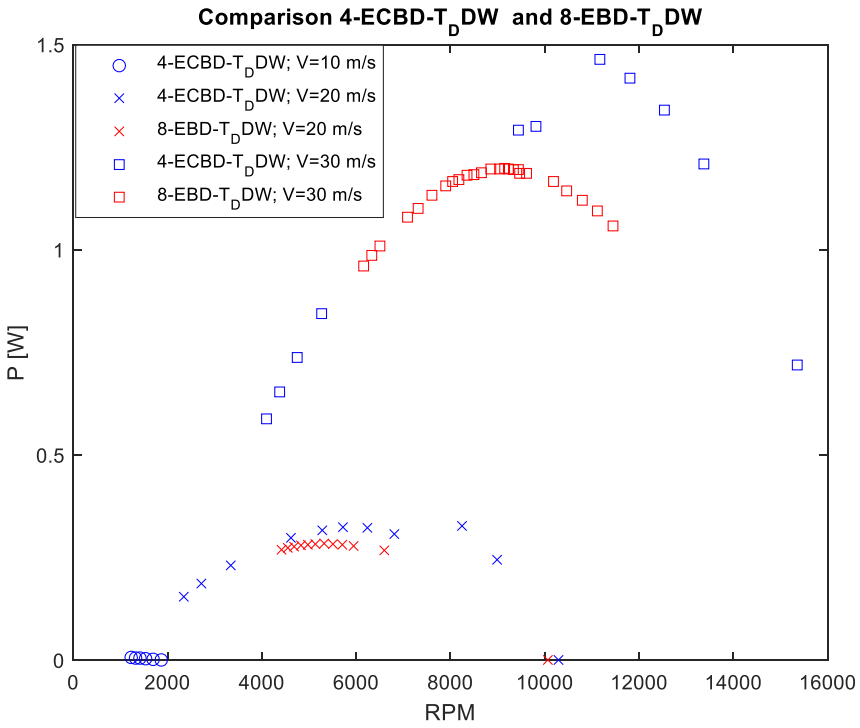

Figure 4.40 *Confined tests: P vs RPM comparison of 4-ECBD-T_DDW and 8-EBD-T_DDW*

Table 4.21 summarized the results of this comparison in downwind configuration considering the peak power of both arrangements.

	4-ECBD-T_DDW		**8-EBD-T_DDW**	
Wind Speed	**P [W]**	**RPM**	**P [W]**	**RPM**
10 m/s	0.006	1233	-	-
20 m/s	0.32	6233	0.28	5327
30 m/s	1.46	11160	1.21	9230

Table 4.21 *Peak power comparison between 4-ECBD-T_DDW and 8-EBD-T_DDW*

The results show that the "Short" turbine generates 6% less power at 20 m/s therefore the power production is almost comparable. While after the peak, at 30 m/s wind speed the power production difference increase until 17%. Therefore the upwind configuration of "Short/Long" comparison, the decrease in power generation duct is higher with respect the case in downwind arrangement in which the decrease in percentage is less evident. In fact at 30 m/s the upwind arrangement has a decrease of 33% while the downwind around 17%.

4.3.6 Grid effect on confined flow turbine performance

In the final application, the tube needs to be shielded at the inlet and at the outlet by means of a grid for safety purpose. Therefore, a test was performed using 7-EBCD-T_CDW layout, that has high performance, and a grid is added at both side of the duct (figure4.41), with a porosity equal to 56% obtained as ratio in equation (4.7):

$$\frac{A_{holes}}{A_{tot}} \qquad (4.7)$$

where A_{holes} corresponds to total area occupied by the holes, while A_{tot} represents the total area of the grid.

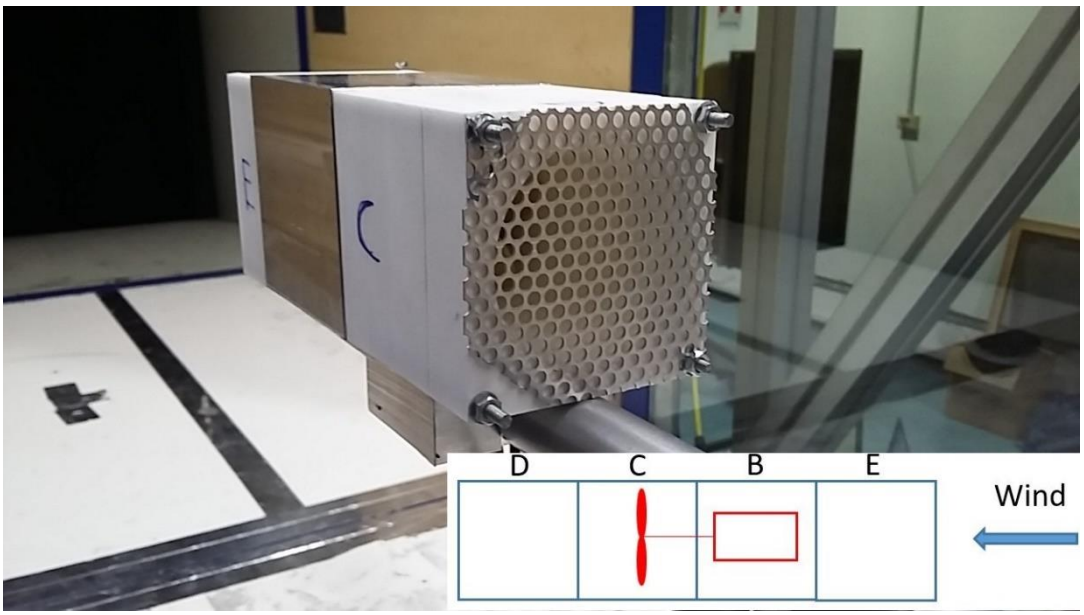

Figure 4.41 *Configuration 7-EBCD-T_CDW with grid*

In figure 4.42 the results of the comparison between the shielded configuration and the one without the grid are presented.

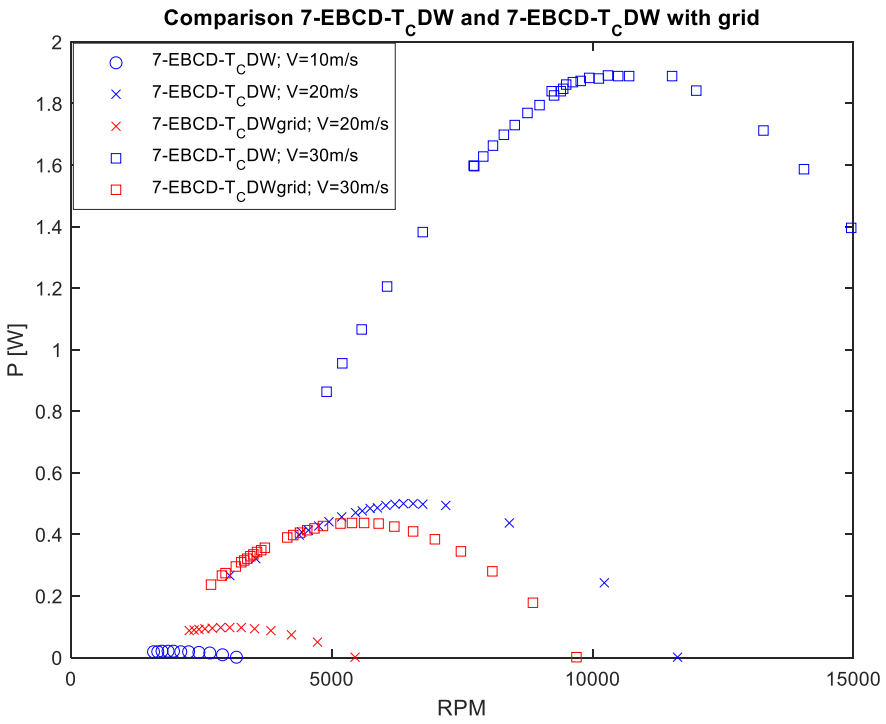

Figure 4.42 *Confined test: P vs RPM of 7-EBCD-T_CDW and 7-EBCD-T_CDWgrid comparison*

Table 4.22 resumes the performance in term of peak power of both configuration.

	7-EBCD-T_CDW		**7-EBCD-T_CDWgrid**	
Wind Speed	**P [W]**	**RPM**	**P [W]**	**RPM**
10 m/s	0.02	1856	-	-
20 m/s	0.48	6556	0.1	3265
30 m/s	1.88	10049	0.44	5624

Table 4.22 *Peak power comparison between 7-EBCD-T_CDW and 7-EBCD-T_CDWgrid*

As shown, the presence of the grid prevents the rotation of the turbine at 10 m/s and reduces the turbine performance to 80% at 20 m/s and 30 m/s wind speed. Therefore, the choice of the correct grid porosity is important in order to have low influence on the power generation.

CONCLUSIONS

Two airfoils blade turbines with 4 cm and 3 cm rotor diameter were designed by means of numerical method BEM in order to power autonomous sensorial node. The design turbines were realized and tested in a wind tunnel to evaluate the C_P and the power extracted at different wind speed and to compare the results with those numerically simulated by the BEM method. The experimental Cp curves have a similar behavior with those come from the simulations. However, the tests reveal that the peak of the power coefficient is about 30% lower and it reaches a lower Tip Speed Ratio equal to 1, while the numerical results it is established at higher TSR, equal to 1.5. Hence the numerical efficiency behavior seems to be shifted towards higher TSR.
Considering the comparison regarding the power, the experimental curves, as previously, reach lower peak and it is shifted toward left at lower tip speed ratio. The behavior of the power curves is slightly detached from the numerical one, when the wind speed is imposed at 20 m/s and 30 m/s, while at 10 m/s the behavior of the experimental curve corresponds to the numerical simulation, almost perfectly. Therefore the BEM model represents a reasonable method to provide airfoil cm-scale turbine design.
Moreover, a 4 cm turbine with symmetric blade was design in order to generate energy from a bi-directional wind, and its performances were compared with those with the airfoil shape.
All the turbines were tested in open field while the symmetric turbine were tested also in confined flow by means of a tube realized with different modules that allows to test different layouts.
The open field tests show that the power produced, using a prolongation shaft to favor the wake disposal, by the 4 cm and 3 cm airfoil turbines is higher than the symmetric turbine, as expected because of the optimized design of the airfoils, but the results demonstrate, also, a flexional instability of the extended shaft at high wind speed. Therefore, the tests carried out with the turbine attached to the turbine shaft prove higher turbine stability but reduced power generation, about 50% less at 10 m/s wind speed. In the same configuration but in downwind arrangement, the tests show that the decrease of the power enhance at 73% reduction at 20 m/s respect to the upwind configuration.

Another important result, derived from the open field test, is the influence on the performance produced by the motor support. The support S_2, designed to have the lowest impact on the wake disposal and on the air flow, demonstrates to increase performance of the symmetric turbine that is able to produce the same amount of power generated with the additional shaft; therefore the support S_2 can enhance the power production up to 45%.

The confined tests reveal an improvement in power generation with respect the open field, in fact the ducted symmetric turbine in downwind arrangement, is able to increase the power generated up to 81% due to a combined effect of the duct and the diffuser. Then, confined flow tests, specifically focused on the divergent, are performed. They reveal that the variation of the length of the diffuser at the outlet of the duct does not improve the turbine's performance, and the same consideration is accomplished when the diffuser shape is used with the purpose of convergent at the inlet of the tube. In order to enhance the turbine power generation the diffuser need to be positioned downstream and this arrangement proves to increase the power up to 27% at 20 m/s.

Moreover, tests show that the position of the turbine inside the tube can increase the power production. As seen, the turbine centered in downwind arrangement enhances the power up to 70% at 10 m/s, with respect to the turbine positioned at the extremity in the same arrangement. However, the centered turbine in upwind configuration shows an instability that cause a decrease of the power. Furthermore, the duct length investigation results reveal that decreasing the tube length do not enhance the performance and in upwind configuration the short tube configuration exhibits an instability.

As final test, the ultimate application in simulated applying a grid at the outlet and at the inlet of the duct and the results show that the grid caused a decrease of power up to 80% at all the wind tested velocity.

However also including the protective net the design turbine performances (almost 100 mW at 10 m/s) are considered sufficient [8] for remote sensing application.

In conclusion a cm-scale rotor was designed using common wind turbine design algorithm, and produced with rapid prototyping technologies.

Finally a series of wind tunnel tests confirm the feasibility of a wind powered remote sensor for freight train instrumentation.

Future work could be the improvement of numerical code performances to improve the matching with experimental results. In particular reliability of classical BEM code at low TSR can be more deeply investigated and also blade sectional aerodynamic data at very low Reynolds can be improved. Also the divergent duct showed very good performances, probably a deeper analysis with high fidelity numerical model, i.e CFD-RANS, will improve the understanding of the physics behind the duct turbine good behavior.

Bibliography

[1] A. T. a. L. G. F. David Rancourt, "Evaluation of Centimeter-Scale Micro Wind Mills: Aerodynamics and Electromagnetic Power Generation," pp. 93-96, 2007.

[2] F. Y. J. H. Y. Q. F.J Xu, "Miniature horizontal axis wind turbine system for mutipurpoe application," *Elsevier,* pp. 216-224, 2014.

[3] A. B. a. S. H. D A Howey, "Design and performance o a centimetre-scale shrouded wind turbine for energy harvesting," pp. 1-12, 2011.

[4] D. B. D. B. a. L. B. Davide Carli, "A high-efficiency wind-flow energy harvester using micro turbine," *Speedam,* pp. 778-783, 2010.

[5] G. H. a. K. R. P. Andrew S. Holmes, "Axial-flux permanent magnet machines fo micro power generation," *Journal of microelectomechanical system,* vol. 14, no. 1, pp. 54-62, 2005.

[6] M. O. L. Hansen, Aerodynamics of wind turbines, Earthscan, 2008.

[7] J. F. M. a. J. G. McGowan, Wind energy explaind: theory, design and application, John Wiley & Sons Ltd, 2009.

[8] H.-J. H. H. J. a. B. F. S. J. Jong-Woong Park, "Feasibility study of micro-wind turbines for powering wireless sensors on a cable-stayed bridge," *Energies,* vol. 5, no. 9, pp. 3450-3464, 2012.

[9] S. B. P. G. J. W. M. G. a. J. L. R. M Perez, "A cm scale electret-based electrostatic wind turbine for low-speed energy harvesting application," *IOP science,* pp. 1-10, 2015.

[10] C. C. F. a. J. Chen, "Air-powered sensor," *IEEE sensors,* vol. 1, pp. 22-25, 2003.

[11] A. P. B. P. G. A. G. a. M. S. S. Christopher A. Lyon, Summary of Low-Speed Airfoil data, Virginia, 1997.

[12] F. P. R. P. o. L. H. A. W. Turbines, VITERNA, L.A., C ORRIGAN, R.D., Cleveland, 1982.

[13] B. S.A.H.Jafari, "Flow analysis of shrouded small wind turbine with a simple frustum duffuser with computational fluid dynamics simulations," *Journal of Wind Engineering and Industrial Aerodynamics,* pp. 102-110, 2014.

[14] B. D. M. B. A. B. R. W. D. J. B. B. a. M. S. S. Gregory A. Williamson, Summary of Low-Speed Airfoil Data, 2012.